DTU Library

Dynamics of photonic crystal nanolasers based on Fano resonance

Liang, Shih Lun

Publication date:
2023

Document Version
Publisher's PDF, also known as Version of record

[Link back to DTU Orbit](#)

DTU Electro
Department of Electrical and Photonics Engineering

Dynamics of photonic crystal nanolasers based on Fano resonance

Shih-Lun Liang

Kongens Lyngby, Denmark 2023

Supervisor: Prof. Jesper Mørk
Co-supervisors: Dr. Yi Yu & Prof. Kresten Yvind

Abstract

This thesis presents an investigation into the dynamics of photonic crystal Fano lasers. It combines theoretical analysis and simulations, practical application estimations, and experimental validations to deepen our understanding of laser dynamics and their potential applications.

Initially, the thesis revisits the fundamental concepts and steady-state properties of Fano lasers. A new multi-section approach that includes carrier diffusion, a factor previously unexplored in Fano laser models, is developed. We investigate the model's numerical stability for this approach and assess the deviations from previous models that assumed uniform carrier distribution.

The focus then shifts to the modulation of the Fano laser's nanocavity. Under rapid modulation, pulses with unique waveforms are generated in Fano lasers. Utilizing the concepts of Q-switching and cavity-dumping, we explain the underlying physics and examine the characteristics of those pulses. Methods for tuning the nanocavity's refractive index, such as the free carrier effect and thermal effect, are analyzed. This analysis facilitates the construction of a modulated Fano laser model that accurately predicts pulse generation phenomena, which aligns well with experimental results. Comparisons with Fabry–Pérot lasers demonstrate the energy efficiency of Fano lasers in pulse generation.

Expanding beyond conventional Fano lasers, we explore a new configuration featuring an active external feedback cavity. This structure reveals multiple oscillation modes, including optical bistability between Fano and Fabry–Pérot modes under specific nanocavity detuning conditions. This discovery sparks interest in utilizing feedback Fano lasers as flip-flop devices, potentially creating compact, energy-efficient optical memories. The characteristics of flip-flop operations are investigated, showcasing picosecond switching times and femtojoule energy consumption per bit. Preliminary experiments on prototype feedback Fano laser samples, although not yet exhibiting bistability, reveal multiple modes consistent with theoretical predictions. Optical-thermal characteristics of these samples are also measured. An analytical comparison between two coupled cavities nanolasers and waveguide-nanocavity systems highlights our system's stability and absence of mode oscillation.

Finally, the focus changes to the stochastic simulation of nanolasers, using a quantum-based approach distinct from the semi-classical methods used in previous chapters. We revisit two stochastic methods—the fixed time increment (FTI) method and Gillespie's first reaction method (FRM)—and compare their characteristics and

computational efficiency. The focus is on the behavior of nanolasers in near-threshold regions, where we successfully capture the photon burst phenomenon with quantum dot laser configurations. We also calculate the deviations between analytical solutions and those obtained from the two stochastic methods and analyze the photon statistics of pulses generated during laser turn-on transients.
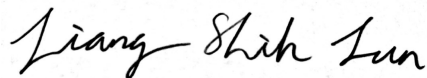
In summary, this thesis pushes the boundaries of understanding the nanolaser dynamics based on Fano resonance, exploring new configurations and operating methods, and laying the groundwork for future photonics and optical computing innovations.

Preface

This thesis is presented in partial fulfillment of the Ph.D. degree requirements at the Technical University of Denmark (DTU). The research was undertaken in the Quantum and Laser Photonics group at the Department of Electrical and Photonics Engineering (DTU Electro), spanning from August 2020 to October 2023 under the supervision of Professor Jesper Mørk, Professor Kresten Yvind, and Senior Researcher Yi Yu.

Kongens Lyngby, 13th December 2023

Shih-Lun Liang

Acknowledgements

First and foremost, I am deeply thankful to Jesper Mørk, my supervisor, for his invaluable guidance and support. His talent to simplify complex ideas and patiently answer my questions have significantly enriched my learning journey. Additionally, his enthusiastic and well-organized leadership has not only enhanced our group's productivity but has also provided me with valuable insights into team management.

A heartfelt thank you to Yi Yu, my co-supervisor, for tackling the toughest and most tedious parts of my research. His step-by-step guidance has been crucial in shaping my research, and our discussions have always been very insightful. I am particularly grateful for his thorough review of our publications. Without his expertise and support, the accomplishments of this thesis would not have been possible.

I want to give a big thanks to Gaoneng Dong for his significant role in my PhD studies. Learning from him in the lab and collaborating on our publications has been both rewarding and enjoyable. Plus, I appreciate the badminton tips! Meng Xiong also deserves a thank you for always creating excellent samples for our group. She was a big help during my early days in Denmark, and our chats were always a nice break from the PhD workload. Besides, thanks to my office mates, Evangelos, Mavi, and Kristian, for their constant friendliness and helpfulness.

A special thanks goes to Gian-Luca Lippi, my host supervisor during my time in Nice. He handled all the paperwork and logistics and really looked out for me and brought great energy to our project. The discussions with him were always enlightening and gave me fresh ideas and directions. Those two months in Nice were incredibly productive and enjoyable, largely thanks to his support.

Outside of work, I want to thank my best friends, Dayang, Sihang, and Yi-Chieh, for making my time in Denmark so memorable. From great lunches to fun weekends and holidays, you have been the best. Wishing you all success in your PhD journeys and beyond.

Finally, I extend my gratitude to Serena for her company, support, and encouragement. Completing this thesis would have been much harder without her.

List of publications

Journal publications

- G. Dong, **S. L. Liang**, A. Sakanas, E. Semenova, K. Yvind, J. Mørk, and Y. Yu, "Cavity dumping using a microscopic fano laser," *Optica*, vol. 10, pp. 248–254, 2023.

- **S. L. Liang**, J. Mørk, and Y. Yu, "Optical bistability and flip-flop function in feedback Fano laser," *submitted*.

Conference proceedings

- G. Dong, **S. L. Liang**, Y. Yu, A. Sakanas, E. Semenova, K. Yvind, and J. Mørk (2021). "Direct optical modulation of photonic crystal fano laser via the mirror," in *OSA Nonlinear Optics 2021*, 2021.

- **S. L. Liang**, J. Mørk and Y. Yu, "Bistable Fano Laser with Optical Feedback," in *Conference on Lasers and Electro-Optics (CLEO) 2023*, San Jose, CA, USA, pp. 1-2. 2023.

- **S. L. Liang**, J. Mørk and G. L. Lippi, "Comparison and Analysis of Stochastic Simulation Techniques for Near-Threshold Microlasers," in *31st Annual International Laser Physics Workshops*, 2023.

Contents

Introduction

1.1 Semiconductor photonic crystal nanolasers in the modern world applications

In today's world, communication technology emerges as a cornerstone of global inter-connectivity, driving advancements in diverse fields. The last decade has witnessed a dramatic increase in network bandwidth demand, driven by the rise of applications such as virtual reality, online gaming, cloud computing, and high-definition video streaming [1]. Central to this advancement is the role of semiconductor lasers, which have become pivotal in optical communication due to their compactness, efficiency, and high-speed operation capabilities. As an essential component in optical commu-nication systems, they have revolutionized how information is transmitted, offering a blend of high bandwidth and lower energy consumption [2] crucial for modern com-munications. The development of on-chip laser technology represents a significant ad-vancement in this field. Semiconductor lasers have been miniaturized to fit on chips, leading to the emergence of integrated photonic systems. These compact systems offer enhanced speed and energy efficiency performance, which is vital for modern data centers that consume vast amounts of electricity, mainly for data processing and transmission needs [3]. Reducing power consumption and size are key benefits of on-chip laser technology, addressing critical challenges in optical communication.

Photonic crystal lasers [4] represent a breakthrough in semiconductor laser tech-nology. Known for their ability to confine light within extremely small volumes [5], photonic crystals create unique lasing properties essential for high-performance in-tegrated photonic devices. Their ease of integration into silicon makes them highly desirable for both inter-chip and intra-chip optical interconnects. Research has shown the advantages of photonic crystal lasers, such as low threshold current [6, 7], high output power [8, 9], and low divergence angle of PhC lasers [9, 10], which lay the foundation for establishing potential monolithic light sources for high-density optical interconnects in future electronics [11]. The advancement of on-chip semiconductor lasers has also positioned them as promising candidates for key roles in the fields of all-optical computing and artificial intelligence. This integration is essential for ad-vancing all-optical computing, where light is used for information processing, poten-tially leading to faster and more energy-efficient computation methods by avoiding electrical-to-optical transduction [12]. In the architecture of computer frameworks,

one of the key aspects is memory. The laser's bistable characteristic [13], is suitable for binary information mapping. Moreover, in artificial intelligence, these on-chip semiconductor lasers, particularly efficient in generating spikes, can mimic biological neural networks through spike generation, enabling fast information processing [14]. This unique characteristic positions on-chip semiconductor lasers as powerful tools in machine learning applications, meeting the growing need for advanced computing technologies.

This study focuses on the dynamics of photonic crystal lasers, particularly when a phenomenon known as "Fano resonance" emerges within the nanometer scale structures. Exploring aspects like spike generation and bistability with lower energy consumption. This research holds potential for advancing emerging computing and communication technologies.

1.1.1   Development of on-chip optical memories

The principle behind optical memories is to utilize light, instead of electrical charges, to store and retrieve binary information. This shift from electronic to photonic data storage has numerous advantages, such as high bandwidth and low latency [15], which are essential for high-speed data processing and communication systems. Using light as a data medium also implies less heat generation and reduced energy consumption compared to traditional electronic memories, which might solve the problem of thermal management, which is one of the critical issues in modern computing hardware [3].

The necessity of a pumping source for lasers makes them only suitable for volatile memories. However, the bistability phenomenon (Chapter 4) that appears in lasers allows for operation without constant refreshing and rewriting, making them appropriate for static random access memory (SRAM), which can operate much faster than dynamic random access memory (DRAM). The skin effect in electrical wiring, which causes an increase in resistance and energy consumption at higher operating frequencies [16], is a challenge unique to electrical systems. This issue, absent in optical systems, also serves as a limiting factor for the bandwidth of electronic RAM. Presently, the bandwidths of state-of-the-art on-chip electronic SRAM are limited to approximately 20 GB/s [17]. Another major advantage of optical memory over electronic systems is the access time, limited in electronics by RC delay. State-of-the-art high-performance electronic SRAM exhibits access times around 200 ps [18]. In contrast, laser systems have shown response times of less than 70 ps across various platforms [19–21] (as also shown in this work). In the 2020 study, T. Alexoudi et al. [15] provided a comprehensive comparison of access times versus energy consumption per bit for both optical and electronic memory technologies (see Fig. 6(b) in the work [15]). Optical memory has improved power efficiency from around 2 pJ/bit [19] to less than 10 fJ/bit [21] while maintaining memory access times under 100 ps, offering short access times with energy efficiency improvements. In contrast,

electronic memory struggles to improve memory access times and energy efficiency simultaneously due to increased energy and heat dissipation requirements [18].

One of the primary disadvantages of the optical system might be its integration density. Currently, electronic SRAM has achieved a size reduction down to 0.027 μm^2 with 7 nm processing technology [22], whereas most optical systems remain above 1 μm^2. T. Alexoudi et al. [15] (refer to Fig. 6(a) in the work [15]) shows the evolution of optical and electrical SRAM components in terms of footprint over the past two decades. The early 2000s marked a key period for optical memory, driven by advances in reliable photonic integration. The progression from larger hybrid-integrated configurations using planar lightwave circuit technology [20] to compact, monolithically integrated memory cells [23], and eventually towards sub-micrometer-scale photonic crystal nanocavities or nanolasers [21,24], signifies a dramatic reduction in scale. This trajectory represents a twelve-orders-of-magnitude improvement in footprint, transitioning from square meter-scale bulky components [25] to today's micro-meter-scale integrated cells. In comparison, electronic technology evolved from a 130 nm^2 processing node [26] to a 7 nm^2 node [22] during the same period, shrinking SRAM cell size by three orders of magnitude. The advancement in optical memory technology has been more pronounced and rapid compared to its electronic counterpart.

1.1.2   On-chip lasers in photonic neuromorphic computing

The traditional centralized processing architecture of computers, characterized by a central processor and separate memory units, is not optimal for managing distributed, massively parallel, and adaptive computational models. These types of models are particularly prevalent in neuromorphic computing within artificial intelligence (AI), which aims to mimic the network structure of the human brain [14]. Neuromorphic computing, which often requires a hierarchical processing structure and recurrent networks for tasks like image and language processing [14], demands the signals to travel relatively longer distances for distributed information processing. Photonic waveguides present an ideal solution due to the distinct advantage over their electronic counterparts, as they have lower attenuation and do not suffer from heat generation or signal distortion issues [27], such as the skin effect, as previously mentioned.

On-chip lasers are crucial in this framework as they can not only be seamlessly integrated with waveguides to construct photonic neural networks but also can act as neurons. These photonic neurons are designed to handle multiple optical inputs, implement a nonlinear operation, and generate an optical output to activate other photonic neurons. Lasers provide the requisite nonlinear response for neuron-like processing. Spike neurons, a common category in neuromorphic computing [14], are designed to produce spiky output only when the input exceeds a specific threshold, similar to the way lasers generate pulses through modulation. Traditional methods of laser pulse generation typically involve using an external modulator to modulate a continuous-wave laser signal [28], or altering the laser gain around the lasing threshold [29]. The former approach tends to occupy a substantial footprint, while the latter

requires excessive energy, hindering the capability to drive other photonic neurons (cascadability) and energy efficiency. Consequently, developing on-chip lasers with compact modulators and energy-efficient modulation methods, as presented in this work (Chapter 3), becomes essential. This study could lead to the development of more efficient, scalable, and powerful photonic-based neural network architectures, potentially transforming AI computing and related fields.

1.2   Overview of the thesis

This work's primary goal is to explore nanolaser dynamics based on Fano resonance. Theoretical models of Fano lasers have been extensively developed over the past decade, encompassing aspects such as lasing mode [30], modulation response [30–32], self-pulsing mechanism [33], and stability under weak feedback [34, 35]. Corresponding experimental studies have also been conducted, including demonstrations of self-pulsing [36] and linewidth measurement [37]. This work seeks to extend the frontiers of this field further.

Chapter 2 introduces the fundamental concept of the Fano laser. It starts with the temporal coupled mode theory, forming the basis for deriving the formulae for reflection and transmission of the Fano mirror and steady-state lasing conditions. Extending from conventional semiconductor equations, small perturbation dynamics rate equations and iterative dynamics rate equations for Fano lasers are derived. An improved multi-section model that accounts for carrier diffusion is proposed. The effects of the number of sections and diffusion rate on calculation results and stability are examined, along with comparisons between various models.

Chapter 3, based on the published work "Cavity dumping using a microscopic Fano laser" [38], where I contributed as the second author alongside G. Dong in experimental work. This chapter explores two laser pulse generation mechanisms: Q-switching and cavity dumping. These mechanisms are later observed in Fano lasers with fast modulation of the nanocavity frequency. Different modulation mechanisms, such as the free carrier effect and thermal effect, are illustrated. This chapter estimates the static and dynamic frequency shifts of nanocavities and simulates the Fano lasers' response, observing and analyzing pulse generation characteristics. The experimental details of pulse generation and comparisons with conventional Fabry–Pérot lasers using gain tuning are presented.

Chapter 4 investigates Fano lasers with an active external feedback cavity. Equations for feedback Fano lasers and their lasing conditions are derived, revealing the emergency of multiple lasing modes. This chapter thoroughly investigates these modes, examining their responses to tuning the nanocavity frequency and exploring variations under different feedback strengths and external cavity lengths. The multi-section model from Chapter 2 is extended to feedback Fano lasers for numerical simulations, where bistability is observed. This chapter also demonstrates flip-flop functionality in a feedback Fano laser with modulated pulses, examining triggering

conditions for mode switching and analyzing their relation with modulation pulse characteristics. The energy costs associated with photonic crystal nanocavity structures are estimated. Finally, experimental measurements on feedback Fano lasers are presented and compared with the outcomes from the numerical models.

Chapter 5 shifts focus to the stochastic simulation of semiconductor lasers, a relevant topic as quantum properties become important in nanolasers with low carrier and photon numbers. In this chapter, we employ a method that contrasts with the semi-classical models used previously, instead presenting a purely quantum model. It introduces two stochastic simulation methods: fixed time increment (FTI) and Gillespie's first reaction method (FRM), comparing their principles and computational efficiencies. The dynamics near the lasing threshold are explored, reproducing a "photon burst" phenomenon reported earlier [39]. Subsequently, the turn-on transient dynamics and their associated photon statistical properties are analyzed. The chapter concludes by comparing FTI and FRM with analytic models of nanolasers in the near-threshold region.

Fano lasers

2.1 Introduction

Semiconductor integrated circuit fabrication techniques have significantly improved over the past two decades. With these improvements, it is now feasible to construct high-quality factor nanocavities (NC) with discrete modes on a chip. One innovative approach involves coupling the NC to a waveguide (WG), allowing the resonance of the discrete NC mode to interact with the continuum of modes of the WG. This unique interplay between discrete and continuous states was first conceptualized in atomic physics by Ugo Fano, who explained the appearance of asymmetric resonance lineshapes, now recognized as Fano resonances [40].

Optical WGs for on-chip photonic platforms are conventionally realized using silicon wire structures [41]. An alternative approach is using line-defect structures within photonic crystals (PhCs). This article delves deeper into the system based on the PhC structure, with further details to be discussed in Subsection 3.5.2. When considering optical cavities, introducing hole defects into PhC structures creates nanometer-scale cavities where light can form standing waves inside. These cavities can be positioned adjacent to the WGs, as depicted in Figure 2.1. In those structures, a portion of the light field traveling through the WG can couple into the NC. The light then out-couples from the NC with a phase shift, interfering with the original wave propagating through the WG [42]. By meticulously tuning this phase shift, which is characterized by a parameter q in the Fano formula [43], one can modulate reflection and trans-
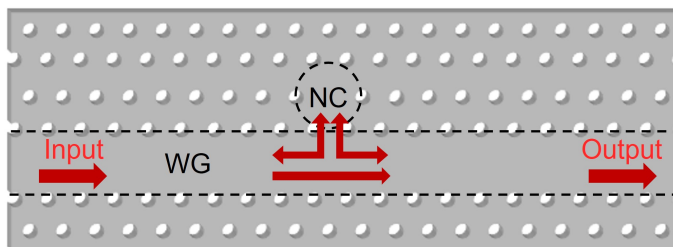
Figure 2.1. Schematic of a line-defected waveguide (WG) and a hole-defected nanocavity (NC) in a photonic crystal. The red arrows indicate the direction of light propagation.

mission as functions of the detuning between light mode and the NC's frequency, giving rise to the distinctive Fano resonance lineshape, as shown in Figure 2.2(a). The frequency-dependent characteristics exhibited by this resonance, especially its narrow linewidth, can effectively serve as an optical latch to control light transmission by slightly shifting the Fano resonance spectrum. Such features have paved the way for observing diverse phenomena and exploring potential applications, notably in optical filters and switches [42]. Figure 2.2(b) and (c) show an example of a Fano-based optical switch. By introducing the parameter q [43], a substantial contrast can be achieved between the low and high transmission points of the spectrum within a narrow detuning range. When an external pump excites the NC, the resonance undergoes a shift (due to carrier-induced nonlinear dynamics, which will be elaborated in section 3.3.1). As a result, the light traveling inside the WG (denoted as a probe light in Figure 2.2(b)), initially at a low transmission level, shifts to a high transmission state and passes through the switch.

Another intriguing concept emerging from this field is utilizing this frequency-dependent mirror to create a laser called a Fano laser [30, 44]. A schematic of a Fano laser can be seen in Figure 2.3. Its design includes a waveguide (WG) with one open end adjacent to a nanocavity (NC). At the closed end, there is a broadband mirror, which can be implemented using various techniques such as a Dielectric Bragg Reflector (DBR) [45, 46], a metallic mirror [47], or even a photonic crystal bandgap [5]. On the opposite end, where the coupling takes place, a Fano mirror is formed. The laser cavity is thus defined by the space enclosed by the broadband mirror and the Fano mirror within the WG. By introducing active material into the WG, the optical field can attain gain, allowing amplification to achieve lasing.

Due to this frequency-dependent mirror, Fano lasers exhibit characteristics that differ from traditional Fabry–Pérot (FP) lasers [30, 44]. A primary distinction from FP lasers is that, for effective lasing in Fano lasers, the WG length must be carefully selected to ensure the longitudinal mode frequency aligns closely with the resonance frequency of the NC. This results in the laser cavity's quality factor (Q-factor) being influenced by the cavity length, as illustrated in Figure 2.4(a) [44]. Another notable trait of Fano lasers is that, as the lasing mode is established, most of the optical field becomes localized within the NC, depicted in Figure 2.4(b) [37]. The laser's emitted field can exit not only through the right side of the main WG (Through-port (TP) shown in Figure 2.3); it also disperses vertically from the NC or another ancillary WG coupled to the opposite side of the NC (Cross-port (CP) shown in Figure 2.3). Additionally, this field concentration within the NC leads to diminished overlap between the optical field and the active materials. This lessens the impact of random phase fluctuations stemming from spontaneous emission, resulting in a narrower linewidth for Fano lasers [37].

The intensity concentration in the NC paves the way for efficient laser modulation. A modest optical power or electrical current can effectively shift the NC's refractive index [48]. This capability allows for the generation of pulses through cavity dumping and Q-switching [38] (as discussed in Section 3.2) with minimal energy consumption. Additionally, Fano lasers are theoretically predicted to have remarkable modulation
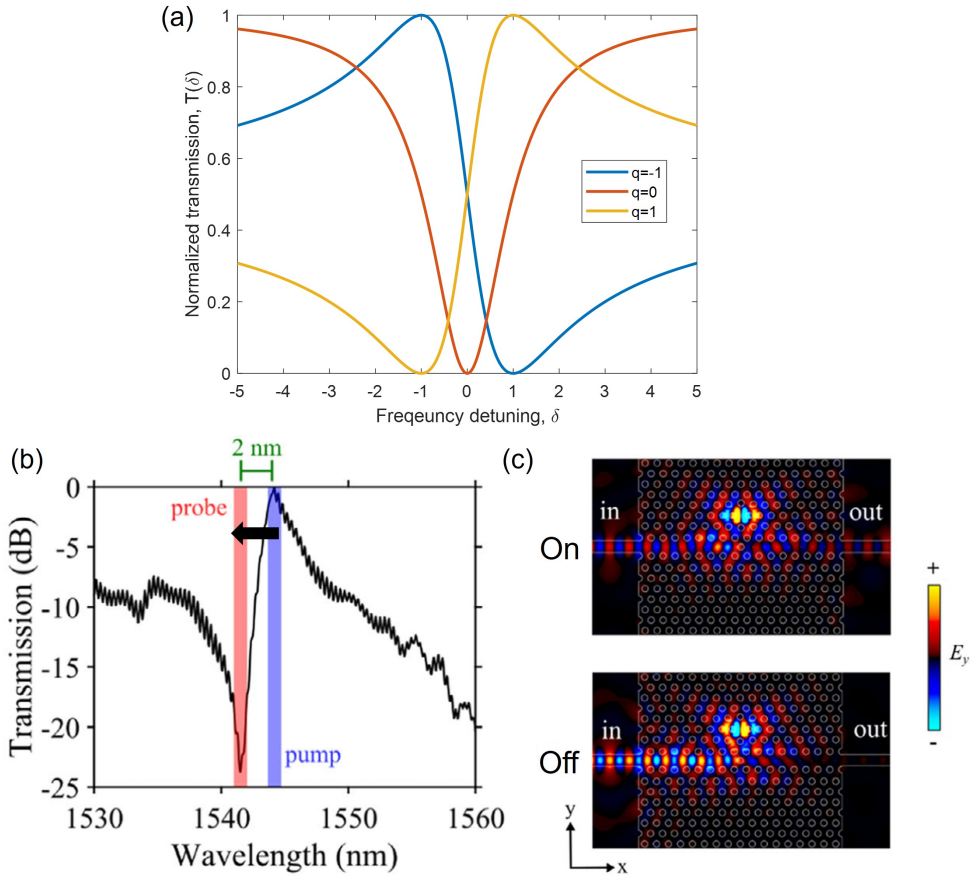
Figure 2.2. (a) Transmission spectrum of Fano resonance, where q is the asymmetry parameter. (b) Measured transmission spectrum of the Fano-based optical switch. The probe light's wavelength is initially positioned at the lowest transmission point and transitions to the highest point upon injection of the pump light. Reprinted from [42]. (c) Normalized electric field distribution, computed using 3D-FDTD, at both the highest and lowest points of transmission. Reprinted from [42].

speeds [31, 32]. Figure 2.5(a) depicts the modulation response to the nanocavity resonance frequency. When the external modulation frequency is below both the mirror's linewidth (γ_T) and the laser's round-trip time (γ_L), Fano lasers' lasing frequency can effectively track the changes of NC detuning. As a result, outputs from both TP and CP exhibit a pronounced frequency modulation response and show the resonance at the relaxation oscillation (RO) frequency. Conversely, when the external modulation frequency surpasses the mirror's linewidth and inverse of the laser's round-trip time, the response of Fano lasers gradually increases to unity instead of diminishing [32, 44].
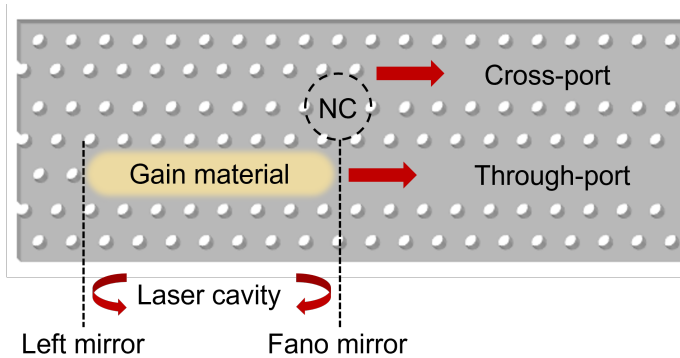
Figure 2.3. Schematic of a Fano laser implemented in a photonic crystal slab. A nanocavity (NC) is side-coupled to a waveguide (WG), forming a Fano mirror and creating a laser cavity in conjunction with a left mirror. The through-port is the port from which the light is out coupled from the main WG. An ancillary WG can be coupled to the opposite side of the NC, being the cross-port. Red arrows indicate the direction and flow of light fields.

This occurs because the field inside the NC can change with the external modulation frequencies via adiabatic frequency conversion [49]. Such features could enable the response time of lasers to reach the femtosecond scale [44], significantly surpassing the 60 GHz seen in today's best-performing lasers [50]. Conversely, at reduced modulation frequencies, Fano lasers exhibit additional damping [32]. This behavior arises from the filtering properties of the Fano mirror, enhancing the threshold for critical feedback and bolstering resistance against instability [34]. The Fano mirror can act as a saturable absorber when accounting for an active NC. Within the NC, carriers undergo excitation and depletion, leading to cyclical increases and decreases in reflectivity [33]. This dynamic results in Q-switching and subsequent self-pulsing. Simulations have demonstrated the emission of a GHz repetition-rate pulse train with pulsewidth on the order of picoseconds, as depicted in Figure 2.5(b) and (c).

2.2 Modeling of Fano lasers

2.2.1 Semiconductor nanolaser rate equations

Semiconductors utilize the recombination of electrons and holes within the active region to produce photons. Semiconductor laser rate equations present a different case than atomic laser systems, where the carrier lifetime is substantially shorter than the photon lifetime, allowing for the adiabatic elimination of carrier and polarization variations in laser rate equations. In semiconductor lasers, carrier lifetime is almost in the same order as photon lifetime, placing them in the category of class B lasers [51], necessitating using two variables to describe lasers' behavior.
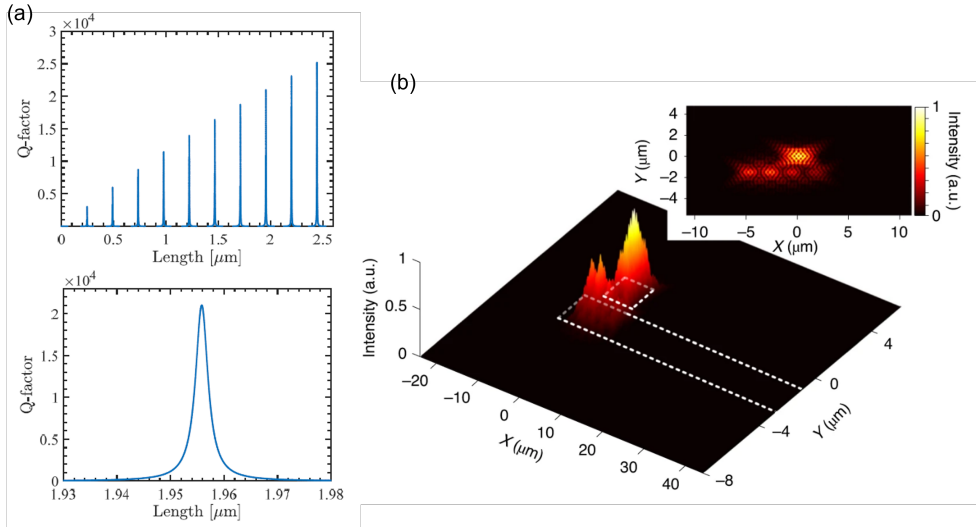
Figure 2.4. (a) Variation of the Quality factor (Q-factor) with Fano laser cavity length. The upper panel is the long-range variation. The lower panel is a detailed view of one specific mode. Reprinted from [44]. (b) Calculated electric field intensity profile of a Fano laser, illustrating a high intensity within the nanocavity. The white dashed lines indicate the nanocavity (upper square) and the waveguide (lower rectangle). Reprinted from [37].

For standard single-mode semiconductor lasers, the dynamics can be described by two coupled nonlinear equations that account for the dynamics of carrier density N and the photon density N_p [52]:

$$\frac{dN}{dt} = R_p - \frac{N}{\tau_c} - v_g g N_p \tag{2.1}$$

$$\frac{dN_p}{dt} = \Gamma v_g g N_p + \Gamma \beta R_{sp} - \frac{N_p}{\tau_p} \tag{2.2}$$

Here R_p is the pumping rate, and τ_c is the carrier lifetime. The group velocity is given by $v_g = c/n_g$, where c is the speed of light in vacuum, and n_g is the group index, Additionally, g is the optical gain. The confinement factor, $\Gamma = V_a/V_p$, is defined as the ratio of the active material region volume V_a to the overall mode volume $V_p = AL$, where A is the cross-section of the WG mode and L is the length of the optical cavity. The spontaneous emission factor, β, is the proportion of spontaneous photons that enter the lasing mode. The spontaneous emission rate is given by R_{sp}, and τ_p is the photon lifetime. In subsequent calculations, we will ignore spontaneous emission unless explicitly stated, given our concentration on the behavior above the lasing threshold. Spontaneous emission minimally influences the dynamics above the threshold, where stimulated emission dominates the lasing mode.

(a)

(b)

(c)
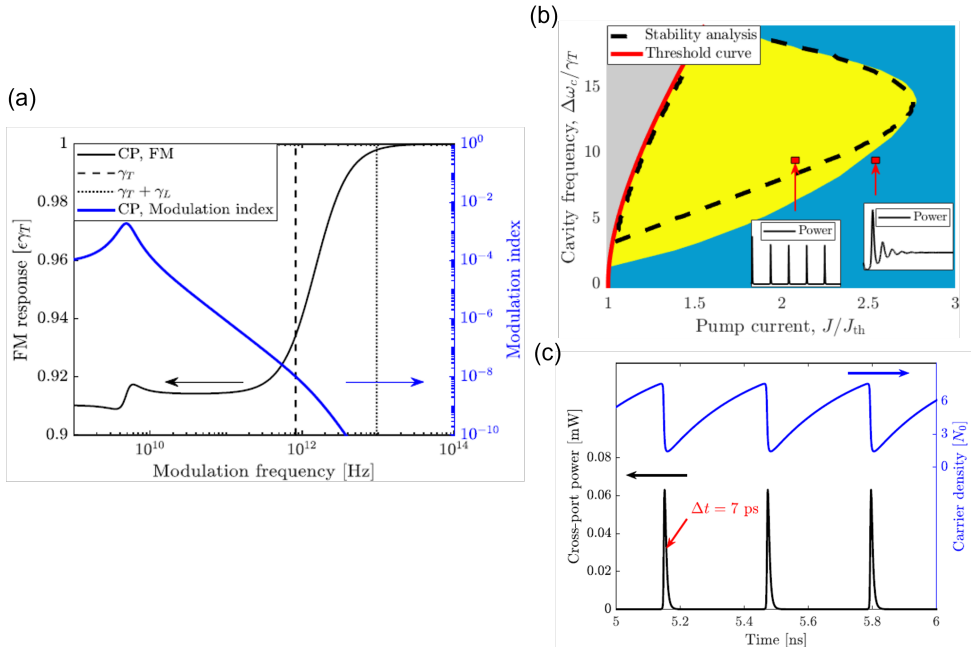
Figure 2.5. (a) Frequency response (FM) (black) and modulation index (blue) with respect to the nanocavity resonance frequency. The FM response is the maximum excursion of the optical frequency, normalized to the modulation amplitude $\epsilon\gamma_T$. The modulation index is the maximum power amplitude normalized to the steady-state power output. Reprinted from [44]. (b) Phase diagram of Fano laser output as determined by pump current and nanocavity frequency. In the gray region, the laser operates below the threshold. In the blue region, the output is a continuous wave, while in the yellow region, the output exhibits self-pulsing. The dashed black line shows the boundary of the self-pulsing regime predicted by stability analysis. Reprinted from [33]. (c) Temporal variation of the output power and carrier density of Fano laser in the self-pulsing state. Reprinted from [33].

In principle, the optical gain function $g(\omega, N)$ is a function of mode frequency and carrier density. Here, assuming the cavity mode bandwidth is much narrower than the gain function profile, g can be approximated solely relying on N. For bulk material, when N is not too large and the effects of gain compression can be ignored, g can be further approximated as a linear function: $g \approx g(N) = g_n(N - N_0)$. Here, N_0 is transparency carrier density, the neutral point where neither gain nor lose as light passes through. g_n is the differential gain coefficient.

The carrier lifetime τ_c encompasses the combined effects of spontaneous emission and non-radiative decay mechanisms such as interactions with lattice defects and Auger recombination [53], which can be expressed as the relation: $1/\tau_c = 1/\tau_{sp} + 1/\tau_{nr}$ [52]. The photon lifetime τ_p is determined by the internal absorption loss within the cavity α_i as well as the losses resulting from transmission at the cavity's mirrors α_m,

which can be expressed as [52]:

$$\frac{1}{\tau_p} = v_g(\alpha_m + \alpha_i) = \frac{v_g}{2L} \ln\left(\frac{1}{|r_L|^2 |r_R|^2}\right) + v_g \alpha_i \tag{2.3}$$

Here, the coefficients r_L and r_R are the reflection coefficients of the left-hand side (LHS) and right-hand side (RHS) mirrors, respectively.

According to Equations 2.1 and 2.2, the carrier density in the semiconductor laser increases due to pumping but decreases because of non-radiative recombination and stimulated emission. This stimulated emission, in turn, raises the photon population. However, the number of photons also decreases due to cavity loss. The energy in the semiconductor laser therefore oscillates between these two reservoirs, eventually reaching an equilibrium (if a stable state exists), as demonstrated in Figure 2.6 (all the simulation parameters used in this chapter are listed in Table 2.1, unless specified otherwise). Above the threshold, in a steady state, the carrier density N remains clamped at a constant value irrespective of the pumping level. This constant value is the threshold carrier density N_{th} that balances optical gain and cavity loss.
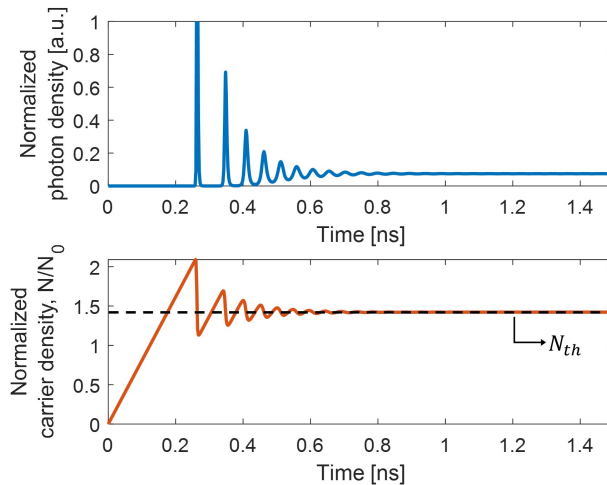
Figure 2.6. Example of turn-on transients of photon density (upper panel) and carrier density (lower panel) in a semiconductor laser. The carrier density clamped at its threshold value. The pumping rate used is $R_p = 4 \times 10^{31}$ s^{-1}, and the reflectivity of the right-hand side mirrors is $|r_R| = 0.95$.

2.2.2 Temporal coupled-mode theory and Fano mirror

The temporal coupled-mode theory (CMT) [54] describes the dynamics of a field coupled with a cavity. This is especially relevant for Fano lasers, composed of a

WG coupled to an NC, as shown in Figure 2.7. Considering a single-mode WG side connected to an NC. The field propagating inside the WG can couple between WG and NC via either the left or the right ports. These two ports are assumed to have equivalent coupling rate γ_c, as shown in Figure 2.7. The CMT equation can be written as [30]:

$$\frac{dA_c}{dt} = -(i\delta(\omega) + \gamma_t)A_c + \sqrt{\gamma_c}e^{i\theta_1}S_L^+ \tag{2.4}$$

$$S_L^- = r_B S_L^+ + \sqrt{\gamma_c}e^{i\theta_1}A_c \tag{2.5}$$

$$S_R^- = -it_B S_L^+ + \sqrt{\gamma_c}e^{i\theta_2}A_c \tag{2.6}$$

Here, A_c is the amplitude of the field inside the NC, while $S_{L(R)}^{+(-)}$ is the amplitude of the propagating wave at the termination plane of the WG beneath the NC. The subscript $L(R)$ refers to the position at LHS (RHS) of the WG, with the superscript $+(-)$ indicating the inward(outward) direction with respect to the NC. The term $\delta(\omega) = \omega_c - \omega$ is the detuning between the mode and the NC resonance frequency ω_c. Additionally, γ_t is the total decay rate of the NC, whereas γ_c is the coupling rate between the NC and the WG. For an NC, besides the coupling decay, other decay channels also exist. These include vertical out-coupling, characterized by the rate γ_v, and intrinsic loss, characterized by the rate γ_i (the intrinsic loss rate encompasses decay not directed into the WG mode, such as absorption and in-plane losses.). This leads us to $\gamma_t = \gamma_c + \gamma_v + \gamma_i$. Using the quality factor (Q-factor) as $Q_x = \omega/(2\gamma_x)$, we can also have the relation: $1/Q_t = 1/Q_c + 1/Q_v + 1/Q_i$.
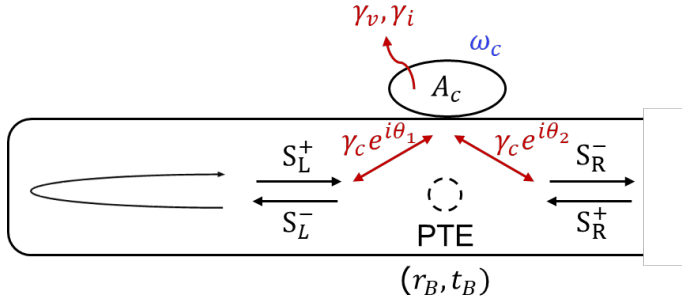
Figure 2.7. Schematic of a Fano laser and the variables used in the temporal coupled-mode theory.

The parameter $\theta_{1(2)}$ defines the coupling phase between the fields $S_{1(2)}$ and the NC. A partially transmitting element (PTE) within the WG is typically positioned near the NC, often realized with a hole defect [42]. This PTE introduces a partial reflection surface, influences the coupling phase, and subsequently modifies the Fano lineshape. The coefficients associated with the reflection and transmission of the PTE are represented by r_B and t_B, respectively. By using energy conservation and time-reversal symmetry [55], we can derive a relationship between the coupling phase and

the coefficients of the PTE [42]:

$$e^{i(\theta_1 - \theta_2)} = \frac{1}{it_B}\left(e^{i2\theta_1} + r_B\right) \tag{2.7}$$

and

$$\cos\left(2\theta_1\right) = -r_B \tag{2.8}$$

From the above formulations, it becomes evident that in the absence of the PTE, θ_1 and θ_2 assume a value of $\pi/4$. By redefining our reference plane such that $e^{i\theta_1}A_c$ transforms to A_c, we can eliminate θ in CMT equations by introducing a factor of i before S_L^+ in Equation 2.4. Note that there is also a factor of i between S_R^- and S_L^+ in Equation 2.6, suggesting that the optical path spanning the coupling region contributes an additional phase shift of $\pi/2$.

Upon achieving a steady state in the system (where $da/dt = 0$), and under the assumption of negligible intrinsic loss, the reflection and transmission coefficients of the Fano mirror can be derived as $r_F(\omega) = S_L^-/S_L^+$ and $t_F(\omega) = S_R^-/S_L^+$ respectively. This leads us to the following expressions [30]:

$$r_F(\omega) = \frac{i\gamma_c}{i\delta(\omega) + \gamma_t} \tag{2.9}$$

$$t_F(\omega) = \frac{\delta(\omega) - i\gamma_v}{i\delta(\omega) + \gamma_t} \tag{2.10}$$

These equations define the Fano mirror's behavior. As demonstrated in Figure 2.8(a), the reflectance, $|r_F(\omega)|^2$ and the phase, $Arg[r_F(\omega)]$ of the Fano mirror is a function of ω. The Fano mirror exhibits a Lorentzian lineshape in reflection with its bandwidth dictated by γ_t. When the mode frequency resonates with the NC, where $\delta(\omega) = 0$, the reflectance reaches its peak value and imposes a $\pi/2$ phase shift in the field. Figure 2.8(b) demonstrates the corresponding transmittance and phase. Note that when the mode frequency is far detuned, the Fano mirror becomes transparent, causing the transmitted field to undergo a $-\pi/2$ phase shift, as described in Equation 2.6.

At first glance, one might assume that the dynamics of a Fano laser can be captured by merely replacing the reflectivity of a conventional broadband mirror with that of a Fano mirror at the laser oscillation frequency in the FP laser equations. However, given the frequency-dependent characteristics of the Fano mirror, the reflectance and phase are not static. They fluctuate over time until the lasing frequency stabilizes. This introduces complexity as the photon number cannot be represented by Equation 2.2, given that the photon's lifetime is also a time-dependent function. A feasible strategy to tackle this problem is first solving the steady-state solution for the lasing conditions. After that, one could implement a small perturbation expansion to study the dynamics around this equilibrium.

The steady-state solution of Fano lasers can be obtained by solving the lasing oscillation conditions (OC), which are the criteria for phase-matching and gain-loss balance [30]:

$$Arg[r_L] + Arg[r_F(\omega_s)] + \frac{2L}{v_g}\omega_s = 2m\pi \tag{2.11}$$
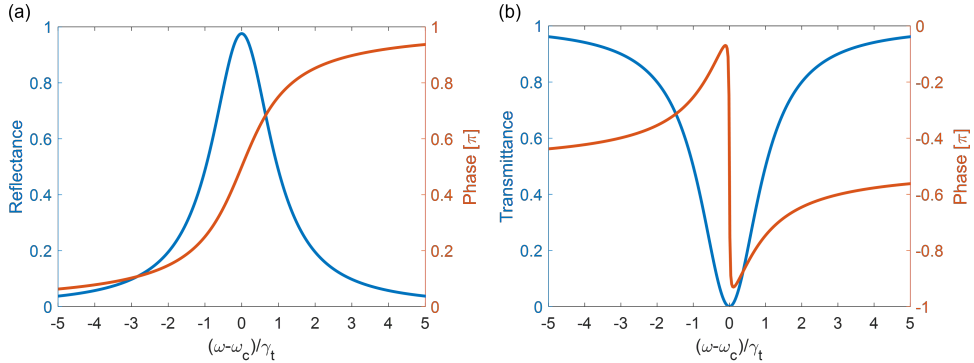
Figure 2.8. Frequency dependence of the (a) reflectance and (b) transmittance (blue lines), and their corresponding phase (red lines) of the Fano mirror as a function of detuning.

$$\Gamma g_n(N_s - N_0) = \frac{1}{2L} \ln\left(\frac{1}{|r_L|^2 |r_F(\omega)|^2}\right) + \alpha_i \tag{2.12}$$

Here, ω_s and N_s represent the steady-state mode frequency and carrier density, respectively. As N is clamped when the laser surpasses the lasing threshold, N_s is concurrently defined as the threshold carrier density. The integer m signifies different longitudinal modes. Figure 2.9(a) shows how N_s and ω_s evolve with L for various longitudinal modes. When ω_s match the WG round-trip $2m\pi$ phase shift and perfectly align with the NC frequency ω_c, the field perceives the maximal reflectance from the Fano mirror, resulting in minimized cavity mirror loss, corresponding to the lowest threshold point in the figure. Near these specific cavity lengths, ω_s exhibits a flat region insensitive to cavity length variations. This "frequency pinned" phenomenon starkly contrasts with the behavior of FP lasers, a distinction further highlighted by experimental measurements in Figure 2.9(b).

2.3 Numerical simulations of Fano lasers

2.3.1 Ordinary differential equation (ODE) approach

As mentioned in the last section, it is possible to expand the laser oscillation conditions around their steady-state solutions to derive small perturbation equations [30]. We can express the complex wavenumber $k(\omega, N)$ as:

$$k(\omega, N) = \frac{n}{c}\omega - \frac{i}{2}\left(\Gamma g_n(N - N_0) - \alpha_i\right) \tag{2.13}$$
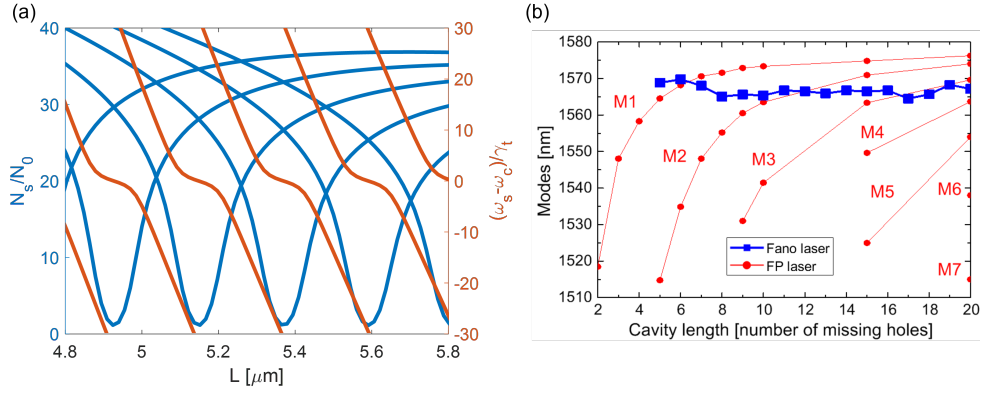
Figure 2.9. (a) Steady-state carrier density (blue lines) and mode frequency (red lines) as functions of cavity length for multiple longitudinal modes.(b) Experimental measurement of Fano laser modes wavelength relative to cavity length, compared with a Fabry–Pérot (FP) laser, M1–M7 denote the mode order. Reprinted from [44].

When no nonlinear effects are present, the refractive index n remains constant, and k can be expanded near the point (ω_s, N_s):

$$
\begin{aligned}
k(\omega, N) &\approx k(\omega_s, N_s) + \frac{\partial k}{\partial \omega}(\omega - \omega_s) + \frac{\partial k}{\partial N}(N - N_s) \\
&= k(\omega_s, N_s) + \frac{n}{c}(\omega - \omega_s) - \frac{i}{2}\Gamma g_n(N - N_s)
\end{aligned}
\tag{2.14}
$$

At the steady state, the spectral density of the propagating field $E^{+(-)}(\omega)$ is governed by the following relations:

$$
E^+(\omega) = r_L \exp\left(i2k(\omega, N)L\right) E^-(\omega) \tag{2.15}
$$

$$
E^-(\omega) = r_F(\omega)E^+(\omega) \tag{2.16}
$$

From these, we can deduce:

$$
\frac{1}{r_L} \exp\left(-i2k(\omega, N)L\right) = r_F(\omega) \tag{2.17}
$$

Substituting Equation 2.14 into 2.15, we have:

$$
\begin{aligned}
E^-(\omega) &= r_F(\omega_s)E^+(\omega) \\
&\approx r_F(\omega_s)\left(1 - L\Gamma g_n(N - N_s) - i\frac{2nL}{c}(\omega - \omega_s)\right) E^+(\omega)
\end{aligned}
\tag{2.18}
$$

Applying the Fourier transform converts the term $-i(\omega - \omega_s)E^+(\omega)$ into $dS_L^+(t)/dt$. Equation 2.18 then becomes:

$$
\frac{dS_L^+(t)}{dt} = \frac{c}{2nL}\left(L\Gamma g_n(N - N_s) - 1\right) S_L^+(t) + \frac{c}{2nL}\frac{1}{r_F(\omega_s)}S_L^-(t) \tag{2.19}
$$

Furthermore, to establish a link between N_P and S_L^+, we introduce the parameter σ_s, which is the ratio of total photon number to the field intensity. At steady-state, it takes the form [36, 56]:

$$\sigma_s = \frac{2\epsilon_0 n n_g}{\hbar \omega_s} \left(\frac{(|r_L| + |r_F(\omega_s)|)(1 - |r_L||r_F(\omega_s)|)}{(\Gamma g - \alpha_i)|r_L|} + \frac{c}{n\omega_s} \frac{|r_L|}{|r_F(\omega_s)|} \text{Im}\left(r_F(\omega_s) \right) \right)$$
(2.20)

with the relation $N_p = \sigma_s |S_L^+|^2 / V_p$. In conjunction with Equation 2.19, 2.5, and 2.1, there is a set of three equations for three variables S_L^+, A_c, and N to solve for Fano laser dynamics.

2.3.2 Iterative approach with fixed time steps

The ODE approach, based on small perturbations around the steady state, inherently comes with a limitation when dealing with the laser dynamic involved in the large signal response. An alternative strategy to circumvent this problem is to adopt iterative approaches. Assuming the field behaves like a plane wave propagating within the WG, the following relationship can be set:

$$S_L{}^+(t + \tau_{rt}) = r_L S_L{}^-(t) \exp\left(i2k\left(\omega(t), N(t) \right) L \right)$$
(2.21)

and

$$S_L{}^-(t) = \sqrt{\gamma_c} A_c(t)$$
(2.22)

Here, $\tau_{rt} = 2L/v_g$ is the round-trip time of the laser cavity, used as the iteration time step.

There are several methods to convert ODEs into time difference equations (TDEs). Here, we use the straightforward Euler method, transforming the derivative term into a finite difference by $dx/dt = (x_{n+1} - x_n)/\tau$ [57]. Given this, Equations 2.1 and 2.4 become:

$$N(t + \tau_{rt}) = N(t) + \tau_{rt} \left(R_p - \frac{N(t)}{\tau_c} - v_g g_n \left(N(t) - N_0 \right) \frac{\sigma_s |S_L{}^+|^2}{V_p} \right)$$
(2.23)

$$A_c(t + \tau_{rt}) = A_c(t) + \tau_{rt} \left(-\left(i\delta(\omega) + \gamma_t \right) A_c(t) + i\sqrt{\gamma_c} S_L{}^+(t) \right)$$
(2.24)

Given that this model considers only a single spatial section, we use the term "Single-section Euler method" (S-E) in the later content.

For more accurate results, one can directly integrate Equations 2.1 and 2.4 to obtain a more precise finite difference formulation. If the time step is sufficiently small compared to the system's evolution, we can assume that $S_L^+(t)$ does not vary significantly and can thus be approximated as constant within a single time step. Equations 2.4 and 2.1 then adopt the form $dx(t)/dt = -ax(t) + b$, which has the solution $x(t + \tau) = \frac{b}{a} + \left(x(t) - \frac{b}{a} \right) e^{-a\tau}$. This gives us:

$$A_c\left(t + \tau_{rt} \right) = \left(A_c\left(t \right) - \frac{C_b}{C_a} \right) \exp\left(-C_a \tau_{rt} \right) + \frac{C_b}{C_a}$$
(2.25)

where

$$
\begin{aligned}
C_a &= i\delta\left(\omega\right) + \gamma_t \\
C_b &= i\sqrt{\gamma_c}S_L^+\left(t\right)
\end{aligned}
\tag{2.26}
$$

Similarly, for the carrier density equation:

$$
N\left(t + \tau_{rt}\right) = \left(N\left(t\right) - C_d\right)\exp\left(-\left(\frac{1}{\tau_c} + C_n\right)\tau_{rt}\right) + C_d
\tag{2.27}
$$

where

$$
\begin{aligned}
C_n &= v_g g_n \frac{\sigma_s|S_L^+\left(t\right)|^2}{V_p} \\
C_d &= \frac{R_p + C_n N_0}{\frac{1}{\tau_c} + C_n}
\end{aligned}
\tag{2.28}
$$

This "Single-section integration method" (S-I) is expected to exhibit superior accuracy and numerical stability compared to the previous S-E method.

2.3.3   Multi-section approach

In the iterative method detailed in subsection 2.3.2, the computation is based solely on a specific site in the WG located directly below the NC, and the carrier density is presumed to be uniform across the WG. Challenges arise when the pump is non-uniform (as detailed in Chapter 4) or when the diffusion of the carrier density becomes essential. Such scenarios can lead to non-uniform carrier density and field distribution. Another limitation of the single-site iterative model is its time step. The value at that specific site can only be updated when the field completes one round trip within the lasing cavity. As a result, the time step cannot be arbitrarily chosen; instead, it must correspond to the round-trip time, which is dictated by the cavity length. This constraint becomes an issue when modeling the rapid dynamic shifts of a system where the time scale is less than τ_{rt}, compromising the resolution of the dynamics.

To overcome these problems, one solution is to divide the WG into multiple sections. We divide the WG into M sections with each section boundary defined as a site. The multi-section model is illustrated in Figure2.10. From the LHS mirror to the NC, the mth site is denoted as $m = 1, 2...M$, The last site, $M + 1$ below the NC, is equal to the subscript L used before. Fields and carrier densities at each site are represented as $S_m(t)$ and $N_m(t)$, respectively. Consequently, the propagation equation 2.21 becomes:

$$
S_m^+\left(t + \tau_d\right) = \begin{cases} r_L S_1^-\left(t + \tau_d\right) \\ \left(m = 1\right) \\ S_{m-1}^+\left(t\right)\exp\left(ik\left(\omega, N_{m-1}(t)\right)v_g\tau_d\right) \\ \left(2 \leq m \leq M + 1\right) \end{cases}
\tag{2.29}
$$

$$S_m^- (t + \tau_d) = \begin{cases} S_{m+1}^- (t) \exp \left(ik \left(\omega, N_{m+1}(t) \right) v_g \tau_d \right) \\ (1 \leq m \leq M) \\ \sqrt{\gamma_c} A_c (t + \tau_d) \\ (m = M + 1) \end{cases} \tag{2.30}$$

where $\tau_d = d/v_g$ is the time taken to traverse a section of length d. For N_m, the equation is:

$$N_m (t + \tau_d) = (N_m (t) - C_d) \exp \left(- \left(\frac{1}{\tau_c} + C_n \right) \tau_d \right) + C_d \tag{2.31}$$

The coefficients are:

$$\begin{aligned} C_n &= v_g g_n \frac{\sigma_0 \left(|S_m^+ (t)|^2 + |S_m^- (t)|^2 \right) d}{V_d} \\ C_d &= \frac{R_p + C_n N_0}{\frac{1}{\tau_c} + C_n} \end{aligned} \tag{2.32}$$

Here, $\sigma_0 = 2\epsilon_0 n n_g / (\hbar \omega_s)$ is the prefactor of the photon number-amplitude parameter in Equation 2.20. $V_d = (d/L) V_p$ is the section mode volume. This "multi-section method" (MS) presumes S_m and N_m are uniformly distributed within each section.
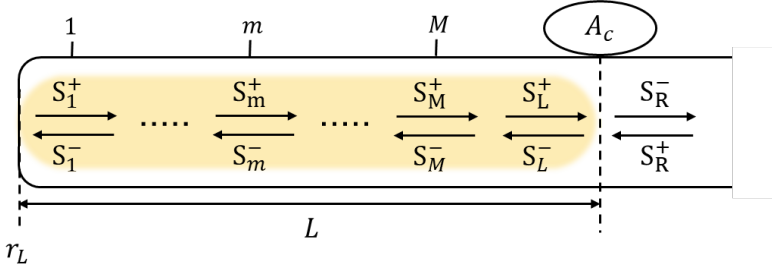
Figure 2.10. Schematic of the multi-section model. The WG is divided into M sections. The light yellow region represents the gain material.

The MS approach provides an approach to incorporate the effects of carrier diffusion. The diffusion effect on N can be described by the diffusion term $D\nabla^2 N_m$. Utilizing the forward Euler scheme, this can be translated into its finite difference representation:

$$D\nabla^2 N_m \rightarrow D \frac{N_{m+1} - 2N_m + N_{m-1}}{d^2} \tag{2.33}$$

Here, D represents the diffusion coefficient. With this representation, we can modify Equation 2.31 and 2.32 as follows:

$$N_m (t + \tau_d) = (N_m (t) - C_d) \exp \left(- \left(\frac{1}{\tau_c} + C_n + D' \right) \tau_d \right) + C_d \tag{2.34}$$

$$C_d = \frac{R_p + C_n N_0 + \frac{D}{d^2}\left(N_{m+1}(t) + N_{m-1}(t)\right)}{\frac{1}{\tau_c} + C_n + D'} \tag{2.35}$$

In this context, $D' = 2D/d^2$; it should be noted that at positions $m = 1$ and $M + 1$, D' becomes D/d^2 since we assume the active material is located only within the laser cavity (i.e. not in the side-coupled cavity), resulting in diffusion from only one side at sites 1 and $M + 1$.

When the diffusion rate of carriers is sufficiently large, allowing carriers to spread across the WG within their effective lifetime (i.e., $\sqrt{D\tau_{eff}} \geq L_1$), the distribution of carriers is nearly homogeneous (if the field inside the WG is absent). We can therefore define $D_{uni} = L_1^2/\tau_{eff}$ as the criterion that carriers are able to spread throughout the entire WG. Here, the effective lifetime is defined as:

$$\frac{1}{\tau_{eff}} = \frac{1}{\tau_c} + v_g g_n N_p \tag{2.36}$$

This accounts for both recombination and stimulated emission effects. At steady state, setting the derivative $dN/dt = 0$ in Equation 2.1, we can establish a relationship between τ_{eff} and R_p:

$$\tau_{eff} = \left(\frac{N_s - N_0}{R_P \tau_c - N_0}\right)\tau_c \tag{2.37}$$

However, in the finite difference method, the diffusion length within a single time step τ_d can not exceed the section length d. This leads to the requirement $D \leq D_{\lim} = d^2/(2\tau_d)$. Exceeding this limit may lead to numerical instabilities, as discussed in [58].

Figure 2.11 displays the contour plot illustrating the numerical stability as a function of the number of sections M and the normalized pumping rate R_p/R_{th}. Here, $R_{th} = N_s/\tau_c$ is the threshold pumping rate. The blue line outlines the condition where $D_{uni} = D_{lim}$. Below this line, it is safe to assume a sufficiently high diffusion rate that carriers can diffuse throughout the entire WG within its effective lifetime and still maintain the stability of the MS method. As seen, for a lower pump rate, a finer resolution is achievable. However, at higher pump rates, the effective lifetime is shortened. To assume a uniform distribution of carriers, a higher diffusion rate setting is required. This setting could potentially result in stability issues in the MS method.

The computational time and data storage requirements as functions of M are depicted in Figure 2.12(a). Here, we model a Fano laser with $D = D_{lim}$, setting the total simulation duration to 1.5ns. Both computational time and data storage demand show an exponential increase with M. As M increases to 70, the storage memory requirement has already escalated to 3.6GB. This highlights the substantial storage demands associated with larger M. Nonetheless, one might not necessarily require such a high M. To explore the impact of M, Figure 2.12(b) presents the temporal variation of $N_1(t)$ and the steady-state N_s of $m = 1$ and $M + 1$ with increasing M. The growth rate of N and the final N_s appear to converge as M increases. As seen, N_s stabilizes once M exceeds 10 sections. Note that the steady-state solutions computed
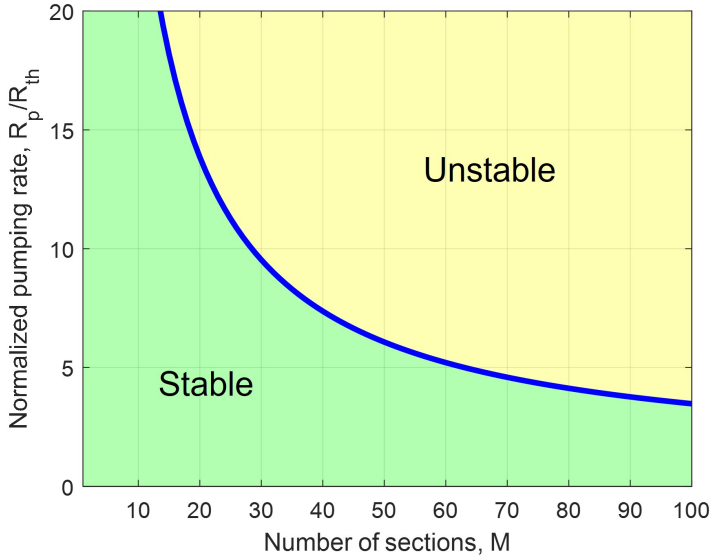
Figure 2.11. Contour plot illustrating numerical stability in relation to the number of sections M and the normalized pumping rate R_p/R_{th}. The blue line indicates the condition $D_{uni} = D_{lim}$. The region below the blue line is stable (light green), while the region above the blue line is unstable (light yellow).

via the MS method exhibit a deviation from the OC solutions. This discrepancy stems from the MS method's ability to account for the non-uniform field distribution within the WG. As a result, N_s values at the LHS end (N_1) differ from those at the RHS end (N_{M+1}), as illustrated in Figure 2.12(c). The OC solutions, calculated assuming all carriers are excited by the mean field and uniformly distributed throughout the WG, have solutions between these two outcomes and fail to capture this feature.

In the investigation of how D affects computational outcomes, Figure 2.13 displays the relative deviations ΔX ($X : N, E_{NC}$) of the computed values from the oscillation condition (OC) solutions. In subfigures (a) and (b), as D increases, ΔE_{NC} exhibits a decreasing trend. This decrease becomes less pronounced once D surpasses D_{uni}. In (c), ΔN demonstrates a decreasing trend for N_{M+1} while it shows the opposite for N_1. As D increases, these curves approach each other. This suggests a diminishing difference in N between the WG's two ends at high diffusion rates.

Notably, when $D = D_{lim}$ (red dashed lines in Figure 2.13), ΔE_{NC} has its value at approximately 5.7%, which contrasts with the relatively smaller 1.13% observed in ΔN. This discrepancy can be attributed to the properties of the Fano laser, where the field intensity is stronger in the NC compared to the WG. The difference in field strength increases the deviation from the homogeneous model at the WG's right end relative to its left end. Given that NC is positioned at the right end, E_{NC} deviates
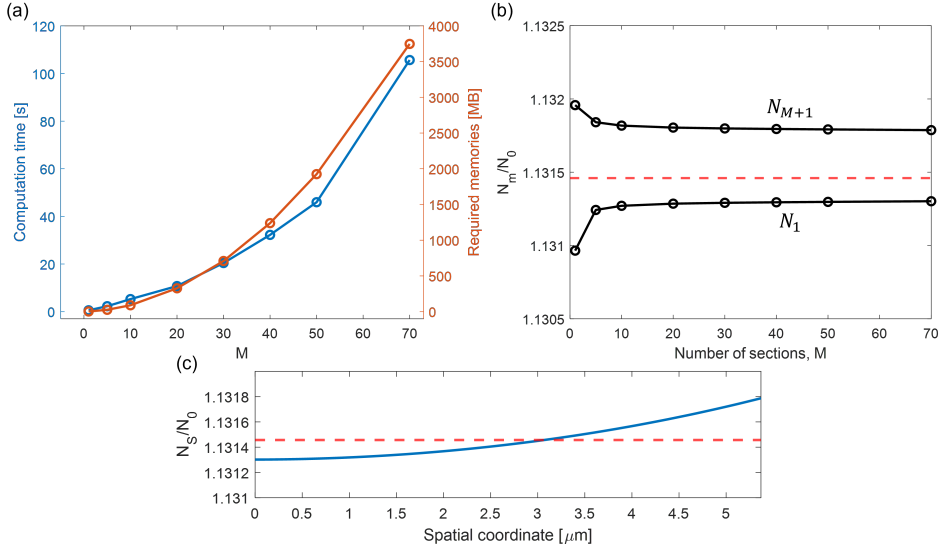
Figure 2.12. (a) Computational time (blue line) and required memories (red line) against section number M, with a fixed simulation duration of 1.5ns. (b) Carrier density against M. The upper black line denotes N_{M+1}, and the lower black line denotes N_1. The central red dashed line is the oscillation condition solution, which assumes a uniform carrier distribution. (c) Spatial carrier density distribution along the WG (blue line) with the starting point positioned at the left mirror. The red dashed line is the OC solution. The pumping rate used is $R_p = 3R_{th}$.

more from the OC solutions (the relative deviation of output power ΔP_{out} shows the same trend as ΔE_{NC}, as evidenced in the SM). The greater deviation in ΔN_{M+1} compared to ΔN_1 further supports this interpretation.

Considering realistic diffusion rates, the uppermost limit for D in InGaAsP is 6.027×10^{-4} m^2/s [59] (a rate we will refer to as D_{real}). At this rate, deviations in ΔE_{NC} can amount to 20%. Conversely, owing to the threshold-clamping phenomenon, ΔN remains relatively modest, only around 1.8% for N_{M+1} and 1.1% for N_1.

Turning to the case with NC detuning, depicted in subfigures (d), (e), and (f), we used an NC detuning value of $\Delta\omega_c = 3\gamma_t$. This can be done in an experiment by adjusting the refractive index of the NC (detailed further in Section 3.3). The introduction of this NC detuning causes a shift in the lasing frequency, accompanied by an effective detuning, which in turn lowers the reflectance of the Fano mirror. Here, the Fano mirror's reflectance drops to around $r_F = 0.8$, which is lower than the left mirror. This leads to reduced power in the NC, making the intensity relatively more uniform than in the zero NC detuning scenario. Consequently, at D_{real}, ΔE_{NC} reduces to roughly 9%. Interestingly, the results indicate that under finite NC detuning, the homogeneous carrier approximation can be more reliable than under zero NC detuning, especially when evaluating output power from the NC or the Fano mirror

output port.
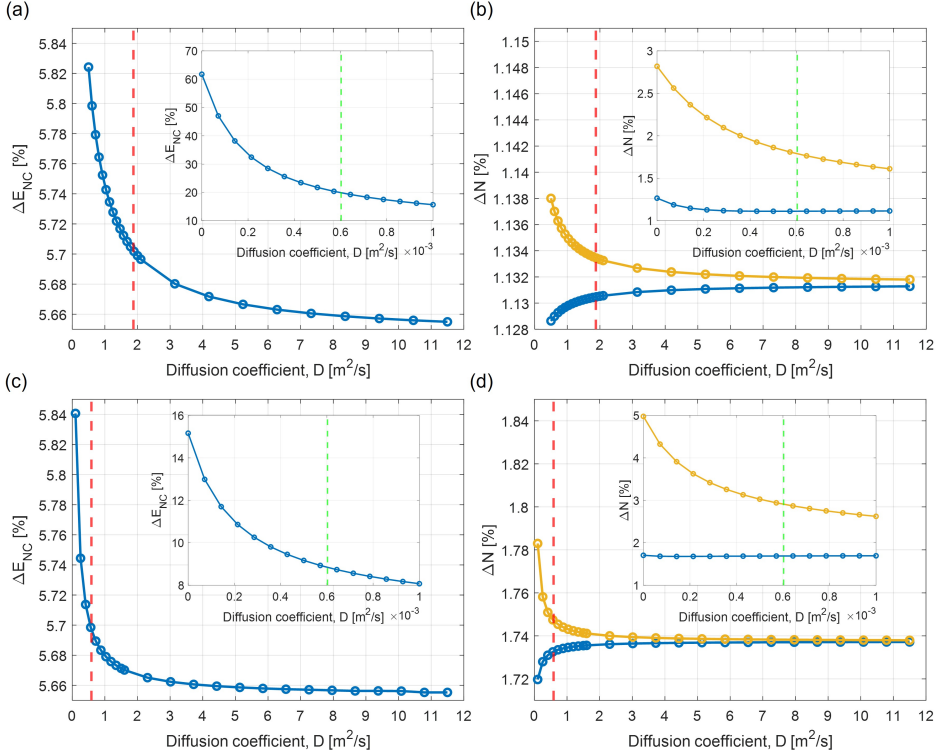
Figure 2.13. Relative deviation ΔX between multi-section approach and lasing oscillation condition solutions as a function of the diffusion coefficient D over a range from 0 to D_{lim} for the pumping rate $R = 3R_{th}$. (a) Deviation of nanocavity energy ΔE_{NC}. (b) Deviation of carrier density ΔN with the yellow line representing N_{M+1} and the blue line representing N_1. (c) and (d) are scenarios when NC detuning is $\Delta \omega_c = 3\gamma_t$. Insets in each subfigure provide zoom-in views for D ranging from 0 to 10^{-3} m^2/s. Red dashed lines mark D_{uni}. Green dashed lines mark D_{real}.

2.3.4   Comparison between various approaches

Figure 2.14 shows the temporal variations of $N(t)$ and $|A_c(t)|^2$ simulated using the ordinary differential equation (ODE), the single-section Euler method (S-E), the single-section integration method (S-I), and the multi-section method either with the small value realistic diffusion coefficient (MS, D_{real}) or with the large limit-value diffusion coefficient (MS, D_{lim}), considering no NC detuning and assuming $R_p = 3R_{th}$. As displayed in Figure 2.14(a), all methods exhibit similar RO frequencies and decay rates and converge to a similar steady-state value. However, distinctions between (MS,

D_{lim}) and the other approaches arise when examining the turn-on delay τ_{DL}. The ODE, S-E, S-I, and (MS, D_{real}) approaches align well with the theoretical turn-on delay for semiconductor lasers [52]. The delay is measured from the moment the laser is turned on until the carrier density N first reaches the steady-state value N_s:

$$\tau_{DL} = \tau_c \ln \left(\frac{R_p \tau_c}{R_p \tau_c - N_s} \right) \tag{2.38}$$

Here, τ_{DL} is calculated assuming that carriers are not influenced by neighboring sites, which is an underlying assumption for the ODE, S-E, and S-I methods. For the (MS, D_{real}), the diffusion rate is so low that carrier dynamics are largely decoupled from neighbor sites; therefore, their turn-on delay also follows Equation 2.38. Although these four methods yield the same τ_{DL}, the ODE approach exhibits a different duration from τ_{DL} to the emergence of the first relaxation oscillation pulse, compared to
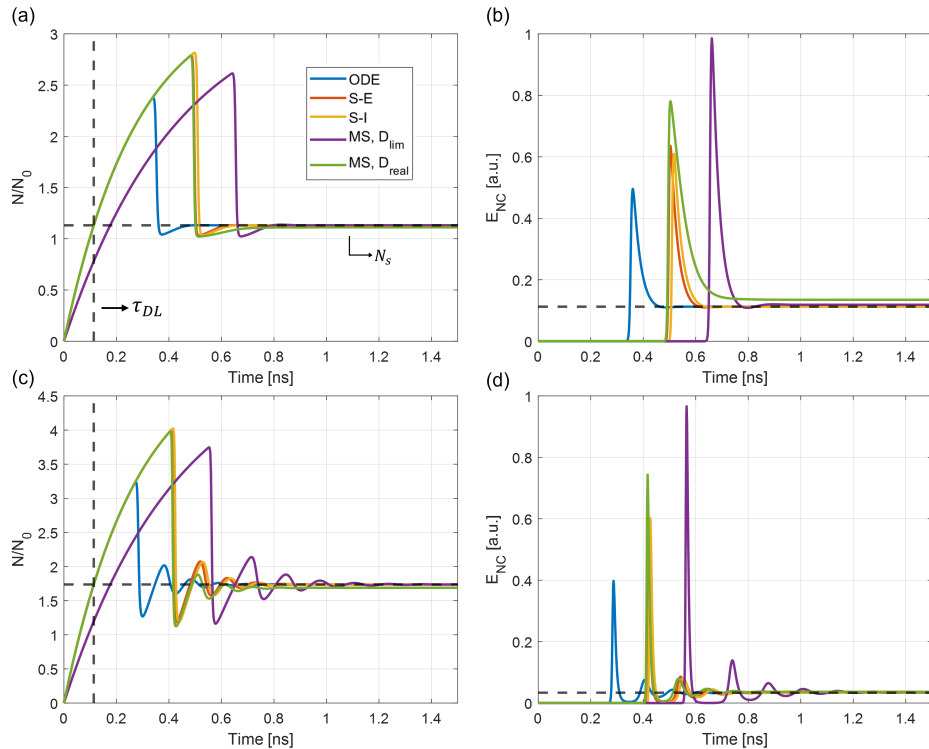
Figure 2.14. Evolution of carrier density N and NC energy E_{NC} over time for different approaches with (a), (b) NC detuning $\Delta \omega_c = 0$ and (c), (d) NC detuning $\Delta \omega_c = 3\gamma_t$. The vertical black dashed lines represent the theoretical turn-on delay τ_{DL} from Equation 2.38. The horizontal black dashed lines represent the OC solutions. The pumping rate used is $R_p = 3R_{th}$.

the S-E, S-I, and (MS, D_{real}) methods. Given the limitations of the ODE method when handling large signal variations, the duration before the first relaxation oscillation pulse it calculates may be as accurate as the durations determined by the other methods. On the other hand, (MS, D_{lim}) shows a longer turn-on delay. This extended delay could arise from the slower carrier accumulation rate due to diffusion effects.

Similar patterns are exhibited in the case $\Delta\omega_c = 3\gamma_t$ (Figure 2.14(c) and (d)). Here, the decreased power within the cavity reduced the decay rate of the RO, making the oscillations more pronounced, in line with predictions made by traditional semiconductor laser models [52]. The investigation of even larger detuning cases can refer to the work [60], which shows the discrepancies between OC, ODE, and S-I methods across broader detuning ranges.

Parameter	Symbol	Value
NC frequency	ω_c	1.215×10^{15} Hz
NC coupling Q	Q_c	500
NC vertical scattering Q	Q_v	10^5
NC internal loss Q	Q_i	86000
WG internal loss	α_i	10 cm^{-1}
LHS mirror reflection coefficient	r_L	-1
Phase and group indices	n, n_g	3.5
Confinement factor	Γ	0.01
Differential gain	g_n	5×10^{-16} m^{-2}
Transparency carrier density	N_0	5×10^{21} m^{-3}
Carrier lifetime	τ_c	0.28 ns
Cross-section of WG mode	A	1.05×10^{-13} m^2
WG length	L	5.37 μm
Threshold pumping rate	R_{th}	3.325×10^{31} m^{-3}s^{-1}

Table 2.1. Simulation parameters used in Chapter 2.

CHAPTER 3

Pulse generation in Fano lasers

3.1 Introduction

Ultra-short laser pulses, known for their high peak energy and short duration, enable controlling a system with finer temporal resolution without large energy dissipation, granting them a wide range of applications. Their short duration with high power and wide spectral bandwidth renders them highly suitable for optical communication [61], meeting the demands for large bandwidth and energy efficiency, giving the optical devices an advantage over traditional electrical-based devices [62, 63]. Laser pulses are also essential for artificial intelligence neuromorphic computing, as discussed in Chapter 1 [14].

Techniques like mode-locking can generate pulses in the femtosecond (fs) range [64], with peak powers reaching hundreds of gigawatts, even for only a few millijoules in energy. However, mode-locked lasers, typically built with free-space optics or fiber lasers [65], often require complex, large-footprint setups, even on-chip platforms [66, 67]. Alternative pulse generation techniques like Q-switching [68, 69] and cavity dumping [70, 71], although limited to generating pulses in the nanosecond to picosecond range, offer simpler structures and are more amenable to integration within nanophotonic platforms. Several examples of high-speed on-chip microlaser modulation through gain tuning have already been realized [72–74], and cavity dumping exploiting reflectivity modulation has been demonstrated as modulating the stopband edge of distributed Bragg reflectors (DBRs) [75] or composite mirrors [76, 77].

Despite these advancements, finding a pulse generation device that satisfies small footprints and low energy consumption remains challenging. Fano lasers, characterized by their dispersive mirror properties as described in Chapter 2, present a promising solution by allowing modulation through simple tuning of the NC. The small volume of the NC resolves the difficulties related to footprint and energy consumption, paving the way for efficient, compact lasers capable of pulse generation.

3.2   Mechanisms of pulse generation

3.2.1   Q-switching

Q-switching, as the name suggests, is a technique that manipulates the Q-factor of a laser cavity, resulting in the generation of short, intense pulses of light [78]. Figure 3.1(a) depicts the process of Q-switching pulse generation in a laser cavity. Initially, the cavity experiences high losses that exceed the gain, preventing the establishment of lasing. In this state, the intra-cavity power remains minimal, with only weak spontaneous emission. As the pumping continuously excites carriers, these carriers accumulate and the gain increases. At a certain point, when the cavity loss is suddenly reduced, the photon lifetime inside the cavity increases. This change triggers a cascade of stimulated emissions, rapidly building power within the cavity and emitting a pulse. As the carriers recombine, the gain decreases. The pulse reaches its peak power when the gain equals the cavity loss. After this peak, the emitted power starts to decrease because the gain falls below the level of the cavity loss. Typically, this emission process extends over several round-trip times, producing pulses often on the nanosecond scale.

Q-switching techniques can be classified into two primary categories [79]: active Q-switching and passive Q-switching (Figure 3.1(b)). Active Q-switching utilizes an external modulator such as shutters, spinning mirrors, or attenuators to control cavity loss and therefore can have a flexible repetition rate. Conversely, passive Q-switching employs a saturable absorber within the laser cavity. This absorber induces substantial absorption when it is unsaturated, maintaining the cavity in a high-loss state. However, as the absorber reaches saturation, the loss diminishes, allowing the pulse to be generated. Passive Q-switching usually has a repetition rate inherently tied to the saturable absorber characteristics and pumping power, making it less adjustable than its active counterpart.

3.2.2   Cavity dumping

Cavity dumping is an alternative method for generating laser pulses. Initially, when a cavity maintains a high Q-factor, minimal light is coupled out [81]. An external modulator, similar to those used in active Q-switching, can be utilized to decrease the cavity's Q-factor. This scenario is similar to removing one of the cavity's mirrors, which allows the stored power to be rapidly released in the form of a pulse. Here, energy is stored in the intracavity field, not in carriers. This approach generates pulses within a single round-trip time, producing pulses with shorter duration compared to Q-switching and independent of pumping power. However, it also imposes an additional constraint absent in Q-switching: the mirror switch-off time must not exceed the round-trip time, otherwise, the energy inside the cavity cannot be fully emitted during a single round-trip, resulting in a reduction of the peak power. Assuming the mirror switching time is adequately fast, and the change in mirror reflectance Δr from the steady state r_s to its minimum point r_f can be considered instantaneous, the output
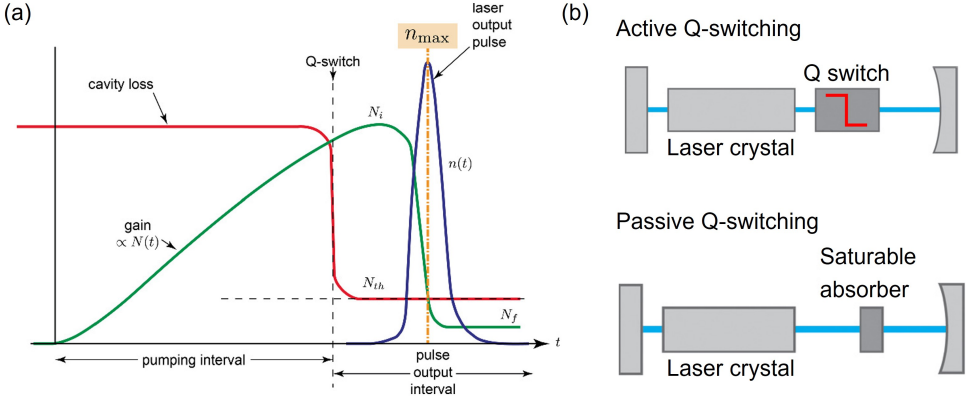
Figure 3.1. (a) Illustration of the Q-switching pulse generation process. The red line is cavity loss, the green line is gain, and the blue line is photon number. The yellow dashed line marks the pulse peak. Reprinted from [79]. (b) Schematics of active and passive Q-switching setups. Reprinted from [80].

peak power will occur when $r = r_f$. The peak power can be estimated by $P_o = |t_f|^2 |S_L^+|^2$, where $|t_f|^2 = 1 - |r_f|^2$ is the final state transmittance. The following can then be derived [38]:

$$
\begin{aligned}
P_o &= \left(1 - |r_s - \Delta r|^2\right) |S_L{}^+|^2 \\
&= \left(1 - |r_s|^2\right) |S_L{}^+|^2 + \left(2r_s\Delta r - \Delta r^2\right) |S_L{}^+|^2 \\
&= P_s + \frac{2r_s\Delta r - |\Delta r|^2}{|t_s|^2} P_s
\end{aligned}
\tag{3.1}
$$

Considering that typically $r_s \to 1$ and $t_s \ll 1$, cavity dumping can achieve significantly higher peak power than pump tuning when using equivalent modulation energy. The peak power for gain tuning (bias modulation) is given by $P_o = P_s + \eta_p(\Delta R/R)P_s$, where η_p is a coefficient smaller than one, and R and ΔR are the pumping rate and its change, respectively [38]. Compared with Equation 3.1, modulating Δr will result in a much larger power variation than modulating ΔR. Figure 3.2 shows simulations of both gain tuning (the terms "Gain switching" and "Bias modulation" in the figure refer to variations of gain tuning differentiated by whether the original state is below or above the threshold, respectively) and cavity dumping. A higher and much narrower pulse generated by cavity dumping is observed [38].
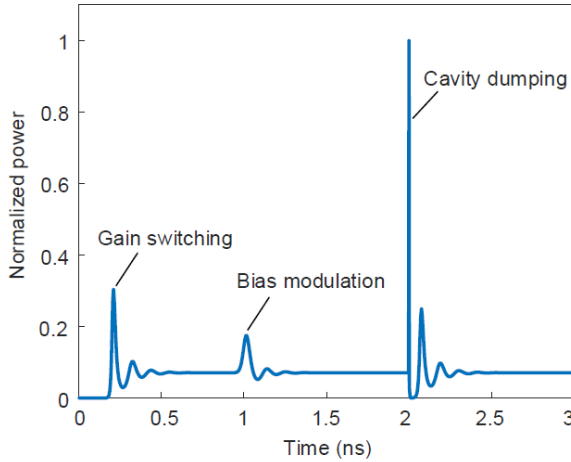
Figure 3.2. Comparison between the pulses generated by gain tuning and cavity dumping. Parameters are set as $r = 0.99$, $\Delta r = 0.1$, $R = \Delta R = 10R_{th}$, and $\eta_p = 1$. Reprinted from [38].

3.3 Modulating a nanocavity

3.3.1 Free carrier effects

When photons are absorbed by a semiconductor, carriers within the semiconductor are generated. An electron can be excited to the conduction band either through direct linear absorption by one photon with energy exceeding the bandgap or through weaker two-photon absorption. In the neutral semiconductor, the creation of an electron in the conduction band is accompanied by the creation of a hole in the valence band. These excited carriers, being no longer bound with lattice atoms, can freely move, thus termed free carriers. The electron density N_e is thus equal to the hole density N_p and can alternatively be expressed as carrier density N. These carriers can alter the refractive index n of the material and, hence, modify the optical characteristics of the semiconductor. Mainly, three effects are induced by the carriers: band filling, bandgap shrinking, and free carrier absorption (FCA) [82].

The band-filling effect, also known as the Burstein-Moss effect [83, 84], occurs when the excited electrons exceed the density of states near the band edge, filling the lowest energy states in the conduction band. As a result, the Fermi level rises, and new excited carriers must absorb photons with greater energy to overcome the enlarged bandgap.

Bandgap shrinking arises from the Coulomb interaction between the carriers. The repulsion could lower (increase) the energy for the electrons (holes) at the edge of the conduction (valence) band, hence reducing the bandgap [85]. Lastly, the free carriers

themselves can also absorb photons and make intra-band transitions [86].

The free carrier effects above can alter the absorption efficiency by either changing the bandgap energy or carrier population. Changes in absorption related to the imaginary part of the refractive index can also modify its real part according to the Kramers–Kronig relations [87]. Reference [82] delineates how these three effects affect the refractive index n in indium phosphide (InP). The change of refractive index $|\Delta n|$ as a function of N is depicted in Figure 3.3, where two different photon energies below the bandgap of InP are considered; in this scenario, the excitation of carriers is primarily due to two-photon absorption (TPA). The value of N used in our simulations and estimates is around 10^{16} to 10^{17} cm^{-3}, in which range Δn is almost linear. We therefore use the relation $\Delta \omega_c / \omega_c = -\Delta n / n$ and approximate the free carrier effect on the NC frequency shift as a linear function:

$$\Delta \omega_c^{car} = K_{car} N_c \qquad (3.2)$$

where N_c is the NC carrier density, and K_{car} is the free carrier coefficient. Note that free carrier effects cause blueshift. The value of $K_{car} = 1.95 \times 10^{-12}$ m^3/s for a hole defect NC implemented in an InP 2D photonic crystal slab is obtained by the pump-probe measurement [48].
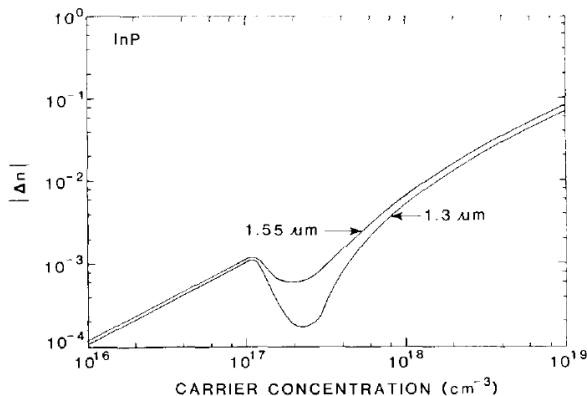
Figure 3.3. Variation in the refractive index of InP with respect to carrier density, evaluated for photon wavelengths of 1.3 and 1.55μm. Reprinted from [82].

3.3.2 Thermal effect

The temperature can also impact the refractive index n due to the thermo-optic effect. Alterations in the lattice constant due to temperature fluctuations can affect optical absorption [88]. Typically, this refractive index shift is often related to the temperature gradient relative to the surrounding environment. Reference [89] establishes the temperature dependence of the refractive index $n_T = dn/dT = 2 \times 10^{-4}$ K^{-1}

for crystalline silicon at a photon wavelength of around 1.5 μm at room temperature. Note that thermal effects generally increase n and induce a redshift contrary to the free carrier effects.

We can express the frequency shift due to thermal effects as follows:

$$\Delta\omega_c^{th} = -K_{th}\Delta T \tag{3.3}$$

Here, $K_{th} = \omega_c n_T/n$, and ΔT denotes the temperature variation of the NC from the original room temperature, which is also the temperature difference between the NC and its surrounding environment (assuming the surrounding environment remains at room temperature). The thermal diffusion equation gives [48]:

$$\frac{d\Delta T(t)}{dt} = -\gamma_{th}\Delta T(t) + \frac{P_{abs}(t)}{C_{InP}} \tag{3.4}$$

where γ_{th} is the thermal relaxation rate, C_{InP} is the thermal capacitance of InP PhC slabs, and P_{abs} is the absorbed power, which subsequently transforms into heat.

Assuming an external optical source is employed to modulate the NC frequency utilizing TPA and following the experimental setup described in Section 3.5 where light is directed from the top side of the NC, we can formulate P_{abs} as:

$$P_{abs}(t) = K_{FCA}(2\epsilon_0 nc)|A_c'(t)|^2 N_c(t) + \eta K_{TPA}(2\epsilon_0 nc)^2|A_c'(t)|^4 \tag{3.5}$$

with

$$K_{FCA} = c\sigma_{FCA}/n \tag{3.6}$$

$$K_{TPA} = c^2\beta_{TPA}/(n^2 V_{TPA}) \tag{3.7}$$

Here, A_c' is the field amplitude of the externally modulated source, whose mode could be different from the lasing mode. The absorption cross-section is denoted by σ_{FCA} [90]. The TPA coefficient is denoted by β_{TPA} [91], and the effective TPA mode volume is denoted by V_{TPA} [92]. The parameter η is the fraction of TPA energy converted to heat. Since the energy sum of the two absorbed photons exceeds the bandgap energy E_g would convert into phonons and induce heat (assuming the Fermi level is near the band edge), we have the relation: $\eta = (2\hbar\omega - E_g)/(2\hbar\omega)$.

For a passive NC, the carrier density dynamics should follow:

$$\frac{dN_c(t)}{dt} = -\frac{N_c(t)}{\tau_{nc}} + \frac{K_{TPA}V_{TPA}}{2\hbar\omega'V_{FCA}^2}(2\epsilon_0 nc)^2|A_c'(t)|^4 \tag{3.8}$$

Here, V_{FCA} is the effective FCA mode volume [92]. The term τ_{nc} is the carrier lifetime inside the NC, which is typically shorter than τ_c, attributed to the much smaller mode volume in the NC, resulting in to denser carrier distribution and faster carrier diffusion [48]. In the following calculation, we set $\tau_{nc} = \tau_c/10$.

The field evolution equation inside the cavity can be obtained by modifying Equation 2.4:

$$\frac{dA_c'(t)}{dt} = -(i\delta(\omega') + \gamma_t')A_c'(t) + \eta_m\sqrt{\gamma_v'}\sqrt{\frac{P_m}{2\varepsilon_0 nc}} \tag{3.9}$$
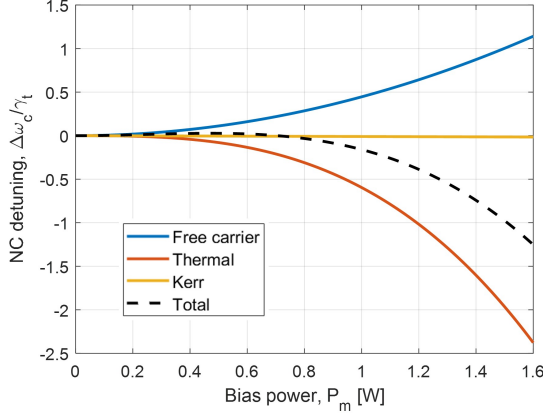
Figure 3.4. Shift in nanocavity frequency as a function of bias power P_m due to free carrier, thermal, Kerr effects, and their cumulative effect at steady state.

where γ'_t and γ'_v represent the total coupling rate and vertical coupling rate for the modulation mode with frequency ω', respectively. The modulation power is denoted by P_m, and the coupling efficiency of the modulation mode is denoted by η_m. At steady-state, for negligible detuning (i.e. $|\delta(\omega')| \ll \gamma'_t$), the following holds:

$$|A'_c|^2 = \eta_m^2 \frac{\gamma'_v}{\gamma'^2_t} \frac{P_m}{2\epsilon_0 nc} \tag{3.10}$$

Figure 3.4 shows the estimation of $\Delta\omega_c$ as a function of P_m when a 1500 nm continuous wave (CW) source at room temperature is used as a bias, injected into the NC at steady state (all the simulation parameters used in this chapter are listed in Table 3.1, unless specified otherwise). Here we assume $\eta_m = 5.6\%$, $\gamma'_t = 2.2 \times 10^{11}$ s^{-1}, and $\gamma'_v = 7.8 \times 10^{10}$ s^{-1} as obtained from experimental fitting [38]. It is observed that the thermal effect shifts the NC frequency on a comparable scale to the free carrier effect when P_m is below 0.7 W. Given that the free carrier and thermal effects counteract each other due to opposite directional shifts in ω_c, approximately 1.3W CW power is needed to achieve a mere $|\Delta\omega_c| = 0.5\gamma_t$ ($\simeq 0.78$ nm). Such power is large and currently challenging to integrate on-chip. To circumvent this issue, enhancing coupling efficiency and rate through in-plane coupling or utilizing an electrical micro-heater for direct NC heating can be considered. If a blueshift is mandatory or shift direction is irrelevant, high-peak-power short pulses can alternatively be employed. At moderate repetition rates, short pulses with low total energy prevent heat accumulation, causing the NC to exhibit only the blueshift from the free carrier effect. Figure 3.5 shows the response of carrier density (green line), temperature (red line), and frequency shift (blue line) of the NC to a modulation pulse with a pulse width of 5 ps and peak power of 150 W. Under these conditions, the highest ΔT remains at a minimal 0.39 K, while $\Delta\omega_c$ can go to 3.8γ_t, primarily attributed to the free carrier effects. Addi-

tionally, it is observable that the decay process of $\Delta\omega_c$ also largely coincides with the N_c decay process.
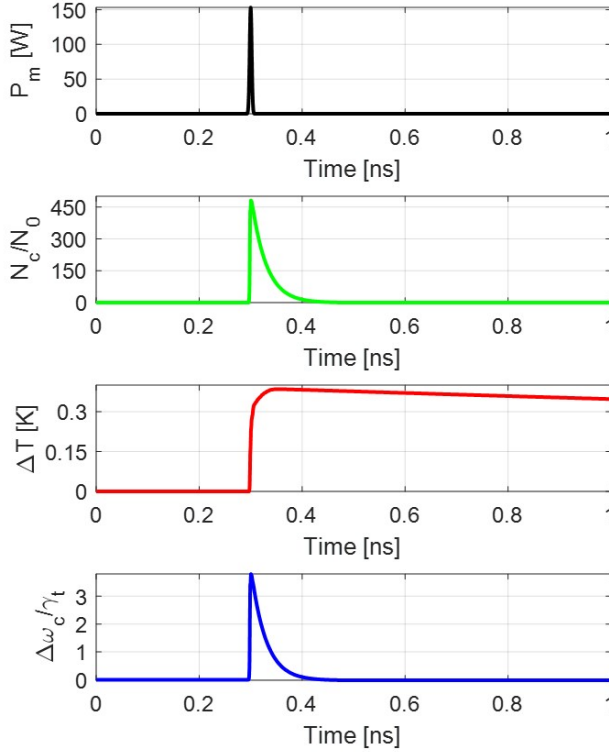
Figure 3.5. Dynamic response of the nanocavity to a modulation pulse. The green line shows the carrier density. The red line shows the temperature. and the blue line shows the frequency shift. The modulation pulse is set to have 1500 nm wavelength, 5 ps pulse width, and 150 W peak power.

3.3.3 Kerr effect

Kerr effect is a nonlinear optical phenomenon that influences the refractive index of a material. This effect arises from the reorientation of molecules, leading to a polarization-dependent shift in the optical phase and, consequently, an effective refractive index alteration [93]. When a light wave propagates through a medium, its electric field can self-induce the Kerr effect, with its strength proportional to the optical intensity. Notably, since the Kerr effect is purely optical and unrelated to

carriers, its response time is virtually instantaneous, especially when compared to the slower free carrier or thermal effects.

The frequency shift in the NC due to the Kerr effect is given by $\Delta\omega_c^{Kerr} = -K_{Kerr}(2\epsilon_0 nc)|A_c'|^2$. where K_{Kerr} is the Kerr coefficient. It can be defined in terms of the NC's properties as [48]:

$$K_{Kerr} = \frac{\omega_c c n_k}{n^2 V_{TPA}} \tag{3.11}$$

where n_k represents the intrinsic Kerr coefficient of the material [48]. Because the Kerr effect occurs much rapidly than both the free carrier and thermal effects, one can measure the change in $\Delta\omega_c$ shortly after modulation begins and estimate the value of K_{Kerr} as demonstrated in [48]. As depicted in Figure 3.4, the impact of the Kerr effect is substantially lesser in magnitude compared to the free carrier and thermal effects. As a result, it will be neglected in the latter modulation simulations.

3.4 Modulation response of Fano lasers

In this section, we explore the response of the Fano mirror to variations in the NC frequency. As a result, the laser exhibits modulation characteristics, enabling the generation of pulses as described earlier. Specifically, our focus will be on the Fano laser's behavior during the transient periods when the NC bias is switched on and off and its eventual steady state. Additionally, we will explore the response to pulse modulation of the NC, a case that aligns more closely with experimental feasibility.

3.4.1 Fano mirror response to tuning the nanocavity

Introducing a bias on the NC produces a shift in the Fano mirror reflectivity $r_F(\omega)$ due to the variations in $\omega_c(t)$ and, in turn, the detuning $\delta(t)$. However, for a laser, the response of $r_F(\omega)$ does not mirror the exact variations of $\omega_c(t)$, given that the laser requires time to establish the dominant resonance mode via relaxation oscillations (RO). Consequently, we turn to our numerical model established in section 2.3, represented by the relationship $r_F(t) = S_L^-(t)/S_L^+(t)$. To evaluate $r_F(t)$, it is necessary to initially find the lasing mode frequency under steady-state OC. Figure 3.6 shows the effective lasing frequency detuning $\Delta\omega_s = \omega_s - \omega_c$ as a function of NC frequency detuning $\Delta\omega_c = \omega_{c0} - \omega_c$, with ω_{c0} denoting the original NC frequency. As seen, $\Delta\omega_s$ exhibits a near-zero negative value for positive $\Delta\omega_c$ and a positive value for negative $\Delta\omega_c$. This highlights that while the Fano laser frequency follows the NC frequency, it consistently remains marginally less shift.

Utilizing the numerical model developed in section 2.3, we can compute the temporal evolution of $r_F(t)$ corresponding to the lasing mode with frequency ω_s. Figure 3.7 shows the response of $|r_F|^2$ to the bias being switched on and off. Assuming the laser is already in the lasing state at the onset (to avoid large-scale turn-on RO), at
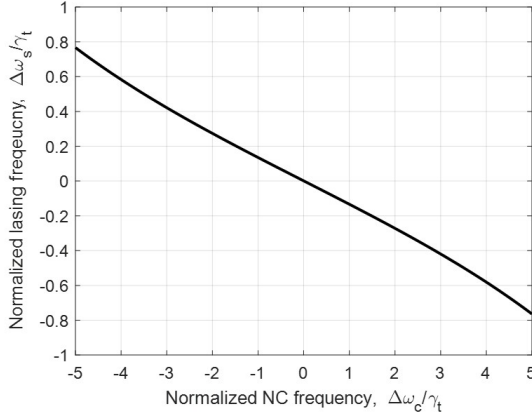
Figure 3.6. Effective lasing frequency detuning for a Fano laser against the nanocavity frequency detuning.

$t = 0.2$ ns, a switch-on (or switch-off) bias is introduced, causing $|r_F|^2$ to decrease (or increase). Following certain ROs, the laser settles into a steady state, with r_F aligning with the analytical steady-state values depicted by the black dashed line. The oscillation frequency and decay rate depend on the final state, with a higher magnitude for the bias switch-on due to the reduced photon number and shortened photon lifetime, as predicted in the semiconductor laser model [52].
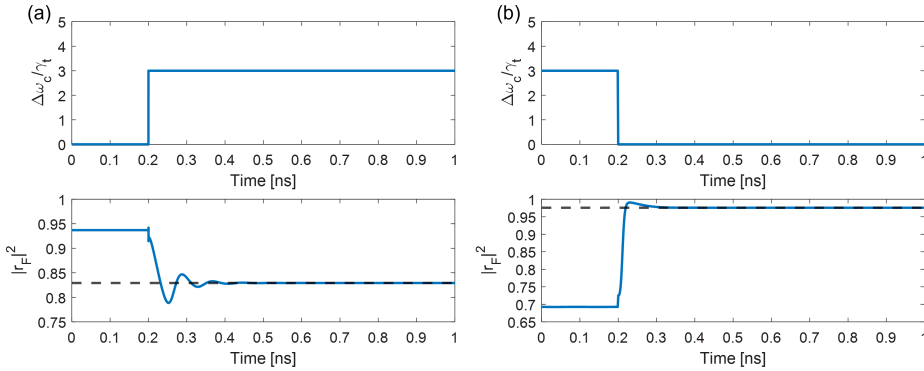
Figure 3.7. (a) Turn-on and (b) turn-off of the bias leading to nanocavity frequency shift and the associated dynamics of the Fano mirror reflectance. The Black dashed line is the analytical steady-state solution calculated from the lasing oscillation condition.

In Figure 3.8(a), the steady-state Fano mirror reflectance and phase against $\Delta\omega_c$ are plotted for the Fano laser and compared with the solitary Fano mirror (employed as a switch). Notably, $|r_F|^2$ is broader in the Fano laser compared to a solitary Fano

mirror since the lasing frequency tends to automatically adjust to match ω_c; this is further verified by the observed linear phase variations. Figure 3.8(b) presents the laser output power from the RHS of the WG P_{out} (proportional to $|S_R^-|^2$) and energy contained within the NC E_{NC} (proportional to $|A_c|^2$). Despite r_F reaching its peak at $\Delta\omega_c = 0$ and having the lowest lasing threshold, the output power also hinges on the mirror's transmission. The balance results in the output's maximum being obtained approximately $3\gamma_t$ away from the reference point (This value depends on the Q-factor of the NC and the Fano mirror bandwidth). However, this limitation can be circumvented by incorporating an additional port coupled to the NC. In such a configuration, the output power would only be weakly influenced by the mirror's reflectivity. Moreover, Figure 3.8(b) shows that E_{NC} has the same profile as the solitary Fano mirror reflectance, suggesting that the higher reflectance of the Fano mirror corresponds to an increased energy stored within the NC. This characteristic leads to the reduction of the laser linewidth, as demonstrated in [37]. We will not delve deeper into this phenomenon as it exceeds the scope of this thesis.
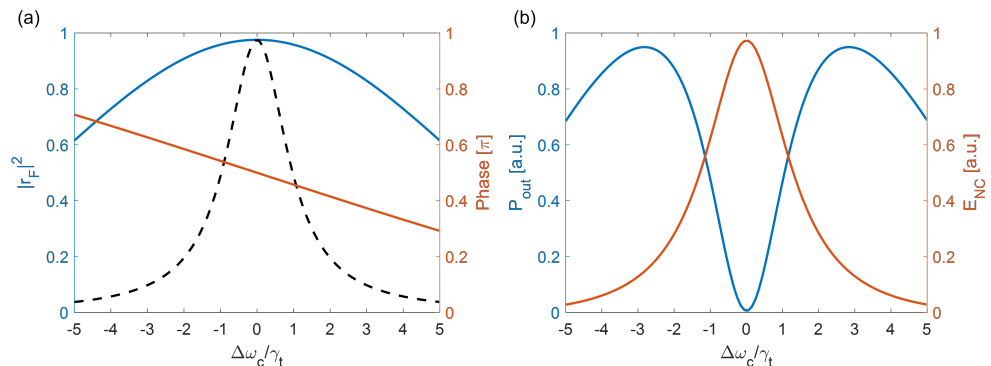
Figure 3.8. (a) Reflectance and phase of the Fano mirror at steady lasing state plotted against the nanocavity frequency detuning. The black dashed line is the reflectance of a solitary Fano mirror. (b) Output power emitted from the right side of the waveguide and the energy contained within the nanocavity plotted against the nanocavity frequency detuning.

3.4.2   Pulse modulation

We then examine the case when the temporal modulation of $\Delta\omega_c$ has the shape of a pulse. In such scenarios, the Fano mirror experiences a rapid change. This leads to phenomena such as cavity dumping and Q-switching.

Referring to Figure 3.5, it is seen that the behavior of $\Delta\omega_c$ resembles the decay dynamics of N_c. To mirror this dynamic in the simulations, we model an external modulation source characterized by a rapid rise in $\Delta\omega_c$, reaching a peak frequency shift (defined as the modulation depth) of $7\gamma_t$, followed by a slow exponential decay

at the rate τ_{nc}^{-1}. This NC frequency shift is illustrated in Figure 3.9(a). As seen in Figure 3.9(b), the output power P_{out} emerges in two pulses: one during the ascent period of $\Delta\omega_c$ and another during its recovery period.
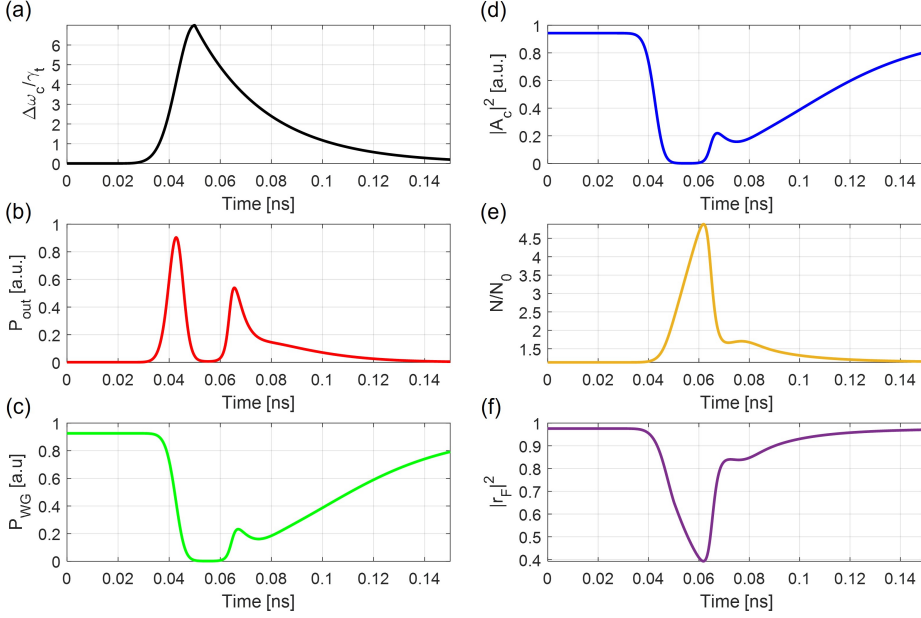
Figure 3.9. Dynamics of the Fano laser's characteristic parameters under pulse-shaped modulation of the nanocavity (NC) frequency. The panels show (a) NC frequency shift, (b) output power, (c) intra-waveguide power, (d) intra-nanocavity energy, (e) carrier density, and (f) Fano mirror reflectance. The ascent period of the NC frequency shift is modeled using a Gaussian function with a pulse width of 10 ps. The decent period uses an exponential decay function with a time constant τ_{nc}. The modulation depth (maximum NC frequency shift) is set to be $7\gamma_t$, and the pumping rate R_p is set to be $100R_{th}$.

During the period of the first peak ($t = 0.043$ ns), the Fano mirror begins to decrease its reflectance, leading to a decline in both the laser cavity (intra-waveguide) power P_{WG} (see Figure 3.9(c)) and the energy within the NC $|A_c|^2$ (see Figure 3.9(d)). However, N starts increasing (see Figure 3.9(e)), suggesting that the initial pulse originates from the combined release of the laser cavity field and NC field but not the field generated from the carrier recombination. This dynamic, similar to "opening the mirror," generates a cavity-dumping pulse, manifesting as a sharp peak. It is noteworthy that at the pulse peak, $|r_F|^2$ only reduces to 0.9, and after the pulse is completely emitted, it only falls to 0.7 (see Figure 3.9(f)). This implies that even a slight modification in the mirror loss can enable a large energy release in the Fano laser. When the NC detuning is non-zero, the energy stored within the NC can be

released as output power. Even with a partially open mirror, the field could still couple out from the laser through the NC. This can be seen from Figure 3.8, where at $|\Delta\omega_c| = 5\gamma_t$, the energy inside the NC E_{NC} decreases nearly to zero, even the Fano mirror reflectance $|r_F|^2$ only drops to 0.6.

The second output pulse ($t = 0.065$ ns) exhibits a distinct mechanism compared to the first one. During this phase, P_{out}, P_{WG}, and $|A_c|^2$ all show an increase while N decreases rapidly. This suggests that this pulse is due to the energy released from the excited carrier, which enhances the overall light field within the laser. In the intervening time between the two pulses, the laser is almost empty of photons, and due to the absence of stimulated emission, the carrier number grows to a high level, and the gain starts to increase. When the gain surpasses the mirror loss, a cascade of stimulated emissions is initiated, leading to the generation of a large number of photons. The origin of this second pulse can be attributed to the Q-switching mechanism as described in the subsection 3.2.1. Following this second pulse, the laser tends to return to its equilibrium state at a decay rate of τ_{nc}^{-1}.

Figure 3.10 displays the two-pulse response as a function of varied laser pumping rates or modulation depths. In Figure 3.10(a), R_P gradually increases from 20 to $100R_{th}$. It is evident that both the cavity dumping and Q-switching pulse amplitudes linearly increase with the pumping rate, maintaining nearly constant pulse widths. This behavior is expected, given that both the intra-cavity power and carrier accumulation rate scale with the pumping power. A decreasing delay time between the two pulses is also attributed to the rapidly increasing gain, which speeds up the stimulated emission that occurs after the cavity-dumping pulse. When the modulation depth is adjusted (denoted as A_m) from 2 to $10\gamma_t$, as shown in Figure 3.10(b), the peak value of the cavity dumping pulse grows with A_m, and the pulse narrows before reaching saturation. Even though a small A_m can already release nearly all photons within the Fano laser, the lower modulation depth can lead to a slow decrease in reflectance rate. The inefficiency of the direct WG out-coupling channel results in wider and less intense pulses. Conversely, the Q-switching pulse's peak becomes both taller and narrower as larger A_m values lead to a more significant mirror loss. Consequently, N can accumulate to high levels before the gain exceeds the loss, leading to more intense pulses with longer inter-pulse intervals.

3.5 Experimental demonstration of pulse generation in Fano lasers

3.5.1 Platform and design of the Fano laser

As introduced in Chapter 2, a Fano laser consists of a WG side-coupled to an NC. We fabricated this structure on an indium phosphide (InP) 2D photonic crystal (PhC) slab. The WG is created by removing a row of holes, introducing a line-defect struc-

(a)

(b)
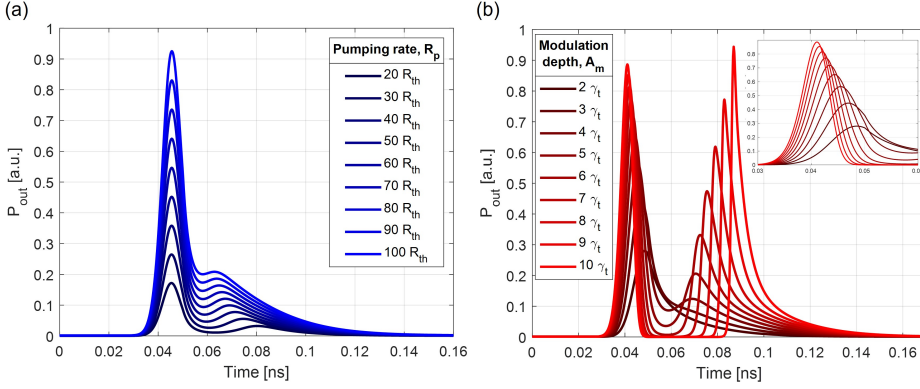
Figure 3.10. Output power response of the Fano laser subject to variations in (a) pumping rate R_p and (b) modulation depth A_m. In (a), A_m is fixed at $4\gamma_t$, and in (b), R_p is fixed at $50R_{th}$. The inset in (b) is the zoom-in view of the cavity dumping pulses.

ture within the PhC. This design allows for a guiding mode whose frequency $\omega < ck_{||}$ (where $k_{||}$ represents the in-plane wavenumber). This mode exists beneath the radiation light cone (modes above this cone have a continuous spectrum and can radiate into the air) and concurrently within the PhC bandgap, as illustrated in Figure 3.11 (a) [5]. Consequently, the light confined within the WG is confined via total internal reflection in the out-of-plane direction, and the photonic bandgap restricts it in the in-plane direction. At the LHS end of WG, the light encounters a broadband mirror (in comparison to the bandwidth of the Fano resonance). At the RHS end of WG, a C-shaped grating coupler (GC) is incorporated both for injecting the laser pumping source and for collecting the output signal.

The NC is a smaller line-defect cavity formed by removing seven holes (termed L7). It has a resonance frequency of approximately 1574 nm for its second-order mode (which is the primary lasing mode we used due to higher output power). For modulation purposes, the third-order mode is selected due to its superior light confinement compared to other modes. A scanning electron microscope (SEM) image of the Fano laser is shown in Figure 3.11 (b). The NC is side-coupled to the WG, positioned approximately 5 μm from the LHS end of WG. This placement fulfills the phase-matching conditions required for lasing. Within the WG, the region extending from the LHS mirror to the RHS Fano mirror has an embedded layer of InGaAsP/InAlGaAs quantum wells inside the InP slab. This layer serves as the active material of the laser and is confined to the area of the laser cavity, excluding the extended portions of the WG and the NC. This design approach, known as the "buried heterostructure" (BH), provides significant benefits by reducing unwanted absorption and carrier diffusion outside the laser cavity [6, 7, 94, 95].
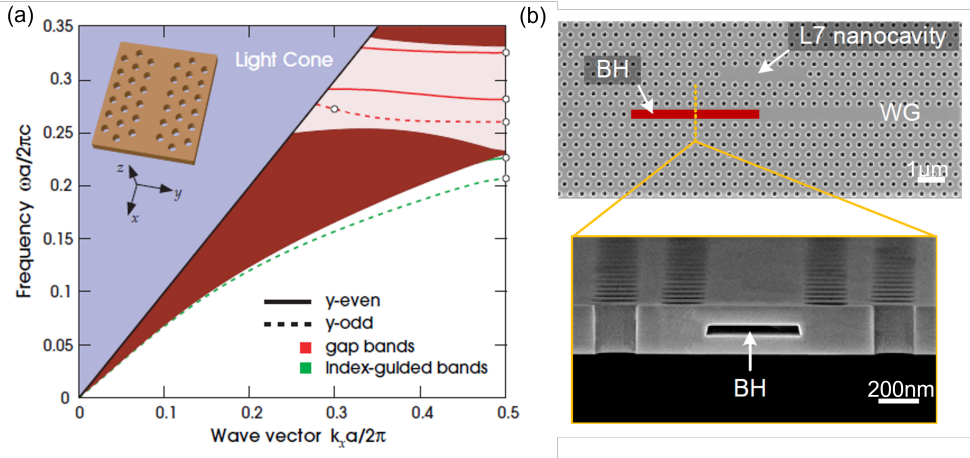
Figure 3.11. (a) An example of the band structure of a 2D photonic crystal slab with a line-defect configuration. The frequency and wavevector are normalized by the lattice constant a. Multiple guided modes are present beneath the light cone and within the bandgap. Reprinted from [5]. (b) Scanning electron microscope image of a fabricated Fano laser (upper panel) constructed on an InP PhC slab. Within the laser cavity, a buried heterostructure gain area (highlighted by the red rectangle) is composed of the structure of a quantum well. Reprinted from [38].

3.5.2 Experimental setup

We first conducted measurements on the static output of the Fano laser. The experimental setup is illustrated in Figure 3.12. A 1480 nm CW laser source is vertically injected into the device through a micro-photoluminescence setup [96]. This source serves as the pump for the Fano laser, entering via the C-shaped GC on the RHS end of WG. Before reaching the device, the pump light first passes through a polarization controller (PC) and a wavelength division multiplexer (WDM) designed for 1480/1550 nm. The PC ensures that the polarization direction aligns with the GC, and the WDM separates the two different wavelength lights into distinct ports, a necessity since both the pump and output signals are coupled from the GC using the same fiber. The output signal is then forwarded to an optical spectrum analyzer (OSA) for analysis. In this configuration, the pumping efficiency is estimated to be around 1%. The pump light, after being focused through an objective lens with a numerical aperture of 0.65, achieves a spot size of approximately 3 μm.

The experimental framework is depicted in Figure 3.13 for the pulse generation measurements. The external modulation source is an ultra-short mode-locked Ti:Sapphire laser. The laser pulses is sent to an optical parametric oscillator (OPO), converting to the desired wavelength for the experiments. The laser pulses out from OPO have a pulse width of 170 fs and a 79.9 MHz repetition rate. These pulses are
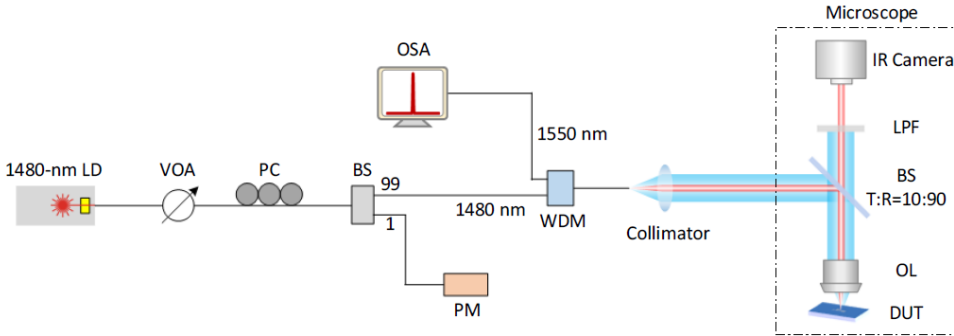
Figure 3.12. Experimental setup of the static Fano laser output measurement. VOA: variable optical attenuator; PC: polarization controller; BS: beam splitter; PM: power meter; WDM: wavelength division multiplexers; OSA: optical spectrum analyzer; OL: objective lens; LPF: long-wavelength pass filter; IR Camera: infrared camera; DUT: device under test. The black lines are single-mode fibers. The blue beam is 1480 nm CW light. The red beam is the output lasing light. Reprinted from [38].

directed through a 10 m single-mode fiber, broadening their width to 4 ps. Such a modification is used to enhance the amplification efficiency for the following erbium-doped fiber amplifiers (EDFAs). To attain sufficient peak power for modulation, we employ a sequence of two EDFAs with optical band-pass filters to sculpt the pulse and align its central frequency with the third-order mode of the NC. The modulated pulse is subsequently combined with the continuous 1480 nm pump light using a 50:50 beam splitter (BS). Two light paths are adjusted to allow a slight spatial offset, enabling selective illumination of either the NC or GC. The output from the Fano laser is then routed through an optical circulator, which guides the signal either to an OSA for spectral analysis or to a communication signal analyzer (CSA) for high-speed waveform measurement. For waveform analysis, further amplification of the signal is necessary to keep an optimal signal-to-noise ratio, which is achieved using a low-power EDFA and filtering again by a band-pass filter.

3.5.3   Experimental results and observations

Figure 3.14(a) illustrates the steady-state output power of the Fano laser under CW pumping. The power measurements, taken post objective lens, are explicitly focused on the second-order mode due to its dominantly higher power over other modes. An evident lasing threshold transition is observed at approximately -5dBm, aligning closely with theoretical predictions (red line). For comparison, we also measured an FP laser with a cavity identical in size to that of the Fano laser's L7 NC, as shown in Figure 3.14(b). Despite the lack of a GC and having to be directly pumped vertically into the cavity, the FP laser exhibited a similar characteristic curve. This FP laser
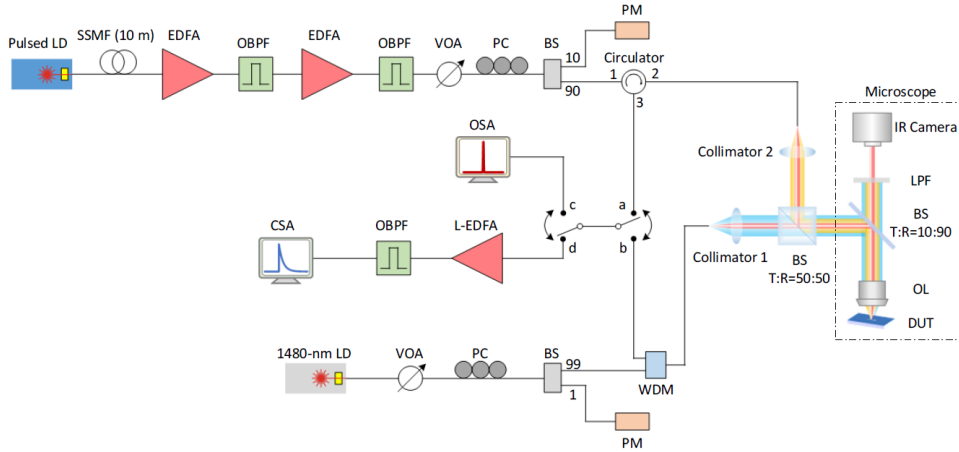
Figure 3.13. Experimental setup of the pulse generation measurement. SSMF: standard single-mode fiber; (L-) EDFA: (low-power) erbium-doped fiber amplifier; OBPF: optical band-pass filter; CSA: communication signal analyzer. The orange beam is the input modulating pulses. Reprinted from [38].

provides us with a comparison reference in the later pulse generation experiment.
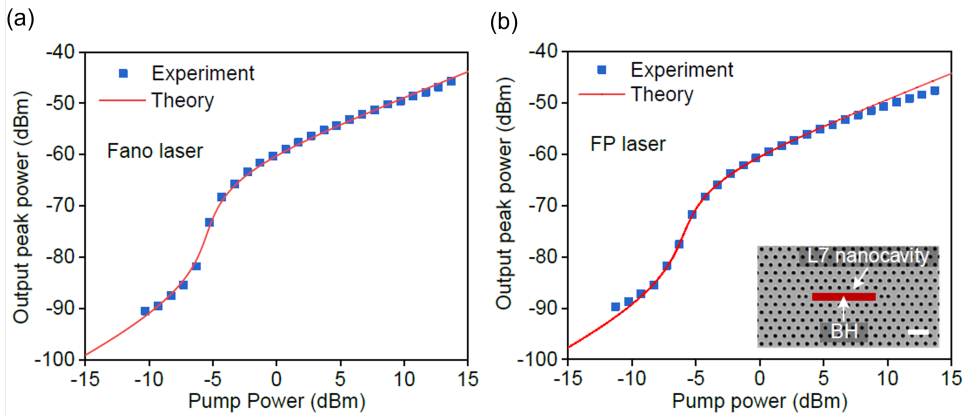
Figure 3.14. Steady-state lasing threshold curve of (a) Fano laser and (b) Fabry-Pérot (FP) laser. The inset in (b) is the SEM image of the L7 FP cavity. Reprinted from [38].

In the pulse generation experiment, the output power of the Fano laser from two different ports is measured. The "through-port (TP)" collected power from the GC, the same as the approach used in the steady-state power measurements. In contrast, the "cross-port (CP)" collected power vertically from the top of NC. Figure 3.15(a) shows an optimized cavity dumping pulse waveform with the pumping power set at

$P = 79P_{th}$ and an average modulated power of 1.26 mW. The TP's output, represented by the red line, shows a cavity dumping pulse approximately 50 ps wide. Following these initial pulses, a "shoulder" emerges in the decay tail, indicating the subsequent Q-switching pulse, as discussed in section 3.4.2. The CP's output, represented by the blue line, exhibits a pronounced dip, which is consistent with the theoretical expectation, as shown in Figure 3.15(b). For comparison, a gray line represents the gain-modulated pulse generated by the FP laser. The cavity dumping pulse is significantly sharper than the gain modulation counterpart in the FP laser. Note that due to the oscilloscope's restricted pulse response (16.5 ps), the cavity dumping pulse from the Fano laser may be somewhat underestimated in this measurement.

Figure 3.15(c) shows the optical spectra of the outputs from both the TP and CP of the Fano laser. The dominant peak for the stable lasing wavelength is located at 1574.6 nm. The noticeable blueshift tail in both ports indicates that the NC frequency shift mainly arises from the free carrier effect, consistent with predictions in Subsection 3.3.1. By tuning the simulation parameters and taking into account the convolution of the oscilloscope's pulse response, we are able to produce waveforms and spectra that closely resemble the measured data. These convoluted results are shown in Figure 3.15(d), while the unconvoluted results are shown in the inset of panel (a). This similarity confirms that our theoretical model can closely mimic the experimental data. In Figure 3.15(e), the temporal dynamics of the Fano mirror's reflection, $|r_F|$ and transmission, $|t_F|$, are calculated. Despite the modulation depth is not particularly large for the estimated reflection of the Fano mirror being $|r_F| = 0.92$ (with a power reflection of $|r_F|^2 = 0.85$), it still enables the release of approximately 40-50% of the intra-cavity energy, as shown in Figure 3.15(b).

The responses of the pulse to variations in pumping power and modulation depth are also investigated. Figures 3.16(a) and (d) show the evolution of the pulse waveform with increasing modulation power (keeping the pumping power fixed at $63P_{th}$), and with increasing pumping power (keeping modulation power fixed at 1.26 mW). In both scenarios, the cavity dumping peak power amplifies far more effectively than the FP laser, as in the subfigures (b) and (e). At higher levels of either P or P_{mod}, the FP laser's output reaches a plateau due to carrier density saturation (subfigure (c)). Note that the Q-switching pulse's "shoulder" becomes noticeable when P_{mod} goes 1.26 mW but is less obvious at lower P_{mod} levels, as seen in the subfigure (a). This observation suggests that at high pumping powers, the output pulses at lower P_{mod} levels are unable to sufficiently delay the secondary Q-switching pulse, causing the two pulses to merge and become indistinguishable, aligning with our simulation in Figure 3.10(a). Conversely, with sufficiently high P_{mod} levels, as in subfigure (d), the secondary pulses become more pronounced. A consistent pattern is observed as P increases: the intensity of the Q-switching pulses grows, and their delay time shortens. In contrast, the cavity dumping pulses remain temporally consistent. Both behavior aligns well with the theoretical calculation in Figure 3.10.
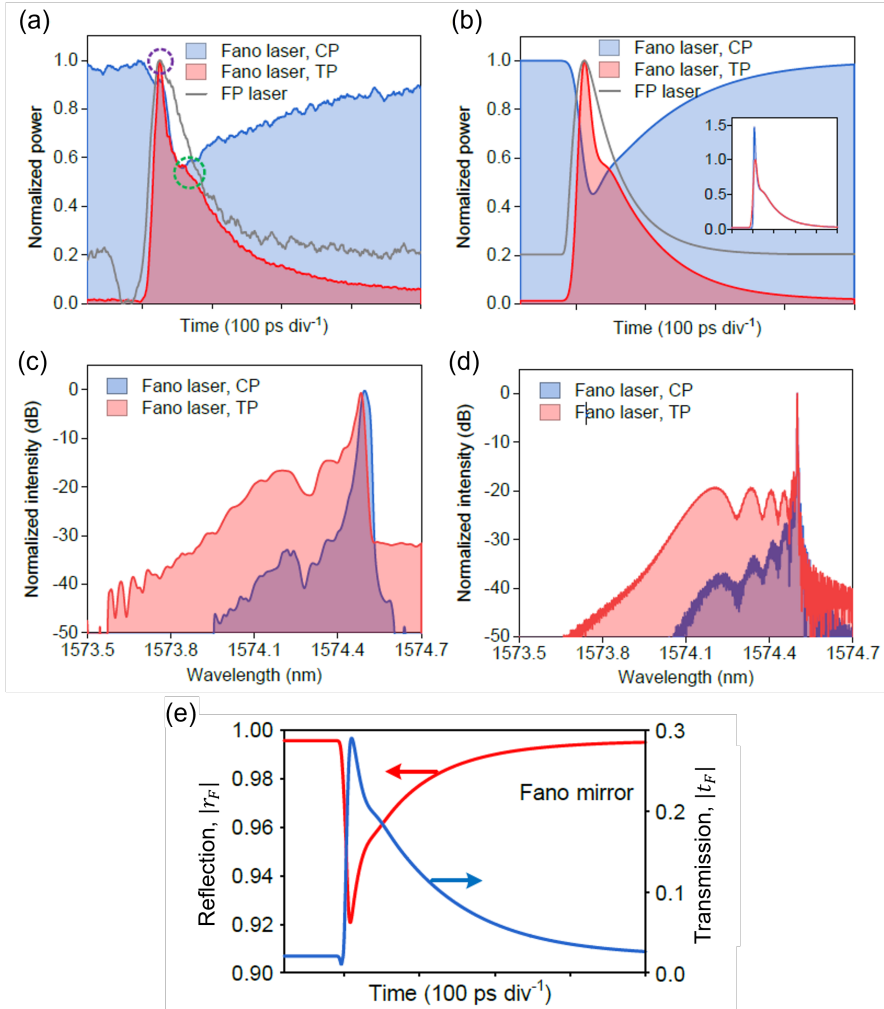
Figure 3.15. Demonstration of the pulse modulation. (a) Experimental measurement and (b) Corresponding simulated fit of the output waveform. CP denotes the cross-port. TP denotes the through-port. The violet circle marks the peak of the cavity dumping pulse, and the green circle marks the "shoulder" originating from the Q-switching pulse. (c) Experimental measurement and (d) Corresponding simulated fit of the optical spectrum. (e) Evolution of Fano mirror reflection $|r_F|$ (red line) and transmission $|t_F|$ (blue line) over time. Reprinted from [38].
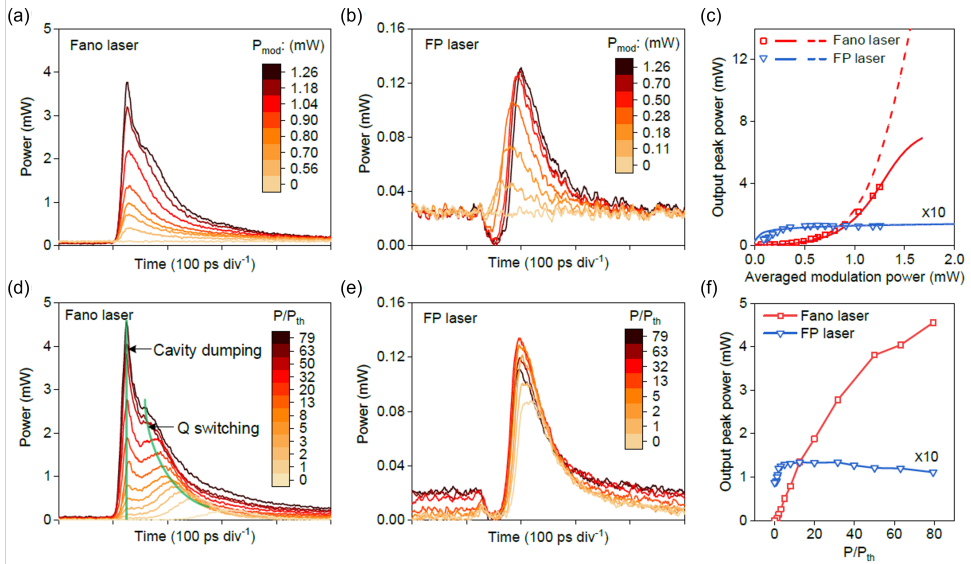
Figure 3.16. Experimental measurement of pulse response concerning pumping power P and modulation depth P_{mod}. Pulses response of the (a) Fano laser and (b) FP laser with varying P_{mod} while P is fixed at $63P_{th}$. (c) Corresponding peak power in (a) and (b). Pulses response of the (d) Fano laser and (e) FP laser with varying P while P_{mod} is fixed at 1.26 mW. Green lines mark the time of the pulse peak. (c) Corresponding peak power in (d) and (e). For clarity, the peak power for the FP laser in (c) and (f) is magnified by a factor of 10.

Parameter	Symbol	Value
Original NC frequency	ω_{c0}	1.215×10^{15} Hz
NC coupling Q	Q_c	500
NC vertical scattering Q	Q_v	10^5
NC internal loss Q	Q_i	86000
WG internal loss	α_i	10 cm^{-1}
LHS mirror reflection coefficient	r_L	-1
Phase and group indices	n, n_g	3.5
Confinement factor	Γ	0.01
Differential gain	g_n	5×10^{-16} m^{-2}
Transparency carrier density	N_0	5×10^{21} m^{-3}
Carrier lifetime	τ_c	0.28 ns
Cross-section of WG mode	A	1.05×10^{-13} m^2
WG length	L	5.37 μm
Threshold pumping rate	R_{th}	3.325×10^{31} m^{-3}s^{-1}
Free carrier dispersion coefficient	K_{car}	1.95×10^{-12} m^{3}s^{-1}
Two-photon absorption coefficient	β_{TPA}	2.4×10^{-10} m/W
Effective two-photon absorption mode volume	V_{TPA}	2.1×10^{-19} m^3
Free carrier absorption cross-section	σ_{FCA}	4.5×10^{-21} m^2
Free carrier absorption mode volume	V_{FCA}	1.3×10^{-19} m^3
InP bandgap energy	E_g	1.344 eV
Intrinsic Kerr coefficient	n_k	1.65×10^{-17} m^2/W

Table 3.1. Simulation parameters used in Chapter 3.

Fano lasers with active feedback

4.1 Introduction

In semiconductor lasers, the characteristics are substantially altered when an external field is injected back into the laser cavity, leading to both beneficial and negative effects. This external field interaction can enable applications such as injection locking [13], but it also risks introducing instability or chaos [13]. The interaction of an external field with a laser modifies the original lasing mode's power and frequency. For lasers with external feedback, it acts as a laser that re-injects its own lasing field after it passes through an external cavity, which is formed by the original out-coupling mirror and an external mirror. As shown in Figure 4.1 [52], for lasers with weak feedback (ignore the external cavity resonance), the mode's frequency shift induced by the external cavity can be approximated as a periodic function, resulting from the altered phase after its round-trip through the external cavity. This leads to multiple steady-state solutions that satisfy the laser rate equations. In semiconductor lasers, the intensity-phase coupling expands the phase shift range, promoting the occurrence of multiple states [52]. This intensity-phase coupling is characterized by the linewidth enhancement factor α, which typically arises from refractive index variations due to carrier density variations [52]. Determining the stability of these solutions usually requires linear stability analysis [52].

Research on Fano lasers with weak optical feedback indicates robustness to coherence collapse far exceeding that of Fabry–Pérot (FP) lasers [34]. In situations with stronger feedback, the field can oscillate multiple times within the external cavity before it decays out. In this case, the feedback field's amplitude and phase shift deviate from simple sinusoidal functions, making analytical analysis more challenging. This chapter explores a Fano laser with a high-reflectance external mirror ($|r_{ext}|^2 > 5\%$), incorporating a gain material embedded in the external cavity that enhances the feedback field strength. The complex interplay between the Fano laser's dispersive mirror and the active external cavity leads to a complicated interplay between the mode frequency and feedback strength. Theoretical calculations show the presence of bistability in these configurations. This exploration could potentially provide new

insights into the behavior of lasers with other types of mirrors, such as DBR lasers, in the presence of strong optical feedback.
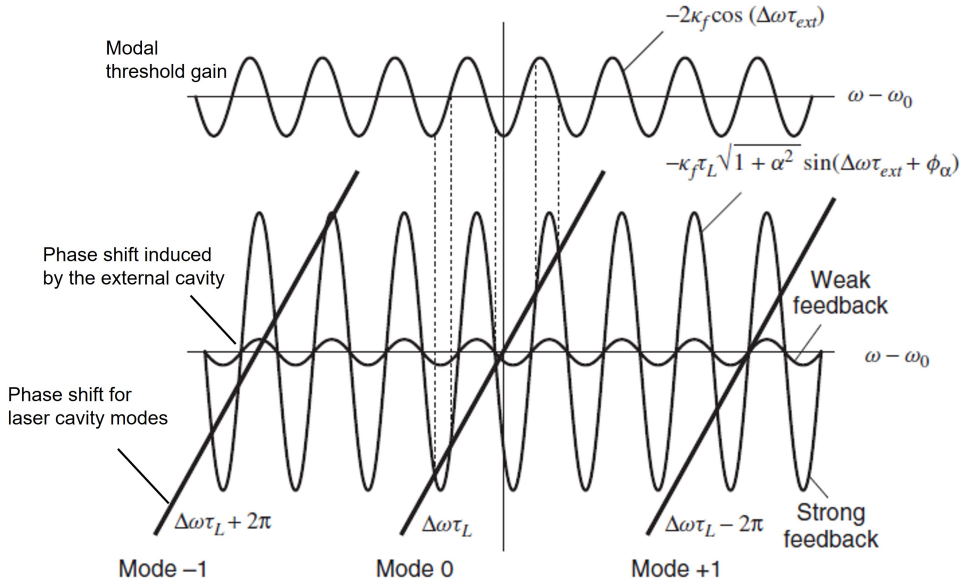
Figure 4.1. Graphical solution for the laser cavity modes with external feedback. The intersections between the straight lines (laser cavity mode phase shifts) and the sinusoidal curves (external cavity induced phase shifts) determine the modes under both weak and strong feedback. Here, κ_f is the feedback rate, τ_L is the laser cavity round-trip time, τ_{ext} is the external cavity round-trip time, $\Delta\omega$ is the total frequency shift, and α is the linewidth enhancement factor. Note that an increase in α promotes the occurrence of multiple solutions. Reprinted from [52].

4.2 Optical bistability

Optical bistability in lasers, where two stable states coexist, is characterized by hysteresis behavior when external parameters such as injection power or feedback strength are varied, as illustrated in Figure 4.2(a). The laser's operational state is typically influenced by initial conditions or the historical trajectory of the system. Within this bistable range, pulse-like external signals can be employed to switch between these two states. This principle underpins digital electronics, particularly in binary data storage, where the "flip-flop" device is a fundamental element for random-access memory and computing systems [97]. Optical counterparts exhibiting this behavior (Figure 4.2(b)) hold potential for applications in switching, routing, memory,

pulse shaping, and logic operations [98]. Previously explored optical bistable devices include semiconductor optical amplifiers (SOA) integrated with Mach-Zehnder Interferometers (MZI) [99,100], coupled ring lasers [101], and photonic crystal microcavity structures [24]. However, these designs often suffer from large footprints and rely on the ability to change the refractive index or gain/absorption within a large specific region of the laser cavities. This approach generally results in high energy consumption for nonlinear effects to achieve sufficient index tuning or long relaxation times, leading to limited operational speed. In contrast, feedback Fano lasers change the laser mirror loss to achieve bistability. We demonstrate that this setup can introduce multiple modes beyond the original Fano mode, enabling bistability between Fano and FP modes. Utilizing the unique properties of the Fano mirror, effective control over laser bistability can be achieved by modulating the NC resonance. This approach might enable rapid flip-flop operations while significantly reducing energy consumption.
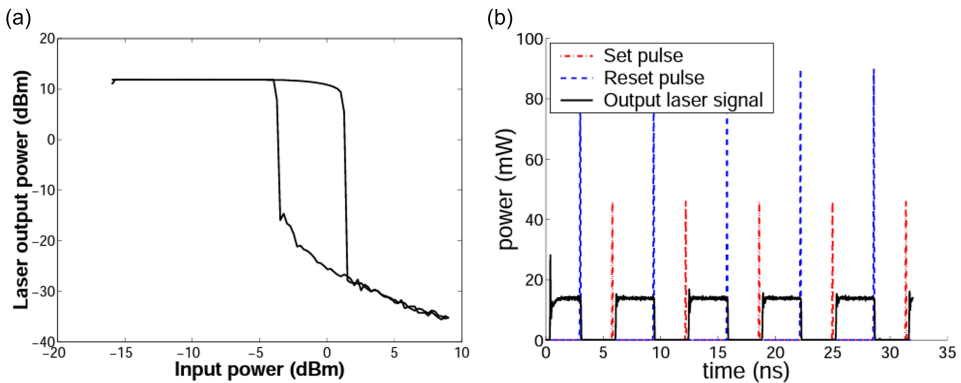
Figure 4.2. (a) Demonstration of hysteresis in a bistable laser during the adjustment of injection power. (b) Operation of an optical flip-flop, utilizing "set" and "reset" pulses to switch between distinct laser states. Reprinted from [98].

4.3 Platform and design feedback Fano lasers

Figure 4.3 (a) illustrates the structure of the feedback Fano laser based on two-dimensional photonic crystal (PhC) membranes. This structure can also be adapted to one-dimensional nanobeams [102–104]. Compared to the ordinary Fano laser discussed in Chapter 2, which has a waveguide (WG) closed at one end and open at the other, the feedback Fano laser presented here has its WG closed on the left-hand-side (LHS) and partially blocked on the right-hand-side (RHS). Such reflectors can be realized via photonic band gap effects as discussed in Subsection 3.5.1. Embedded within the WG is the active medium, comprising either quantum dot or quantum

well structures, implemented using buried heterostructure (BH) nanotechnology (see Subsection 3.5.1). The chosen LHS WG length ensures destructive interference between the field from the side-coupled nanocavity (NC) and the WG-propagating field, making the LHS part of the device identical to a standard zero NC detuning Fano laser [30]. Conversely, the additional reflection mirror on the RHS forms an external feedback cavity. This configuration results in a coupling of FP longitudinal modes and the narrowband Fano resonance mode from the NC. Figure 4.3(b) demonstrates this phenomenon, depicting the internal resonance enhancement factor A_{ir}, which is the ratio of the input field intensity to the field intensity circulating within the cavity. For a FP cavity with mirror reflection coefficients r_1, r_2, and cavity length L, A_{ir} is given by [105]:

$$A_{ir} = \frac{1}{|1 - r_1 r_2 e^{-2ik(\omega)L}|^2} \tag{4.1}$$

In a passive Fano cavity, the reflection coefficient r_2 is replaced by a Fano mirror r_F. For the feedback Fano cavity, r_2 is substituted with a composite mirror r_{CMR} (detailed in Subsection 4.4.2). Both Fano and FP modes can coexist in the feedback Fano cavity, as illustrated in the bottom panel of Figure 4.3(b). Note that the presence of gain material can induce shifts in resonance mode frequencies due to the amplification of the feedback field, affecting their interference with the original field. These modes might become active lasing modes, depending on their threshold gains and the laser's initial state.

4.4   Analysis of modes

4.4.1   Lasing condition of feedback Fano lasers

In contrast to the weak feedback scenario, strong feedback cannot be simply calculated by considering a single external cavity round-trip of the original output signal; resonance with the external cavity should also be considered. The eigenmodes of the laser can be identified using the transmission matrix (T-matrix) approach [52]. The overall T-matrix $\mathbf{T}_{tot}$ for the feedback Fano laser is the product of five individual T-matrices as shown in Figure 4.3(a):

$$\mathbf{T}_{tot} = \mathbf{T}_{LM}\mathbf{T}_{LWG}\mathbf{T}_F\mathbf{T}_{RWG}\mathbf{T}_{RM} \tag{4.2}$$

Here, the subscripts LM and RM denote the LHS and RHS mirrors, LWG and RWG denote the LHS and RHS WGs, and F denotes the Fano mirror. The structure of
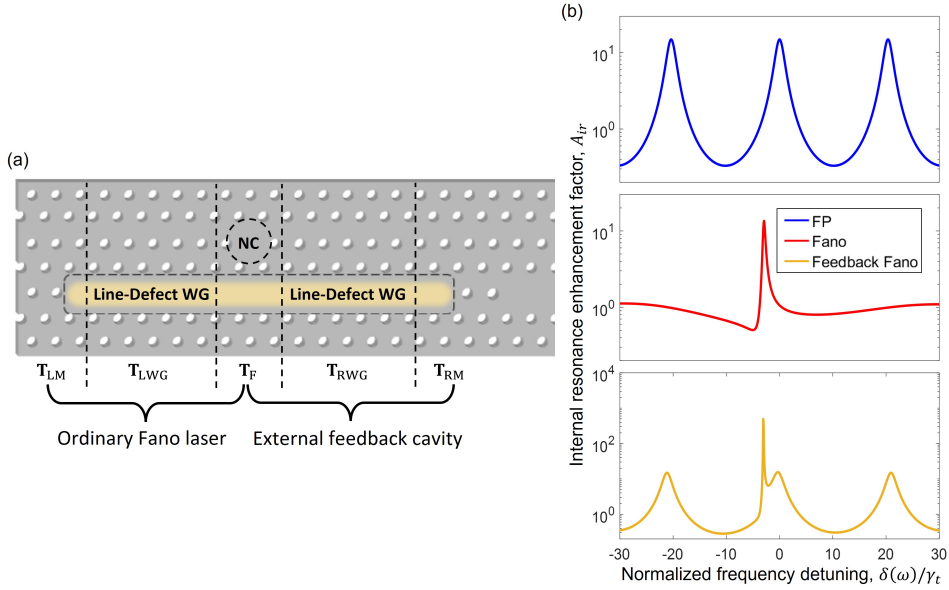
Figure 4.3. (a) Schematic of the feedback Fano laser realized in a 2D photonic crystal slab. A nanocavity (NC) of H1 type (one missing air hole) is side-coupled to a closed line-defect waveguide (WG). The active region is highlighted in light yellow. For transmission matrix analysis, the device is divided into five distinct components. (b) Comparison of the internal resonance enhancement factor A_{ir} across different cavity types: Fabry–Pérot (FP) cavity shown in blue, Fano cavity in red, and feedback Fano cavity in yellow, as a function of normalized frequency detuning. Here, $r_1 = r_2 = -0.9$ and $L = 5.37\mu$m. The Fano mirror reflection coefficient r_F and the composite Fano mirror r_{CMR} are calculated using the parameters listed in Table 4.1.

each T-matrix is as follows:

$$
\begin{aligned}
\mathbf{T}_{LM} &= \frac{1}{t_L} \begin{pmatrix} 1 & -r_L \\ -r_L & 1 \end{pmatrix} \\
\mathbf{T}_{LWG} &= \begin{pmatrix} e^{-ik(\omega,N)L_1} & 0 \\ 0 & e^{ik(\omega,N)L_1} \end{pmatrix} \\
\mathbf{T}_F &= \frac{1}{t_F(\omega)} \begin{pmatrix} 1 & -r_F(\omega) \\ r_F(\omega) & t_F^2(\omega) - r_F^2(\omega) \end{pmatrix} \\
\mathbf{T}_{RWG} &= \begin{pmatrix} e^{-ik(\omega,N)L_2} & 0 \\ 0 & e^{ik(\omega,N)L_2} \end{pmatrix} \\
\mathbf{T}_{RM} &= \frac{1}{t_R} \begin{pmatrix} 1 & r_R \\ r_R & 1 \end{pmatrix}
\end{aligned}
\tag{4.3}
$$

where $r_L (t_L)$ and $r_R (t_R)$ are the reflection (transmission) coefficients of the LHS and RHS mirrors, respectively. L_1 and L_2 are the lengths of the LHS (Fano laser cavity) and RHS (external feedback cavity) of the WG, respectively, and ω denotes the mode frequency. The Fano mirror's reflection and transmission coefficients are defined in Equations 2.9 and 2.10. The wavenumber $k(\omega, N)$ is given by Equation 2.13 with consideration of the linewidth enhancement factor α:

$$k(\omega, N) = \frac{n}{c}\omega - \frac{i}{2}\left((1 - i\alpha)\Gamma g_n(N - N_0) - \alpha_i\right) \tag{4.4}$$

The matrix $\mathbf{T}_{tot}$ can then be transformed into a scattering S-matrix, the poles of which determine the eigenmodes of the laser [52]. These poles correspond to the lasing oscillation conditions. The overall S-matrix shares a common denominator T_{11} between each element, which simplifies the calculation of the pole. Therefore, the oscillation condition of a feedback Fano laser can be reformulated as follows (see Appendix A):

$$
\begin{aligned}
& e^{2ik(\omega, N)L_1} r_L r_F\left(\omega\right) + e^{2ik(\omega, N)L_2} r_R r_F\left(\omega\right) \\
& + e^{2ik(\omega, N)(L_1 + L_2)} r_L r_R\left(t_F^2\left(\omega\right) - r_F^2\left(\omega\right)\right) = 1
\end{aligned}
\tag{4.5}
$$

The first and second terms in Equation 4.5 can be interpreted as the propagation factors when the field in the LHS and RHS WGs encounters the corresponding mirrors and the Fano mirror. The third term describes the coupling between the field traveling in the entire WG and the NC. Using Equation 4.5, we can calculate the oscillation frequency ω and corresponding threshold carrier densities N for all possible lasing modes.

4.4.2 Composite Fano mirror

The concept of a "composite mirror" (CMR) in a feedback Fano laser system is a useful approach for simplifying and understanding the laser's dynamics [52]. By viewing the RHS components of Equation 4.3 ($\mathbf{T}_F$, $\mathbf{T}_{RWG}$ and $\mathbf{T}_{RM}$) as a single entity, the feedback Fano laser can be thought of as a laser having a composite mirror on its RHS. The reflection coefficient for this CMR is given by (see Appendix B):

$$r_{CMR}\left(\omega\right) = r_F\left(\omega\right) + \frac{r_R t_F^2\left(\omega\right) e^{2ik(\omega, N)L_2}}{1 - r_R r_F\left(\omega\right) e^{2ik(\omega, N)L_2}} \tag{4.6}$$

This formulation encapsulates the complex interplay between the different components on the RHS of the laser. Equation 4.6 indicates that r_{CMR} combines the ordinary Fano mirror reflection r_F and an effective reflection stemming from the external cavity. When the feedback is weak, i.e. $|r_R| \ll 1$, the effective reflection term primarily consists of the numerator, depicting a field undergoing a single external cavity round-trip. When the feedback is large, both the numerator and the denominator must be considered. Here, the denominator captures the field's resonance with the

external cavity, which couples N to the imaginary part of r_{CMR} and thus affects the phase. Even without the linewidth enhancement factor, the carrier density can influence the phase of r_{CMR}, and consequently the mode frequency, in a strong feedback cavity with a gain medium. This effect is due to the resonance-induced amplification of the field, which leads to changes in the interference between the original field, coming mainly from the passive side-coupled cavity, and the feedback field.

Figure 4.4 presents the spectra of reflectance and phase for the ordinary Fano mirror, passive composite Fano mirror, and active composite Fano mirror (with $N = 5N_0$) under the conditions $r_R = -0.3$ and $L_1 = L_2$. The peak reflectance remains almost unchanged due to the high reflectance of the ordinary Fano mirror ($|r_F(\delta = 0)|^2 \approx 97.5\%$), but the mirror bandwidth narrowing and the elevation of the floor (far detuned region without Fano resonance) are observed. Additionally, the composite mirror reduces the steep phase shift occurring near zero detuning. Fields redshifting toward the NC frequency acquire larger phase shifts, while those blueshifting toward the NC frequency acquire smaller phase shifts compared to the ordinary Fano mirror.
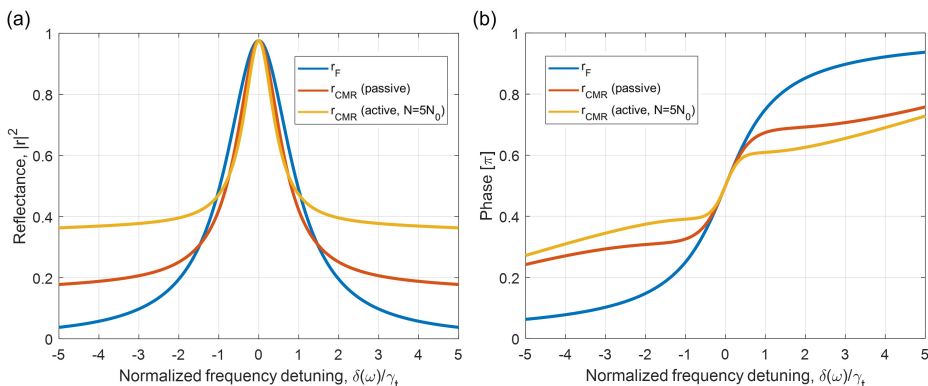
Figure 4.4. (a) Reflectance and (b) phase spectra versus normalized frequency detuning for an ordinary Fano mirror r_F (blue lines), a passive composite Fano mirror r_{CMR} (red lines), and an active composite Fano mirror at $N = 5N_0$ (yellow lines).

4.4.3   Lasing condition and modes in the absence of intensity-phase coupling

By solving Equation 4.5, we can determine all possible modes of a feedback Fano laser, including their mode frequency and threshold carrier density, when tuning the NC frequency through the normalized detuning $\sigma_c = (\omega_c - \omega_{c0})/\gamma_t$. Here, ω_{c0} is the original NC frequency where the ordinary Fano laser achieves its lowest threshold gain, signifying optimal phase matching between the WG round-trip and the Fano mirror. Here, we consider two cases of low ($r_R = -0.3$) and high ($r_R = -0.7$) RHS mirror

reflectivity when $L_1 = L_2$, as shown in Figure 4.5(a),(b) and (c),(d), respectively (all the simulation parameters used in this chapter are listed in Table 4.1, unless specified otherwise). The horizontal dotted lines represent the longitudinal modes of the FP cavity, created by the LHS and RHS mirrors when the NC is transparent. These modes exhibit a free spectral range of $20.5\gamma_t$, as determined by the specific parameters chosen. According to the threshold gains of the lasing modes, each subplot within Figures 4.5 (a)-(d) can be categorized into three distinct regions along the σ_c axis: the Fano mode region (where the lasing mode is the Fano mode, indicated by blue shading), the bistability region (characterized by the potential lasing of either the Fano or the FP mode, indicated by red shading), and the FP mode region (where the lasing mode is the FP mode, non-shaded).

Within the Fano mode region, where the detuning of the NC frequency approximates zero, two distinct Fano modes emerge, their mode frequencies exhibiting an almost linear dependence on σ_c, which means the round-trip phase shifts of these modes are almost entirely determined by the Fano mirror and follow the NC frequency (see Figure 3.6). Here, FP modes are absent due to the Fano mirror's high reflectivity, which effectively divides the WG into two independent cavities. This high reflectivity confines the optical field to either the LHS or RHS WG, leading to two frequency-degenerate Fano modes but with different thresholds. The Fano mode with the higher threshold (and correspondingly lower Q-factor) is the RHS-Fano mode, with its field mainly localized in the NC and the RHS WG. Conversely, the mode with a lower threshold (and a higher Q-factor) is the LHS-Fano mode, with its field primarily concentrated in the NC and the LHS WG. The variation in thresholds stems from the non-equivalence between r_L and r_R. Each mode's Q-factor and the spatial distribution of the mode power are demonstrated in Figure 4.5(e), calculated using the multi-section model which will be introduced in Subsection 4.5.1.

The LHS-Fano mode (green lines in Figure 4.5) can be characterized as an optical field oscillating between the LHS mirror and a composite RHS Fano mirror. This mode's narrower mirror bandwidth causes its threshold to increase more rapidly than that of the ordinary Fano laser (the black dashed line in Figure 4.5(b)) as the absolute NC detuning $|\sigma_c|$ increases. On the contrary, the RHS-Fano mode, where the field oscillates between the RHS mirror and a composite LHS Fano mirror (has the same form as the RHS composite Fano mirror in Equation 4.6, but with L_2 and r_R substituted by L_1 and r_L), exhibits a decreasing threshold with increasing $|\sigma_c|$. This decrease is attributed to enhanced light leakage into the LHS WG due to the reduced reflectance of the central Fano mirror. As a result, the originally lower Q-factor RHS lasing cavity gains additional amplification from the LHS WG, leading to a reduction in its threshold.

Within the FP region, ω_c is far detuned from ω_{c0}, leading to a decreased reflectance of the composite mirror. Under these conditions, the LHS-Fano mode requires a higher threshold gain to counterbalance the increased loss, but the highly reflective composite mirror cannot fulfill the phase-matching condition. Consequently, the FP mode replaces the Fano mode as the dominant lasing mode, maintaining phase matching at the far-detuning background floor of the composite mirror spectrum and
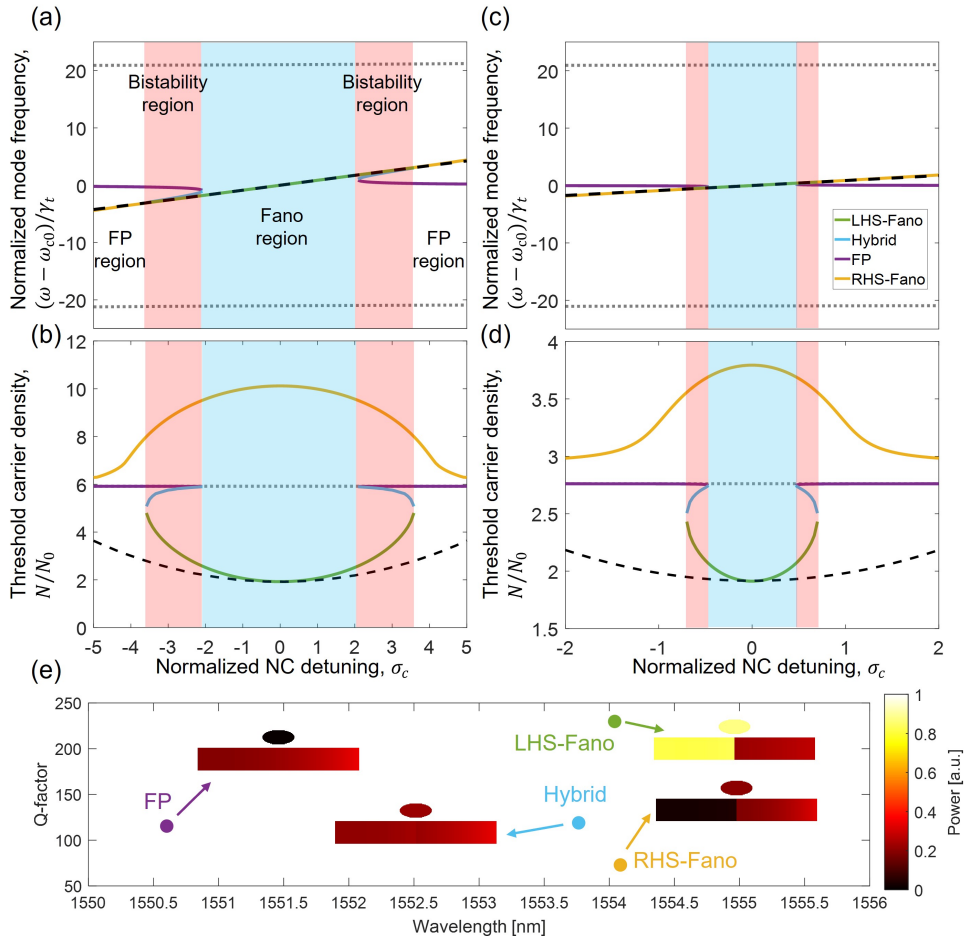
Figure 4.5. (a), (c) Normalized mode frequency $(\omega-\omega_{c0})/\gamma_t$, and (b), (d) the corresponding laser threshold density N/N_0 of the modes as a function of the normalized NC frequency detuning σ_c. (a), (b) correspond to $r_R = -0.3$, and (c), (d) to $r_R = -0.7$, with $\alpha = 0$ in all cases. The colored lines represent four distinct mode types: LHS-Fano (green), hybrid (light blue), FP (violet), and RHS-Fano (orange) modes. The horizontal dotted lines represent the other longitudinal modes of the WG. The black dashed lines represent the Fano mode of the ordinary Fano laser without feedback as a reference. Three different regions are identified: FP (non-shaded), bistability (red-shaded), and Fano (blue-shaded) regions. (e) The resonant wavelengths and Q-factors of each mode in (a) and (b), calculated from the corresponding mirror loss at the NC detuning of $-3\gamma_t$. Insets in (e) graphically represent the spatial power distribution of each mode.

remaining unaffected by variations in σ_c. The dependency of the composite mirror's reflectance with increased NC detuning (from 0 to -4.0γ_t) and the corresponding
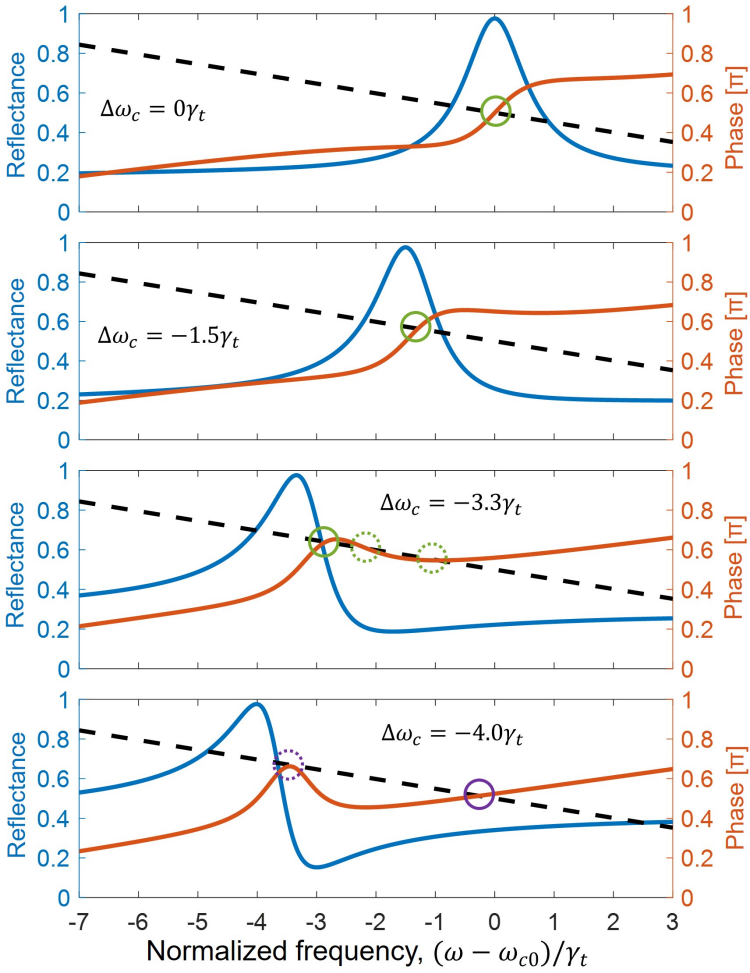
Figure 4.6. Reflection coefficient spectra of the LHS composite Fano mirror r_{CMR} as the NC frequency redshifts from 0 to $-4.0\gamma_t$. The blue lines show the reflectance (right axis), while the red lines show the phase (left axis). The black dashed lines show the propagation phase shift in the LHS WG. In the first three subplots, the solid green circles marking the intersections signify the solutions of the LHS-Fano mode that satisfy both phase matching and loss-gain balance conditions. In the fourth subplot, the solid violet circle marks the FP mode solution. The dashed circles represent the solutions that satisfy phase matching but not the loss-gain balance conditions.

lasing mode is depicted in Figure 4.6.

Besides the Fano and FP domains, two intermediate bistability regions exist where four modes are concurrently displayed. Due to the reduced reflectivity of the compos-

ite mirror, the LHS-Fano mode's threshold increases rapidly with increasing $|\sigma_c|$ and eventually vanishes at some point, determining the boundary between the FP and the bistability region. In these regions, an "intermediate" or hybrid mode bridges the gap between the FP and LHS-Fano modes. This mode's spatial field distribution spans both the WG and the NC (see Figure 4.5(e)). With a larger detuning relative to the NC frequency, this hybrid mode exhibits a higher threshold than the LHS-Fano mode. However, this hybrid mode is unstable (as demonstrated in the stability investigation in Appendix C) and prevents sustained lasing. In contrast, both the FP and LHS-Fano modes are stable, thus characterizing the bistability region. As shown in Figure 4.5, the lasing FP mode extends over both the FP and bistability regions, touching the edges of the Fano region. Conversely, the lasing Fano mode spans the Fano region and overlaps with the FP mode within the bistability region.

4.4.4   Lasing conditions and modes with intensity-phase coupling

As discussed in Section 4.1, intensity-phase coupling is a notable phenomenon in semiconductor lasers, characterized by the linewidth enhancement factor α. Here, we explore the variations in the modes of feedback Fano lasers when α is present. For the case where $\alpha = 0$, as detailed in Subsection 4.4.3, the threshold curves display symmetry around zero NC detuning ($\sigma_c = 0$). This symmetry arises from the Lorentzian shape of the Fano mirror reflectance. However, when α is non-zero (e.g., $\alpha = 2$, a typical value for semiconductor InGaAsP quantum well lasers), an additional phase shift induced by carrier-index coupling (see Equation 4.4) alters the dynamics. This results in a blueshift of the Fano and hybrid modes frequency (illustrated in Figure 4.7(a)-(d)), introducing asymmetry in the curves. The presence of intensity-phase coupling α can lead to multiple solutions even in ordinary Fano lasers, as indicated by the black dashed line in the figure. Among these solutions, the mode with higher frequency tends to be unstable. The interplay between the phase-matching condition, given by $\arg\{r_L\} + \arg\{r_F(\omega)\} + 2L_1 n\omega/c - \alpha\Gamma g_n(N - N_0)/2 = 2m\pi$ (where m is an integer), and the gain-loss balance condition, results in not just the primary solution, the typical Fano modes frequency ($\omega \cong \omega_c$), but also an alternative solution. This alternative solution represents the hybrid mode in the feedback Fano laser framework. As σ_c increases, with an increase in N, the mode frequency ω needs to shift more than in the $\alpha = 0$ case for mode switching to occur. Consequently, a larger α-value broadens the bistability region, as seen in Figure 4.7(a)-(d).

The feedback intensity, characterized by the reflectivity of the RHS mirror r_R, is also important in the functionality of the feedback Fano laser. When $|r_R|$ is increased, for instance, to 0.7, as shown in Figures 4.5(c), (d) and 4.7(c), (d), there is a noticeable shrinking in both the Fano and bistability regions. This shrinking is attributable to the further narrowing of the bandwidth of the composite mirror (similar to the behavior seen in high-gain scenarios, as demonstrated in Figure 4.4).

A detailed analysis presented in Figure 4.7(e) highlights how the bistability range (represented by a black line) and the associated output power contrast vary as a

function of r_R for $\alpha = 2$. Here, the output power contrast is calculated as the ratio between the mode with higher optical output power (LHS-Fano mode for the LHS output and FP mode for the RHS output) and the mode with lower output power (FP mode for the LHS output, and LHS-Fano mode for the RHS output) at the lowest threshold point within the bistability region. In this figure, the power contrast of the LHS mirror output is depicted by a red line, while that of the RHS output is illustrated by a blue line.

Note that mode switching is only feasible when the normalized NC frequency detuning σ_c exceeds the boundaries of the bistability range, as discussed in Subsection 4.5.2. Therefore, as $|r_R|$ increases, the energy required for mode switching decreases. However, Figure 4.7(e) shows that the power contrast diminishes with an increase in $|r_R|$, primarily due to the escalating output power of the FP mode. This reduction in power contrast is a significant concern as it increases the device's vulnerability to noise-induced bit-flip errors [52]. This highlights the need to select an optimal mirror reflectivity to enhance both the reliability and energy efficiency of the flip-flop operation.

4.4.5   Influence of external cavity length

Another critical parameter affecting the bistability is the external cavity length L_2. Variations in L_2, potentially due to fabrication inaccuracies, can impact the round-trip phase in the external cavity, thereby affecting the bistability range. Figure 4.8 shows the dependence of the threshold carrier density and the mode frequency of the lowest threshold mode on σ_c and L_2. In the scenario where the laser operates in the LHS-Fano mode (i.e., $\sigma_c \approx 0$), the field in the RHS WG is relatively weak. Consequently, alterations in L_2 have a minimal impact on the lasing mode, as can be observed in the middle sections of Figures 4.8(a) and (b). Since the Fano laser frequency exhibits a blueshift with the NC frequency blueshift (see Subsection 3.4.1), while it redshifts as L_2 increases (as shown in the phase variation of the composite mirror with L_2 in Figure 4.10(a)), lasing phase matching conditions for the Fano laser can be satisfied in the lower-left and upper-right areas of Figures 4.8(a) and (b). In contrast, in the upper-left and lower-right regions, the phase-matching condition fails to be satisfied, resulting in the laser jumping to the FP mode. The bistability regions, enclosed by red curves in the figures, appear between these two areas. Notably, the size of these bistability regions decreases as the difference $|L_2 - L_1|$ increases (L_1 set to a constant length as in the previous calculations).

The contour plots in Figure 4.8 provide an assessment of the bistability's robustness against variations in L_2. Moreover, it is found that stronger intensity-phase coupling can enhance the robustness of the bistability region against L_2 fluctuations. For instance, when $\alpha = 0$, the tolerance for variations in L_2 that allow the system to remain in the bistability region, for L_1=5.73 μm at $\sigma_c = -3$, is approximately 10 nm, demanding high fabrication precision. However, when α increases to 2, while the bistability region initially on the blue side ($\sigma_c > 0$ when $\alpha = 0$) vanishes, the region
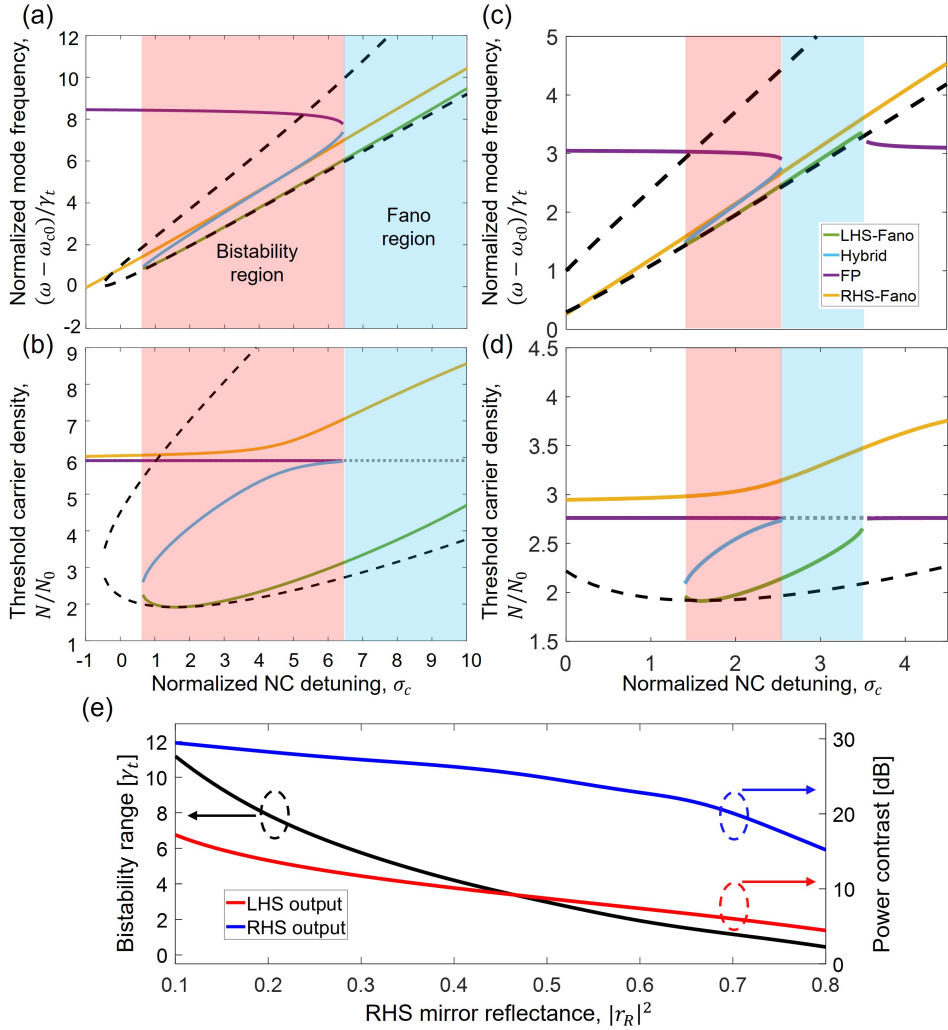
Figure 4.7. (a), (c) Normalized mode frequency $(\omega - \omega_{c0})/\gamma_t$, and (b), (d) the corresponding laser threshold density N/N_0 of the modes as a function of the normalized NC frequency detuning σ_c. (a), (b) correspond to $r_R = 0$, and (c), (d) to $r_R = -0.7$, with $\alpha = 2$ in all cases. The colored lines represent the distinct modes as in Figure 4.5. (e) Bistability range (left axis) and power contrast between the mode with a higher output power and the mode with a lower output power (right axis) as a function of the RHS mirror reflectance $|r_R|^2$. The power contrast is calculated for the NC detuning, where the LHS-Fano mode has the lowest threshold.
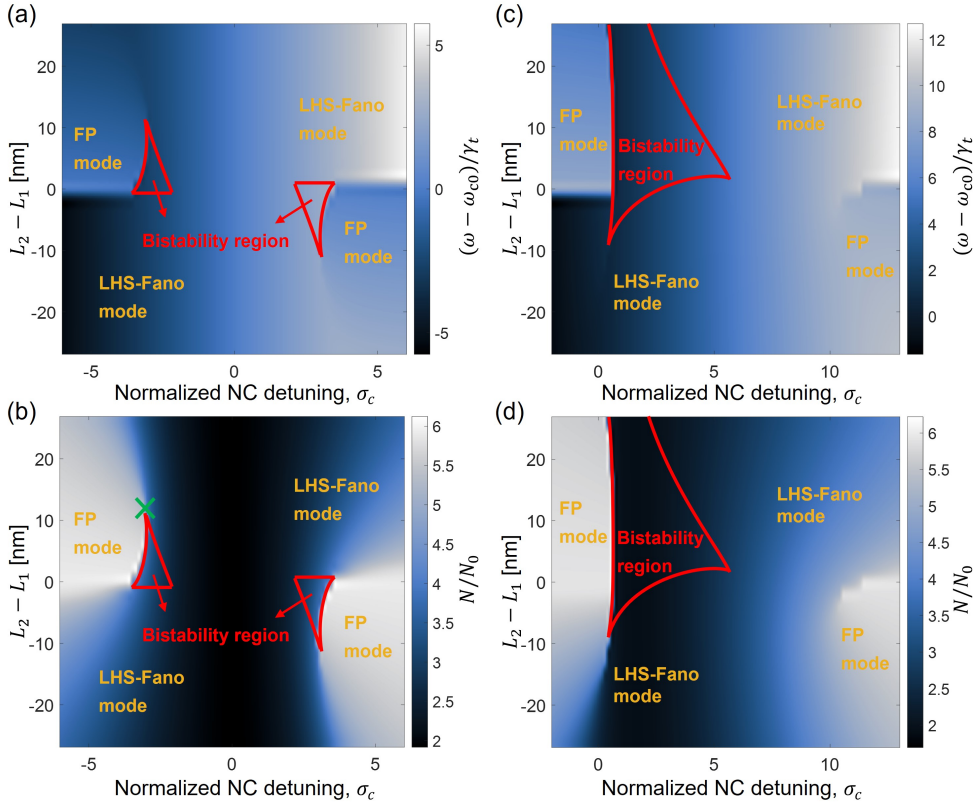
Figure 4.8. The lowest threshold modes as a function of RHS WG length offset, $L_2 - L_1$, and NC detuning σ_c with L_1 fixed at 5.37 μm. (a), (c) show the oscillation frequencies, and (b), (d) show the corresponding threshold carrier density. (a), (b) are under the condition of $\alpha = 0$, and (c), (d) are for $\alpha = 2$. The areas enclosed by the red curves represent the bistability regions. The green cross corresponds to the bottom row panels in Figure 4.9(a) and (b).

initially on the red side ($\sigma_c < 0$ when $\alpha = 0$) blueshifts and expands (as seen in Figure 4.8(c) and (d)). This expansion indicates that the bistability can be preserved even with large deviations in L_2 up to 25 nm.

Figure 4.9(a) shows how the bistability region vanishs when the RHS WG length gradually increases. A unique phenomenon occurs at a specific length of the RHS WG, as plotted by the red curve in Figure 4.9(a) and (b), corresponding to the green cross in Figure 4.8(b). Here, the hybrid mode merges with FP and LHS-Fano modes. This convergence creates, for a certain detuning, an infinite number of points that fulfill the oscillation condition, allowing for a seamless transition between FP and LHS-Fano modes. The primary mechanism behind this phenomenon is the phase
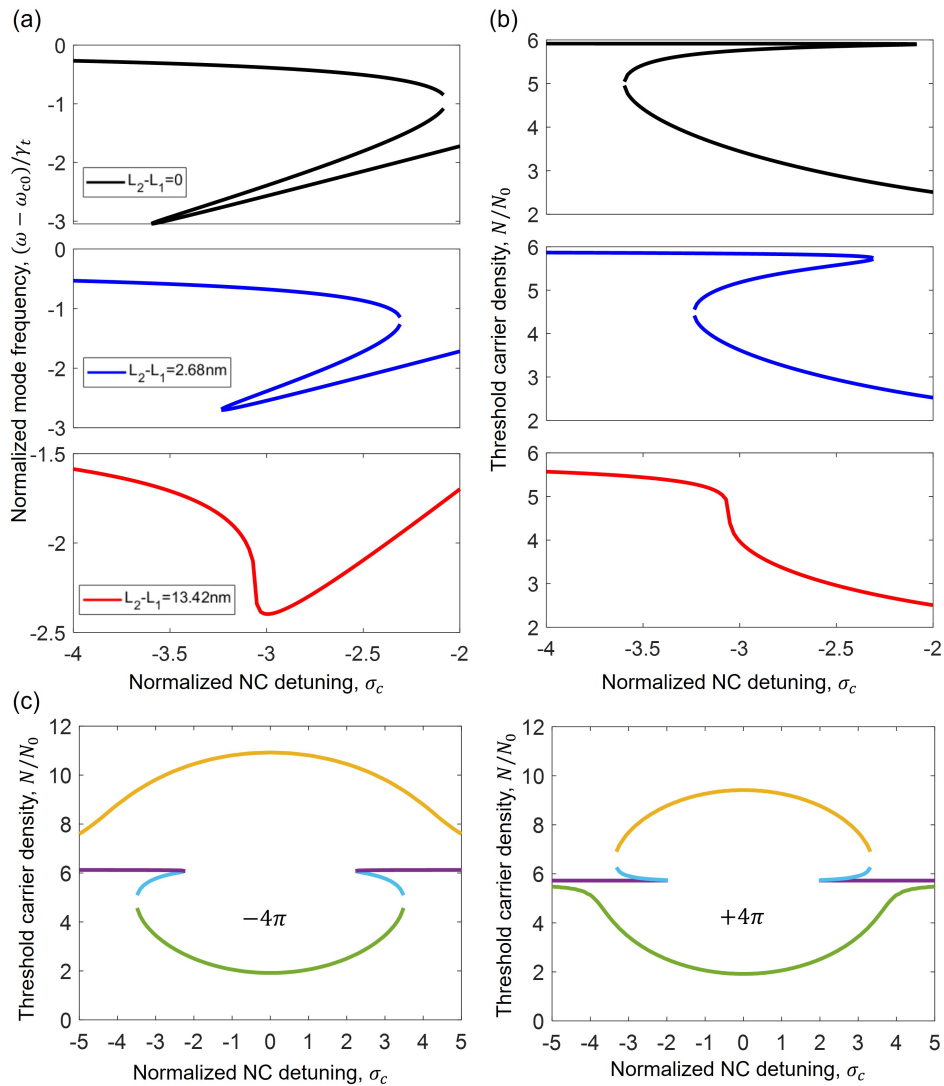
Figure 4.9. Variations in the lowest threshold modes with minor RHS WG length L_2 adjustments, shown for (a) mode frequency and (b) threshold carrier density. The red curves in the bottom row panels represent the critical length at which the bistability region vanishes, corresponding to the green cross in Figure 4.8(b). (c) The threshold carrier density variations of modes when L_2 is shorter (left panel) or longer (right panel) than L_1 corresponds to a WG phase shift of -4π or $+4\pi$.

"flattening" of the composite mirror. Assuming a constant carrier density N, a slight extension of the RHS WG can significantly flatten the composite mirror phase curve on one side of the spectrum, as shown in Figure 4.10(a). Conversely, an increase in N can counterbalance this flattening, as shown in Figure 4.10(b), leading to multiple combinations of ω and N that satisfy the lasing condition. Despite the absence of a mode jump, this transition is accompanied by a large variation in spatial power distribution. This smooth transition could bypass transient relaxation oscillations, with a potential for rapid optical switching, which is particularly beneficial in optical communication systems where fast switching speeds are crucial.

A notable observation is the cyclical re-appearance of bistability, correlating with the RHS WG length, occurring when the phase shift of the field propagating over the extended cavity reaches 2π manifolds, as shown in Figures 4.9(c). This behavior is expected in standard passive structures, as completing a full oscillation cycle (modulo 2π) ensures the propagation phase remains unchanged. However, note that excessively increasing the WG can lead to a decline or even the complete elimination of the bistability region. In the case of an elongated external active WG, the optical field passes a longer distance through the gain medium, resulting in a lower lasing threshold. As previously mentioned, this causes a flatter phase curve of the composite mirror, which in turn can eliminate the bistability.
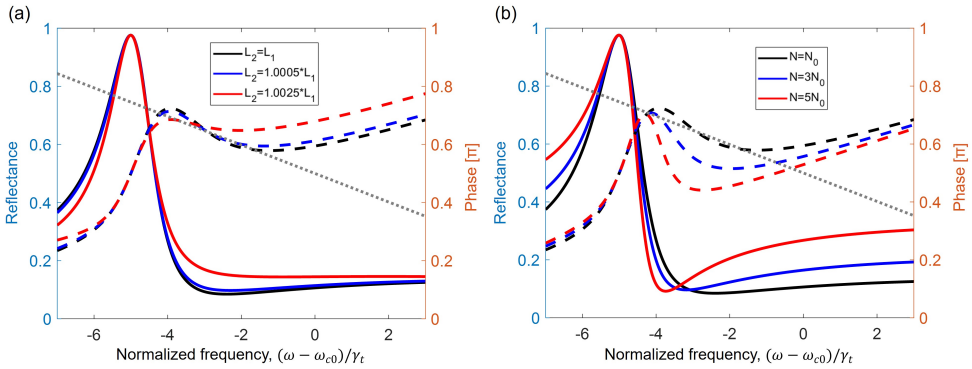
Figure 4.10. Reflection coefficient spectra of the LHS composite Fano mirror r_{CMR} for (a) different external cavity lengths L_2 (where $N = N_0$) and (b) different value of the carrier density N (where $L_2 = L_1$) The NC detuning σ_c is set to -5. The solid lines represent the reflectance (right axis), and the dashed lines represent the phase. The black dotted lines are the propagation phase shift in the LHS WG.

4.5   Numerical simulations of feedback Fano lasers

4.5.1   Multi-section approach for feedback Fano lasers

The T-matrix approach is useful in identifying steady-state cavity modes but falls short of capturing the dynamic lasing behavior. Referencing Subsection 2.3.3, we can expand the multi-section model to accommodate feedback Fano lasers with non-uniform carrier distributions. Here, the WG is divided into $2M$ discrete sections. Each section, indexed as $m = 1, 2...M + 1, M + 2, ...2M + 2$ from the LHS mirror to the RHS mirror, is illustrated in Figure 4.11. We calculate the temporal evolution of fields using a series of plane wave propagation equations:

$$S_m^+ (t + \tau_d) = \begin{cases} r_L S_1^- (t + \tau_d) & (m = 1) \\ S_{m-1}^+ (t) \exp\left(ik\left(\omega, N_{m-1}(t)\right) v_g \tau_d\right) & (2 \leq m \leq M + 1) \end{cases} \tag{4.7}$$

$$S_m^- (t + \tau_d) = S_{m+1}^- (t) \exp\left(ik\left(\omega, N_{m+1}(t)\right) v_g \tau_d\right) \qquad (1 \leq m \leq M) \tag{4.8}$$

$$S_m^+ (t + \tau_d) = \begin{cases} S_{m+1}^+ (t) \exp\left(ik\left(\omega, N_{m+1}(t)\right) v_g \tau_d\right) & (M + 2 \leq m \leq 2M + 1) \\ r_R S_{2M+2}^- (t + \tau_d) & (m = 2M + 2) \end{cases}$$
$$\tag{4.9}$$

$$S_m^- (t + \tau_d) = S_{m-1}^- (t) \exp\left(ik\left(\omega, N_{m-1}(t)\right) v_g \tau_d\right) \qquad (M + 3 \leq m \leq 2M + 2) \tag{4.10}$$

For the central two sections, $m = M + 1$ and $M + 2$, located adjacently on either side of the NC, we denote $S_{M+1}^{\pm}$ and $S_{M+2}^{\pm}$ alternatively as $S_{nl}^{\pm}$ and $S_{nr}^{\pm}$ respectively. The field dynamics at this point is described by the coupled mode equations:

$$S_{nl(nr)}^- (t) = -i S_{nr(nl)}^+ (t) + \sqrt{\gamma_c} A_c (t) \tag{4.11}$$

$$\frac{dA_c (t)}{dt} = -\left(i\delta(\omega) + \gamma_t\right) A_c (t) + i\sqrt{\gamma_c} S_{nl}^+ (t) + i\sqrt{\gamma_c} S_{nr}^+ (t) \tag{4.12}$$

The out-coupling power through the LHS WG (RHS WG) end is $P_{L(R)} = |t_{L(R)}|^2 |S_{1(2M+2)}^-|^2$. Moreover, the carrier rate equation for each section is given by:

$$N_m (t + \tau_d) = (N_m (t) - C_d) \exp\left(-\left(\frac{1}{\tau_c} + C_n + D'\right) \tau_d\right) + C_d \tag{4.13}$$

where C_n and C_d are defined as:

$$C_n = v_g g_n \frac{\sigma_0 \left(|S_m^+ (t)|^2 + |S_m^- (t)|^2\right) d}{V_d} \tag{4.14}$$

$$C_d = \frac{R_p + C_n N_0 + \frac{D}{d^2} \left(N_{m+1}(t) + N_{m-1}(t)\right)}{\frac{1}{\tau_c} + C_n + D'} \tag{4.15}$$

Note that $D' = 2D/d^2$ at $2 \leq m \leq 2M + 1$ and $D' = D/d^2$ at $m = 1, 2M + 2$ at the WG boundary with the section length $d = L_1/M$. All other parameters have the same definitions as in Subsection 2.3.3.
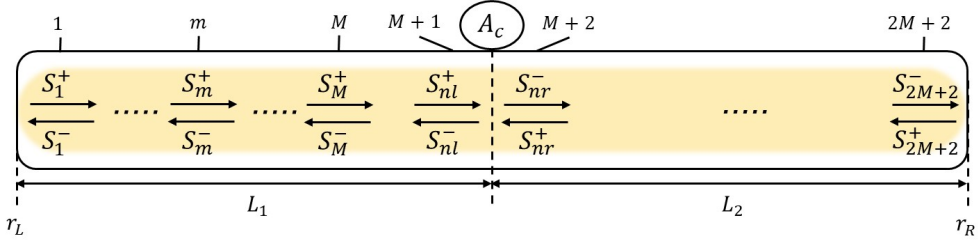
Figure 4.11. Schematic of the multi-section model for a feedback Fano laser. The WG is divided into $2M + 2$ sections. The central two sections, $m = M + 1$, and $M + 2$, are located adjacently on either side of the NC. The light yellow region represents the gain material.

4.5.2 Steady-state solutions

To calculate the steady-state behavior of the laser for varying NC frequency, we gradually vary the parameter σ_c, crossing from negative to positive values and then reversing the process. The steady-state solutions are extracted from the dynamic simulations (using the multi-section approach), when the turn-on relaxation oscillations are damped out. When tuning σ_c, the initial conditions for each dynamic simulation are set to be the steady-state solutions from the prior calculation, incorporating a memory effect of the system's past state into the model. Here, the carrier diffusion rate is assumed to be large, setting the diffusion coefficient D to the limit-value $D_{lim} = d^2/(2\tau_d)$ (see Subsection 2.3.3), section number $M = 20$, RHS mirror reflectivity $r_R = 0.3$, pumping rate $R_p = 20R_{th}$, cavity length $L_1 = L_2$ and linewidth enhancement factor $\alpha = 2$. As shown in Figure 4.12(a), the steady-state solutions derived from the multi-section dynamic model are remarkably matched with the solutions calculated from the lasing oscillation conditions (Figure 4.7(b)). When the NC frequency is blueshifting, the laser retains in the FP mode until $\sigma_c = 6$. A sudden transition to the LHS-Fano mode occurs as the reflectivity of the Fano mirror becomes high enough (the LHS-Fano mode will always dominate over the RHS-Fano mode because of the lower threshold). Conversely, when the NC frequency is redshifting, the laser stays on the LHS-Fano mode until $\sigma_c = 0.5$, and then transits to the FP mode. This transition point differs from that of the blueshift, leading to a hysteresis loop and indicating the bistability.

Further analysis explores the scenario when the diffusion rate is more realistic. With D set to $D_{real} = 6.027 \times 10^{-4}$ m^2/s, carriers are inclined to recombine at or near their initial location. As a result, the carrier density within the RHS WG remains higher than in the LHS WG due to the decreased optical field for the LHS-Fano mode (refer to Figure 4.13(b)). A lowered D leads to more pronounced carrier localization in the RHS WG, thereby enhancing the gain there. This increased gain compensates for the reduction in the Fano mirror loss, causing the reflectance of the composite mirror to have less variation when tuning σ_c. Consequently, lasing in the LHS-Fano mode is maintained over a broader NC detuning range, with reduced variations in
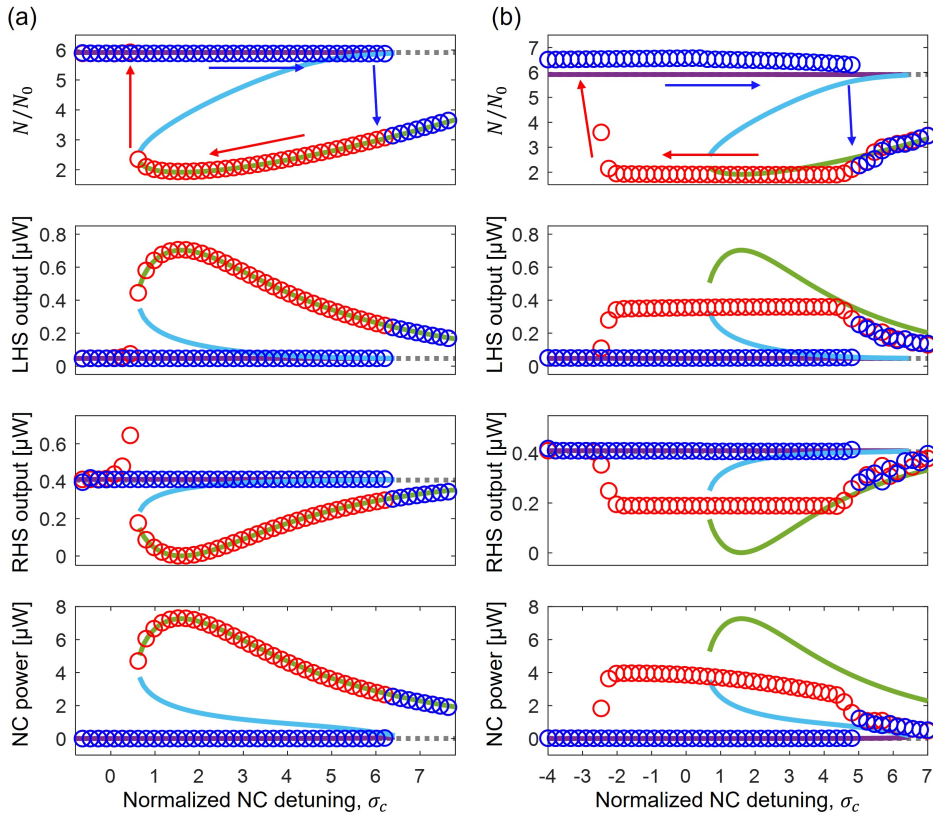
Figure 4.12. Stead-state solutions extracted from dynamic simulations using the multi-section approach for (a) a diffusion coefficient set at the limit-value $D = D_{lim} = d^2/(2\tau_d)$ and (b) a realistic diffusion coefficient $D = D_{real} = 6.027 \times 10^{-4}$ m^2/s. Parameters are fixed at $M = 20$, $r_R = -0.3$, $R_p = 20R_{th}$, $L_1 = L_2$, and $\alpha = 2$. Blue circles are solutions corresponding to a blueshift of the NC frequency (scanning from lower to higher values), while red circles are solutions corresponding to a redshift of the NC frequency (scanning from higher to lower values). The carrier density displayed in the first-row panel of (b) corresponds to the midpoint of the LHS WG.

threshold and power throughout the bistability region, as shown in Figure 4.12(b).
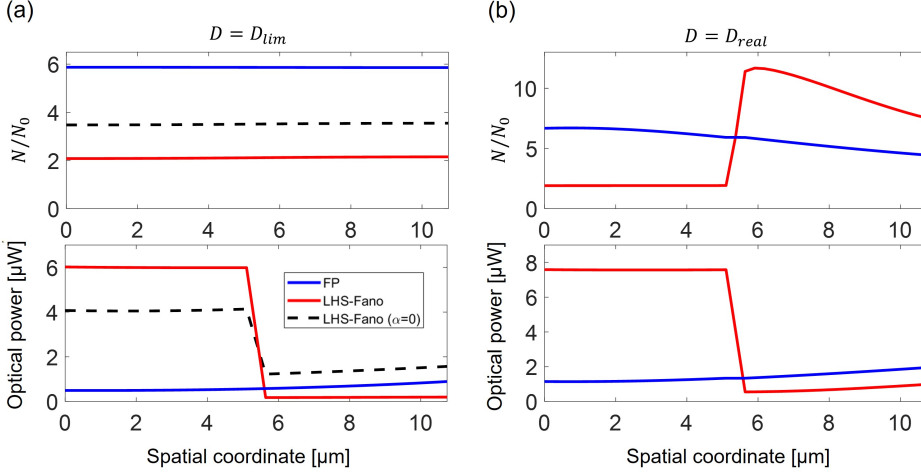
Figure 4.13. The spatial distributions of the carrier density and optical power along the WG for (a) $D = D_{lim}, \sigma_c = 3$ and (b) $D = D_{real}, \sigma_c = 1$. The spatial origin ($0\mu m$) is aligned with the LHS mirror. Blue lines represent the FP mode, and red lines represent the LHS-Fano mode. Black dashed lines represent the LHS-Fano mode as a reference when $\alpha = 0$ and $\sigma_c = 3$.

4.5.3   Dynamics and modulation of feedback Fano lasers

4.5.3.1   Flip-flop operations

Next, we investigate the dynamic response of the laser when σ_c is modulated in time. Such a modulation scheme can be implemented by changing the refractive index of the NC as introduced in Section 3.3, leading to a flip-flop operation between two lasing states, as shown in Figure 4.14(a). Here, the pumping rate R_p is set to $40R_{th}$. The carrier diffusion coefficient D is set to D_{lim} and α is set to be 0. The initial NC detuning σ_c is set at -3, which is in the middle of the bistability region indicated by the red shaded areas in Figures 4.5(a) and (b)). Upon initiation, the laser operates in the LHS-Fano mode, characterized by lower relaxation oscillation frequencies [32] and fast damping rate [32]. A modulation pulse with a Gaussian shape is applied to the NC at $t = 1.2$ ns, causing a redshift of the NC detuning σ_c to -5, making it cross the left boundary of the bistability region ($\sigma_c = -3.6$), as shown in the first-row panel of Figure 4.14(a). The laser then transits from the LHS-Fano mode to the FP mode, characterized by a slower damping rate and faster relaxation oscillation. The laser remains locked in the FP mode even when the detuning reverts to the initial value (e.g., at $t = 1.5$ ns). Subsequently, at $t = 2.4$ ns, another modulation pulse

is applied, causing σ_c to blueshift to -1, which crosses the right boundary of the bistability region ($\sigma_c = -2.1$), driving the laser back to the LHS-Fano mode. This series of control pulses demonstrates the dynamic bistability in the feedback Fano laser system.

The simulation is also performed under realistic conditions with $D = D_{real}$ and $\alpha = 2$, shown in Figure 4.14(b). Here, σ_c is initially set at 1 and tuned from -4 to 6 accordingly. The flip-flop action is still observed. As demonstrated in Figure 4.12(b), when α is non-zero, and D is reduced to a realistic value, the carrier density for the LHS-Fano mode is maintained at a lower level across the entire bistability range (e.g., for $N \cong 2$ ranging from σ_c = -2 to 5). A larger extinction ratio can be attained during the mode-switching compared to the case with zero α and fast diffusion (Figure 4.14(a)). The lower panels of Figures 4.14(a) and (b) show the time evolution of the output power from the LHS mirror (the second row, red lines) and the RHS mirror (the third row, blue lines). The time evolution of the output power from both ends of the WG exhibits opposing trends due to a stronger LHS WG field for the LHS-Fano mode compared to the FP mode. In contrast, the RHS WG exhibits an inverse field strength relation in these two modes (see Figure 4.13). Such an intrinsic anti-correlation between the power levels from the different ports distinguishes the feedback Fano laser from other optical flip-flop devices [24, 99, 101]. This feature makes it possible to construct a shift register by interconnecting the signal from the anti-correlation port to the subsequent flip-flop in a series arrangement [106].

4.5.3.2 Dependence on the characteristics of triggering pulses

As mentioned, the modulating pulse must surpass certain threshold values (bistability region boundaries) to enable mode switching, imposing requirements on both the temporal width and amplitude of the modulating pulse. The laser state will remain unchanged if the modulating pulse peak power is below these threshold values. When the pulse exceeds the threshold, the laser requires a certain duration to alter and stabilize the carrier density level. From the simulations of the switching dynamics (Figure 4.14), one can find the shortest pulse width (full width at half maximum, FWHM) necessary for triggering the mode switching. As seen in Figure 4.15, the minimum FWHM for triggering the Fano-to-FP mode transition (represented by red dots) varies with the pumping power and tends to be longer than that needed for the FP-to-Fano transition (blue dots). This difference is due to the higher threshold of the FP mode, meaning that the carrier population needs time to accumulate to a higher level. Consequently, the minimum FWHM of the triggering pulse for the Fano-to-FP process shows the opposite relation with the pumping power. In contrast, the transition from the FP to Fano mode involves a decrease in average carrier density. This process relies on stimulated emission to reduce the carrier population. which is more rapid than increasing the population. This process resembles the dynamics of a Q-switching as illustrated in Figure 3.1. The laser state transition completes only after the pulse generated by the sudden increase of the cavity's Q-factor has been entirely released. The trailing edge of this pulse is primarily governed by the photon
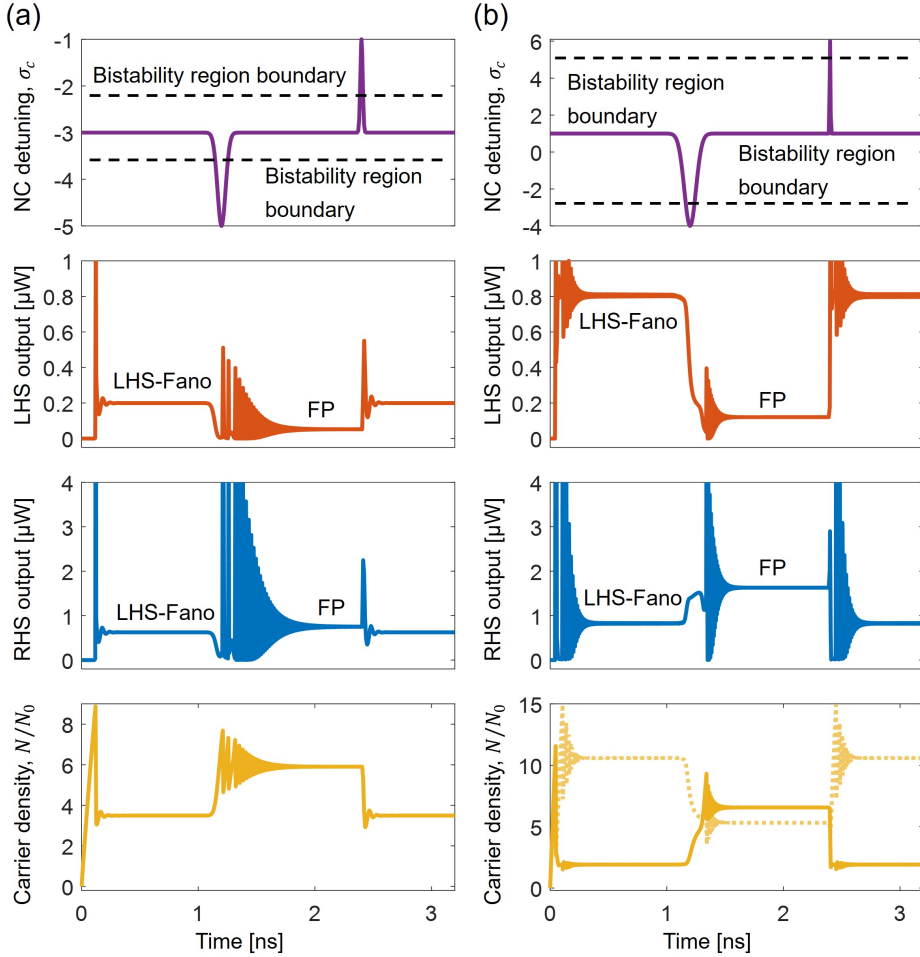
Figure 4.14. Simulation of dynamic flip-flop operation of the feedback Fano laser for (a) $D = D_{lim}$ with $\alpha = 0$, and (b) $D = D_{real}$, $\alpha = 2$. In (a), the NC detuning σ_c starts at -3, redshifts to -5 at $t = 1.2$ ns, then blueshifts to -1 at $t = 2.4$ ns. In (b), the NC detuning σ_c starts at 1, redshifts to -4 at $t = 1.2$ ns, then blueshifts to 6 at $t = 2.4$ ns (first-row panels, violet lines). Black dashed lines mark the corresponding bistability region boundary. Subsequent panels show the LHS output power (second-row panels, red lines) and the RHS output power (third-row panels, blue lines). The bottom row panels show the carrier density at the midpoint of the entire WG for (a) (yellow line), and at both the midpoints of the LHS WG (yellow solid line) and the RHS WG (yellow dashed line) for (b).

lifetime, which depends on mirror loss and cavity length rather than the pumping rate [79]. Consequently, the minimum FWHM for triggering the FP-to-Fano process is much shorter than that for the Fano-to-FP process and shows minimal sensitivity to changes in the pumping rate.
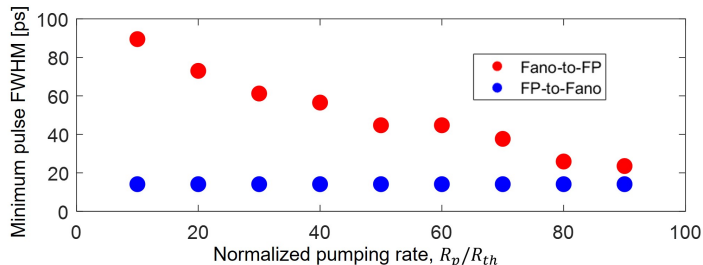
Figure 4.15. Minimum pulse width (FWHM) required to trigger the mode switching as a function of normalized pumping rate R_p/R_{th}, with other parameter settings same as in Figure 4.14(a). Red dots represent the Fano-to-FP mode process, and blue dots represent the FP-to-Fano mode process.

4.5.3.3 Energy consumption estimation of triggering pulses

As indicated, the minimum FWHM of the triggering pulse is expected to depend on the cavity mirror loss and therefore should be affected by the NC detuning σ_c. Figure 4.16(a) depicts the minimum pulse FWHM as a function of σ_c. Here, σ_c is initially set at -3 with the parameters used in Figure 4.14(a) and will be later tuned to the values exceeding the bistability boundaries ($\sigma_c = -3.6$ and -2.1). As seen in Figure 4.16(a), the minimum FWHM of the triggering pulse is inversely related to the modulation amplitude. Once the bistability boundary is surpassed, the minimum pulse FWHM decreases with the increased modulation amplitude for both Fano-to-FP and FP-to-Fano processes. The reduction in pulse width approaches a lower boundary where the Fano mirror is either fully transparent (for the Fano-to-FP process, red curve) or entirely blocked (for the FP-to-Fano process, blue curve). In the former case, the build-up of carriers is not hindered by stimulated emission from the field trapped inside the Fano cavity. In the latter case, the Fano mirror effectively halves the FP cavity's length, decreasing the photon lifetime. Under these conditions, the laser functions either as a 'pure' FP laser or a Fano laser, enabling a mode build-up time shorter than a laser with a semi-transparent mirror. Figure 4.16(a) shows that the lower limits of the triggering pulse width for both processes fall below 50 ps, which is considerably faster than previous photonic crystal optical flip-flop devices [24], requiring several nanoseconds to deplete a significant number of excited carriers.

Next, we estimate Energy requirements for the triggering pulse that shifts the NC frequency are estimated. We assume the NC is illuminated by an external source, which modulates the NC resonant frequency via the refractive index change due to

free carriers generated by two-photon absorption (as discussed in Subsection 3.3.1). Typically, this effect can only result in a resonance blueshift [82] but not the reverse redshift. However, by designing the NC with an initial red detuning σ_i outside the bistability region and then applying a bias to re-enter this region to the detuning value σ_b, one can still realize mode switching for both processes. For instance, the cold cavity detuning is $\sigma_i = -5$, and a constant NC shift of $2\gamma_t$ is applied so that the detuning is biased to $\sigma_b = -3$. Mode switching is achieved by applying a triggering pulse or turning off the bias to cross both sides of the bistability region. The bias power P_b can be estimated through Equation 3.2, yielding $|\sigma_b - \sigma_i| \gamma_t = K_{car} N_c$, and through Equations 3.8 and 3.10 when the time variation of carrier can be set to zero at steady-state, giving $G_{TPA}(P_b/\gamma_{cp})^2 = N_c/\tau_c$, with $G_{TPA} = K_{TPA}V_{TPA}/(2\hbar\omega' V_{FCA}^2)$ representing the two-photon absorption coefficient. The carrier density inside the NC is N_c, and γ_{cp} signifies the total coupling rate for the external modulation mode, leading to a coupling Q-factor of $Q_{cp} = \omega'/(2\gamma_{cp})$, where ω' is the modulation mode frequency. This estimation holds well when the switching speed is much slower than the carrier decay rate, which is a good approximation for an NC with an ultra-small mode volume, which accelerates the carrier diffusion, leading to a lifetime of only a few picoseconds [48, 107, 108]. Furthermore, we assumed that a higher-order mode of the NC, distinct from the Fano mode, is excited to efficiently modulate the NC without affecting the original Fano laser system. The higher-order mode exhibits weak coupling to the WG, allowing the NC to maintain a large Q_{cp} [38]. The bias power is then expressed by:

$$P_b = \sqrt{|\sigma_b - \sigma_i|\, \gamma_t \gamma_{cp}^2/(K_{car}G_{TPA}\tau_c)} \tag{4.16}$$

and the energy cost for the triggering pulse [109]:

$$E_p \approx \sqrt{\Delta T \gamma_t \gamma_{cp}^2/(K_{car}G_{TPA})} \left(\sqrt{|\sigma_c - \sigma_i|} - \sqrt{|\sigma_b - \sigma_i|} \right) \tag{4.17}$$

Here, ΔT is the pulse width. We chose $Q_{cp} = 10^4$ and $V_{FCA} = 0.108~\mu\text{m}^3$, which are reasonable values for an H1-type photonic crystal NC [110].

Figure 4.16(b) shows the energy cost of the triggering pulse for the FP-to-Fano process, starting with an initial NC detuning of $\sigma_i = -5$ and an after-bias detuning of $\sigma_b = -3$. The bias power, as shown in Figure 4.16(c), is in the range of milliwatts and increases monotonically. The bias power for the parameters we used is approximately 0.18 mW for $|\sigma_b - \sigma_i| = 2$.

Figure 4.16(b) shows a trade-off between the switching pulse width and the absolute detuning σ_c caused by the pulse. The most energy-efficient point is the NC detuning shift around $0.5\gamma_t$ ($\sigma_c = -1.5$) from the bistability region's boundary, where the lowest switching energy is observed to be 2.8 fJ/bit. The energy consumption may be further reduced by increasing the Q-factor or reducing the NC's mode volume since a higher Q/V ratio increases the field strength and thereby the optical nonlinearities within the NC [48]. For instance, a tenfold increase in Q_{cp} could reduce the pulse energy to 0.28 fJ/bit, and the bias power to around 16 µW. Although additional
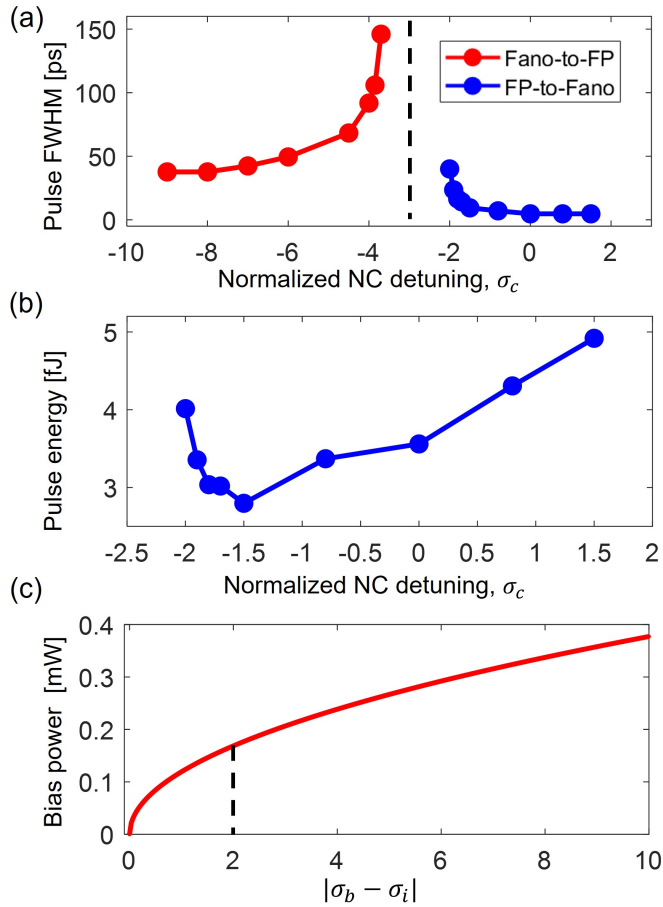
Figure 4.16. (a) Triggering pulse width as a function of normalized NC detuning σ_c, with the same parameters used in Figure 4.14(a). The red line represents the Fano-to-FP process, while the blue line represents the FP-to-Fano process. The black dashed line marks the initial NC detuning before applying the triggering pulse. (b) Corresponding triggering pulse energy for the FP-to-Fano process in (a), with the assumption of employing an H1-type photonic crystal nanocavity where free carrier effects induce the detuning. Here, the initial detuning is set at $\sigma_i = -5$, and then biased to $\sigma_b = -3$. (c) Bias power as a function of $|\sigma_b - \sigma_i|$, with the black dashed line indicating the bias setting used in (b).

power is required for laser pumping, this can be reduced to sub-microwatt levels by employing nanolasers [7].

4.6   Comparison to nanolasers with two coupled cavities

This section compares a two coupled NC system [111], which can also generate fast mode switching with low energy consumption, to the feedback Fano laser, an NC-WG coupled system. In the NC-WG system, the two states – the LHS-Fano and the FP mode – both show stability within the optical bistability region in the numerical dynamic simulations. Here, we analytically analyze the stability of the two coupled NC and the NC-WG coupled systems.

   Consider a system comprising two coupled NCs, each containing active material. For simplicity, we assume that both NCs are identical, characterized by identical resonance frequencies, gain materials, transparency carrier densities, and loss rates. The dynamics of each nanocavity within the coupled system can be described using the temporal coupled-mode theory [54]:

$$\frac{dA_{c1}(t)}{dt} = -(i\delta(\omega) + \gamma_t)A_{c1}(t) + i\gamma_c A_{c2}(t) + \sqrt{g'_{nn}}(N_1 - N_0)A_{c1}(t) \qquad (4.18)$$

$$\frac{dA_{c2}(t)}{dt} = -(i\delta(\omega) + \gamma_t)A_{c2}(t) + i\gamma_c A_{c1}(t) + \sqrt{g'_{nn}}(N_2 - N_0)A_{c2}(t) \qquad (4.19)$$

with the carrier rate equations:

$$\frac{dN_{1(2)}(t)}{dt} = R_p - \frac{N_{1(2)}(t)}{\tau_c} - g'_{nn}|A_{c1(2)}(t)|^2(N_{1(2)}(t) - N_0) \qquad (4.20)$$

Here, A_{c1} and A_{c2} are the amplitudes of the fields inside the first and second NC, respectively. The parameter γ_t is the total decay rate, which is the sum of the coupling rate γ_c between the two cavities and any additional decay rate arising from other loss mechanisms. The parameter g'_{nn} is the gain coefficient for a two coupled NC system, which has a positive value. The time derivative term in Equation 4.20 can be adiabatically eliminated when the pumping rate approaches the laser threshold [52], producing an approximate solution:

$$N_{1(2)} = \frac{\tau_c R_p}{1 + \tau_c g'_{nn}|A_{c1(2)}(t)|^2} + \frac{\tau_c g'_{nn}|A_{c1(2)}(t)|^2}{1 + \tau_c g'_{nn}|A_{c1(2)}(t)|^2}N_0 \qquad (4.21)$$

In the near-threshold region, we can assume $\tau_c g'_{nn}|A_{c1(2)}(t)|^2 << 1$, leading to the approximation $N_{1(2)} = \tau_c R_p - \tau_c^2 R_p g'_{nn}|A_{c1(2)}(t)|^2$. Substituting it into Equation 4.18 and 4.18, we have:

$$\begin{aligned}
\frac{dA_{c1}(t)}{dt} &= -(i\delta(\omega) + \gamma_t)A_{c1}(t) + i\gamma_c A_{c2}(t) \\
&\quad + \sqrt{g'_{nn}}(\tau_c R_p - \tau_c^2 R_p g'_{nn}|A_{c1}(t)|^2 - N_0)A_{c1}(t) \\
&= (-i\delta(\omega) - \gamma_t + \sqrt{g'_{nn}}\tau_c R_p - \sqrt{g'_{nn}}N_0)A_{c1}(t) \\
&\quad - \tau_c^2 R_p g'^{3/2}_{nn}|A_{c1}(t)|^2 A_{c1}(t) + i\gamma_c A_{c2}(t)
\end{aligned} \qquad (4.22)$$

and

$$\frac{dA_{c2}(t)}{dt} = (-i\delta(\omega) - \gamma_t + \sqrt{g'_{nn}}\tau_c R_p - \sqrt{g'_{nn}}N_0)A_{c2}(t)$$
$$- \tau_c{}^2 R_p g'^{3/2}_{nn}|A_{c2}(t)|^2 A_{c2}(t) + i\gamma_c A_{c1}(t) \tag{4.23}$$

Here, we consider the anti-symmetric mode that can exist in two states suitable for bistable operation: one with high A_{c1} and low A_{c2}, and the other with low A_{c1} and high A_{c2}. An anti-symmetric mode function can be defined as $\psi(t)\varphi(r) \equiv A_{c1}(t)\varphi_1(r) - A_{c2}(t)\varphi_2(r)$ with the anti-bonding relation $A_{c1}(t) = -A_{c2}(t)$, the non-overlap relation $\int \varphi_1(r)\varphi_2(r)dr = 0$ and the normalization condition $\int \varphi(r)dr = 1$. Here, $\varphi(r)$ is the space-dependent complex amplitude. As such, we can express $|\psi(t)|^2$ as $2|A_{c1}(t)|^2$ or $2|A_{c2}(t)|^2$ (see Appendix D.1). By subtracting Equations 4.22 and 4.23 and taking an integration over the spatial domain, we have the anti-symmetric mode evolution equation:

$$\frac{d\psi(t)}{dt} = (-i\delta(\omega) - \gamma_t + \sqrt{g'_{nn}}\tau_c R_p - \sqrt{g'_{nn}}N_0)\psi(t) - \frac{\tau_c{}^2 R_p g'^{3/2}_{nn}}{2}|\psi(t)|^2\psi(t) - i\gamma_c\psi(t)$$

$$= -i(\delta(\omega) + \gamma_c)\psi(t) + (\sqrt{g'_{nn}}\tau_c R_p - \gamma_t - \sqrt{g'_{nn}}N_0)\psi(t) - \frac{\tau_c{}^2 R_p g'^{3/2}_{nn}}{2}|\psi(t)|^2\psi(t)$$
$$\tag{4.24}$$

Equation 4.24 is the Stuart-Landau equation [112]. In this equation, the real part of the linear term has a positive coefficient when $\sqrt{g'_{nn}}\tau_c R_p - \sqrt{g'_{nn}}N_0 > \gamma_t$, and a negative coefficient in the cubic term, indicating a supercritical Hopf bifurcation [113]. The laser oscillates between two eigenstates, one characterized by $A_{c1}(t) > A_{c2}(t)$ and the other by $A_{c1}(t) < A_{c2}(t)$. This behavior emerges when the field's out-coupling rate is slower than the field's amplification rate. Consequently, the field that escapes from the first NC is coupled in the second NC and amplified before it is fed back into the first NC. This dynamic leads to a perturbation of the equilibrium, resulting in oscillations between the two asymmetric modes.

For the feedback Fano laser, we assume $L_1 = L_2 = L$ and $r_L = -1$, and simplify Equation 4.12 by substituting 4.7 and 4.11, thereby decoupling the traveling wave amplitude $S^\pm$ from NC field evolution equation, making it solely dependent on $A_c(t)$:

$$\frac{dA_c(t)}{dt} = -(i\delta(\omega) + \gamma_t)A_c(t) + \gamma_c\left[\frac{i(r_L + r_R)e^{2ik(\omega,N)L} + 2r_L r_R e^{4ik(\omega,N)L}}{1 + r_L r_R e^{4ik(\omega,N)L}}\right]A_c(t) \tag{4.25}$$

When the laser operates in the LHS-Fano mode with mode frequency ω_s and carrier density N_s, ω_s close to the NC frequency ω_c, i.e. $\delta(\omega_s) \to 0$, leading to $r_F(\omega_s) \approx i$, and therefore $\exp(2ik_s L) \approx i$ and $\exp(4ik_s L) \approx -1$ with $k_s = k(\omega_s, N_s)$. We can then linearize Equation 4.25, getting a perturbation equation (see Appendix D.2):

$$\frac{d\Delta A_c(t)}{dt} = (\gamma_c - \gamma_t)\Delta A_c(t) + 2GL|A_s|\gamma_c\Delta N(t) \tag{4.26}$$

Here, A_s is the amplitude of the field at steady state, and $G = \frac{1}{2}\Gamma g_n$ is the imaginary part coefficient of the wavenumber. Applying a similar approach to the carrier rate equation with the condition $N_s \approx N_0$, we derive (see Appendix D.2):

$$\frac{d\Delta N(t)}{dt} = -\frac{\Delta N(t)}{\tau_c} - g'_{nl}\gamma_c|A_s|^2\Delta N(t) \tag{4.27}$$

where g'_{nl} is the gain coefficient associated with S^-_{nl}, which has a positive value. We then have the differential equation for the perturbed amplitudes $\Delta A_c(t)$ and carrier density $\Delta N(t)$:

$$\frac{d}{dt}\begin{pmatrix} \Delta A_c(t) \\ \Delta N(t) \end{pmatrix} = J_{LF}\begin{pmatrix} \Delta A_c(t) \\ \Delta N(t) \end{pmatrix} \tag{4.28}$$

with the Jacobian matrix:

$$J_{LF} = \begin{pmatrix} \gamma_c - \gamma_t & 2GL|A_s|\gamma_c \\ 0 & -(1/\tau_c + g'_{nl}\gamma_c|A_s|^2) \end{pmatrix} \tag{4.29}$$

From this matrix, we can straightforwardly get the eigenvalues $\lambda_1 = \gamma_c - \gamma_t$ and $\lambda_2 = -(1/\tau_c + g'_{nl}\gamma_c|A_s|^2)$. Notably, both eigenvalues are negative (γ_t is a bit larger than γ_c), indicating the stability of the LHS-Fano mode.

Alternatively, if the laser operates in the FP mode, we get the corresponding small-signal dynamical equation for the FP mode :

$$\frac{d}{dt}\begin{pmatrix} \Delta A_c(t) \\ \Delta N(t) \end{pmatrix} = J_{FP}\begin{pmatrix} \Delta A_c(t) \\ \Delta N(t) \end{pmatrix} \tag{4.30}$$

The corresponding Jacobian matrix is (see Appendix D.2):

$$J_{FP} = \begin{pmatrix} -(\zeta_1 - 1)\gamma_t & -2|A_s|GL(\zeta_1 - 1)\frac{\delta^2(\omega_s)}{\gamma_t} \\ -2\kappa\gamma_c|A_s|(N_s - N_0) & -(\frac{1}{\tau_c} + \kappa\gamma_c|A_s|^2) \end{pmatrix} \tag{4.31}$$

where $\zeta_1 = (1 + |r_R|)/(2\sqrt{|r_R|})$, and the coefficient κ is:

$$\kappa = g_{nl}{}'\left(\frac{1}{2}\frac{\delta^2(\omega_s)}{\gamma_t{}^2}\sqrt{|r_R|}(\zeta_1 - 1) + |r_R|\right) + g_{nr}{}'\left(\frac{1}{2}\frac{\delta^2(\omega_s)}{\gamma_t{}^2}\frac{1}{\sqrt{|r_R|}}(\zeta_1 - 1) + \frac{1}{|r_R|}\right) \tag{4.32}$$

Since $\zeta_1 \geq 1$, the trace of J_{FP} is negative. Additionally, because the NC energy is very small for the FP mode, the term associated with $|A_s|^2$ can be neglected, resulting in a positive determinant of J_{FP}, which implies that the FP mode is stable. This stability analysis of the FP mode in the feedback Fano laser system indicates that these lasers can avoid oscillation as in lasers with two coupled cavities.

4.7   Experimental results and observations

Experiments were conducted on a feedback Fano laser, although the evidence of bistability had not yet been obtained. However, some observations can be explained with the feedback Fano laser model.

We investigated a feedback Fano laser sample comprising a line-defect WG side-coupled to an L7 NC, based on a two-dimensional indium phosphide (InP) photonic crystal (PhC) slab with an embedded layer of InGaAsP/InAlGaAs quantum well as the gain medium, as shown in Figure 4.17. This sample is similar to the configuration described in Subsection 3.5.1. The distinction is the gain medium extends along the entire WG until the grating coupler (GC). The grating coupler here not only acts as the port for signal collection and pump light injection but also functions as an external reflector, transforming the device into a Fano laser with feedback. The L7 NC is designed to have a resonance frequency near 1550 nm for its fundamental mode. A series of samples were fabricated with adjusted PhC's hole radii to span guiding mode frequencies from 1530 to 1570 nm, aiming for optimal phase matching between the WG and NC.

The cavity length of the Fano laser, corresponding to the LHS WG length in the feedback Fano model, measures approximately 5.37 μm. The distance from the NC to the GC, corresponding to the RHS WG, is about 20 μm. We began by characterizing the lasing spectrum of the device, using a 1480 nm continuous wave laser for pumping, directed at the grating coupler via a micro-photoluminescence setup [96], as illustrated in Figure 3.12. The C-shaped grating coupler, designed for 1480 nm, exhibits approximately 40% reflectance at 1550 nm, as determined by finite-difference time-domain (FDTD) simulations. Since the pump wavelength is significantly detuned from the resonance frequency of the NC, the Fano mirror will not impede the pump, ensuring uniform carrier pumping across the WG.
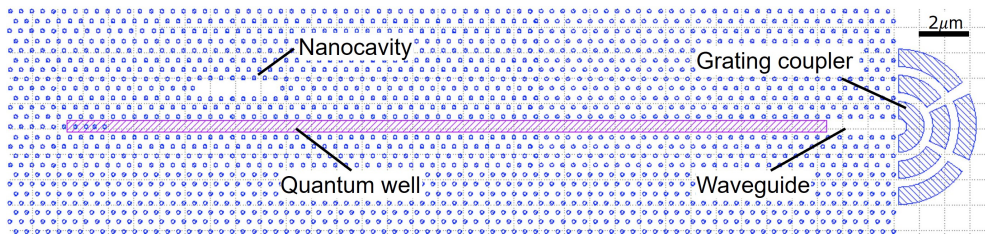

Figure 4.17. Schematic of the feedback Fano laser sample. The blue circles are the air holes, forming the photonic crystal structure. The violet rectangle marks the region of the quantum well structure.

4.7.1   Emission spectra and laser L-L curves

Figure 4.18(a) shows the emission spectrum for a sample illuminated with a 1480 nm pump. The optical spectrum analyzer (OSA) used has a resolution limit of 0.02 nm. We observe multiple emission peaks between 1538 and 1542 nm. The peak at 1540.44 nm is identified as the Fano mode as it is the only mode detected when out-coupling signals are collected from directly above the NC. The other peaks are probably higher-order FP modes originating from the photonic crystal structure [5]; they could also be defect modes or Anderson localized modes [114]. This sample shows a very close wavelength difference between the Fano mode and the FP mode nearest to it (within 0.5 nm), providing an opportunity to observe bistability. Here, we focus on the Fano mode and the adjacent FP mode (termed as the 1st FP mode), positioned immediately next to the Fano mode at a peak wavelength of 1540.75 nm. The corresponding light-in versus light-out (L-L) curve for both the Fano and the 1st FP modes is shown in Figure 4.18(b). Under uniform 1480 nm pumping, the 1st FP mode exhibits a typical S-shaped curve, signifying a lasing threshold (the OSA's noise floor covers the part below the threshold). Conversely, the Fano mode does not display this behavior. It operates solely within the amplified spontaneous emission region, showing a linear increase in output power when the other FP modes are present. A typical S-shaped lasing threshold curve for the Fano mode becomes apparent when the Fano laser cavity (LHS WG) is pumped with a 980 nm laser in the absence of the 1480 nm pump, as shown in Figure 4.18(c). This suggests that when FP modes are present, the Fano mode lasing is somehow suppressed.

4.7.2   Characterization of optical-induced thermal modulation

Given that the femtosecond pulse source applied in Section 3.5 offers pulses too short for the system to reach its steady state, and broadening the femtosecond pulse would result in inadequate peak power, we turn to use thermal modulation. Here, we employ a 980 nm continuous wave laser source, which has photon energy marginally below the InP bandgap energy, enabling two-photon absorption and efficient light-to-thermal energy transfer while minimizing direct linear absorption (though linear absorption still occurs in the area with quantum well structure) for an unwanted pumping effect. We characterized the thermal-induced wavelength shift of feedback Fano lasers by measuring the emission spectra dependence on temperature. This measurement is performed on another sample that, after several months, had degraded to a non-lasing state. However, their thermal characteristics are similar.

The device's temperature was adjusted by placing it on a platform connected to a temperature controller, ensuring a precision of 0.01 K. The data presented in Figure 4.19(a) shows the wavelength against temperature for Fano and FP modes, consistently showing a linear increase at a rate of 0.104 nm/°C, indicating uniform heating across the device by the temperature controller. The decrease in wavelength observed between 22 to 24 °C is attributed to mode hopping. Due to the absence

(a)

(b)

(c)
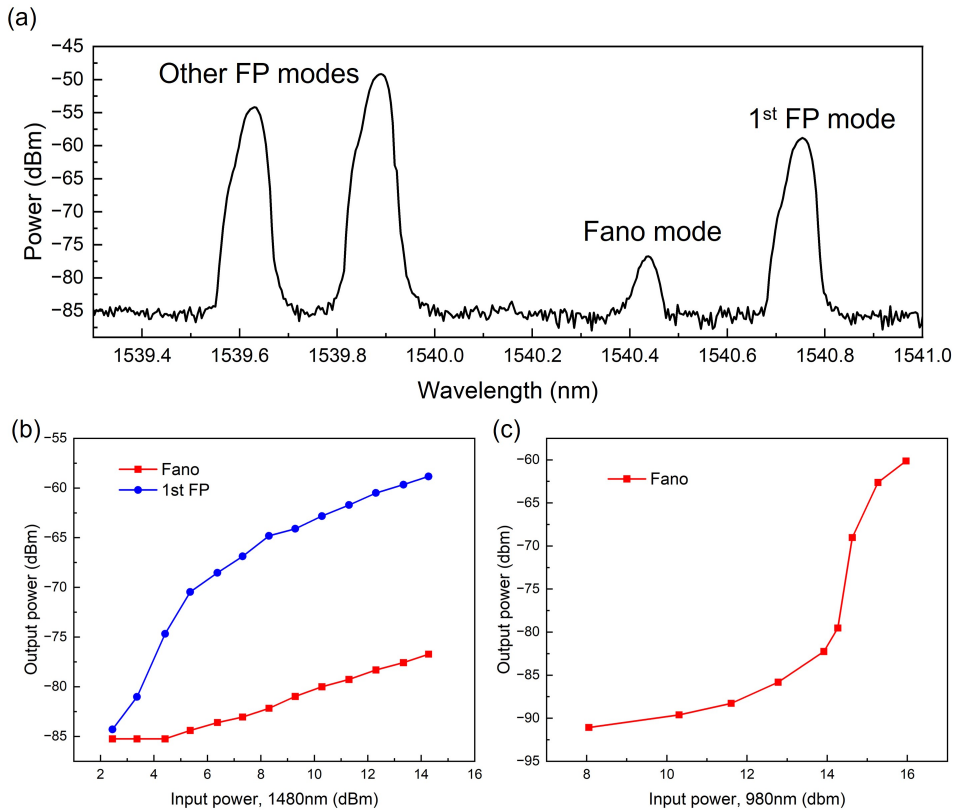
Figure 4.18. (a) Emission spectrum of the feedback Fano laser. The peak at 1540.44 nm is identified as the Fano mode and the adjacent peak at 1540.75 nm is termed as the 1st FP mode. (b) L-L curve for the Fano mode and the 1st FP mode under a 1480 nm pump through the grating coupler. (c) L-L curve for the Fano mode when vertically pumped with a 980 nm laser atop the LHS WG.

of active material, simply illuminating the NC with the modulation light proved insufficient for inducing the necessary index shift. Therefore, we directed a 980 nm laser at the midpoint atop the RHS WG to induce temperature changes in the sample. Though this might alter the refractive index and consequently the effective cavity length of the external cavity, it has been shown that variation of the external cavity length does not significantly affect the modes' frequency when the NC detuning is not too large (see Figure 4.8). The measurements of the optical-thermal characteristics under the injection of the 980 nm laser in Figure 4.19(b) reveals a wavelength shift for the Fano mode at a rate of 0.00453 nm/mW, correlating to a temperature increase of 0.0436 °C/mW. Additionally, an output power increase of 0.09457 mW/mW (980

nm) was observed. Since altering the external cavity length also does not significantly affect the modes' lasing threshold(see Figure 4.8), it is likely that this output power variation is a result of an additional pumping effect produced by the 980 nm laser.
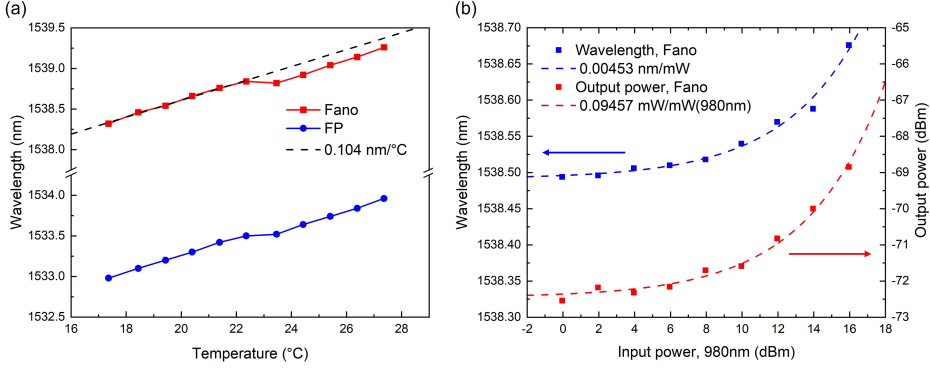
Figure 4.19. (a) Emission peak wavelengths of the Fano mode and the adjacent FP mode (1st FP mode) versus temperature. Temperature control is achieved with a precision of 0.01 K. The black dashed line represents a linear fit of the initial six data points for the Fano mode before the occurrence of mode hopping. (b) Variations in the wavelength and peak power of the Fano mode in response to the input power of a 980 nm laser. Dashed lines indicate fitted curves representing the optical-thermal response characteristics.

4.7.3   Pumping spot position and its influence on excited modes

The influence of non-uniform pumping becomes significant when directing a small-diameter beam at the WG. The location of the pumping spot is crucial for determining which modes are excited. We utilize the multi-section approach to simulate a symmetric feedback Fano laser under non-uniform pumps, considering a realistic diffusion rate, D_{real}, and assuming $\alpha = 0$. A pump with a finite diameter of 3 μm is centered on the midpoints of the LHS WG and the RHS WG, respectively. We apply a pumping power of 100 R_{th} for the LHS WG, while for the RHS WG, the power is set at 100, 128, and 130 R_{th}, corresponding to the right to the left column in Figure 4.20. With the NC detuning σ_c set to 3, we position the laser within the bistable region (refer to Figure 4.5(b)). When both WGs receive equal pumping power, the Fano mode with the normalized frequency value near 3 emerges as the dominant lasing mode, as seen from the Fourier transform spectrum (the bottom-row panels in Figure 4.20(a) and (b)). Upon increasing the RHS pumping power, the Fano mode becomes unstable at a certain threshold, showing fluctuations in output power and the NC internal energy (Figure 4.21(b)). Beyond this threshold, the NC energy decays, leading to the dominance of the FP mode (Figure 4.20(c)). This suggests that almost no coexistence of Fano and FP modes occurs in a symmetric feedback Fano laser. A
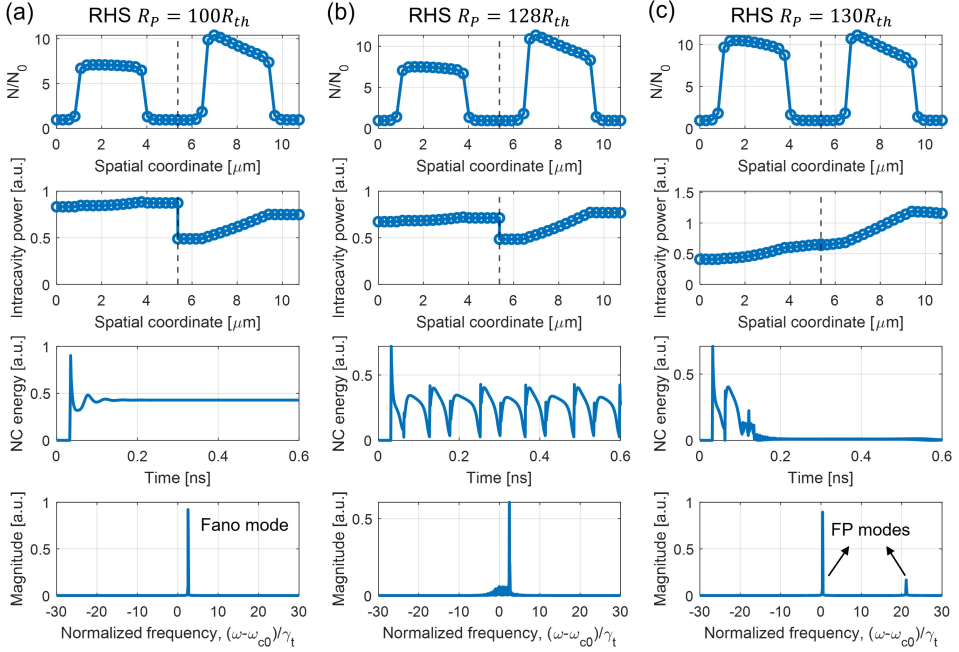
Figure 4.20. Simulation results for symmetric feedback Fano lasers with dual pumping on the LHS and RHS WGs, with RHS pumping rates of (a) 100 R_{th}, (b) 128 R_{th}, and (c) 130 R_{th}. The LHS pumping rate is fixed at $100R_{th}$, with an NC detuning of $\sigma_c = 3$. The beam diameter for each pump is set at 3μm. The top-row panels show the carrier density spatial profile, with the origin at 0μm corresponding to the LHS mirror. The second-row panels show the spatial distribution of the intracavity power. The third-row panels show the temporal dynamics of the NC energy. The bottom-row panels show the Fourier transform spectra. In the spectra of (a) and (b), the mode with a normalized frequency value close to 3 is identified as the Fano mode. However, in the spectrum of (c), the Fano mode disappears, and FP modes appear.

non-uniform pump with stronger power on the RHS may compensate for the large loss of the external cavity and excite the FP mode. However, this compensation can also stem from the extension of the external cavity and the gain medium. In further simulations shown in Figure 4.21, where we gradually increase the external cavity length with a uniform pump, we use a low pumping rate $R = 10R_{th}$ and set $\sigma_c = 0$. For a symmetric structure, the laser stabilizes in the Fano mode. However, as L_2 extends to 9.40 μm, multiple FP modes appear. When L_2 goes even higher to 12.08 μm, the Fano mode is suppressed, and multiple FP modes appear. This simulation provides insights into our experimental findings: In a feedback Fano laser with an asymmetrical design, the extended external cavity that incorporates additional gain

can lead to the dominance of FP modes, which in turn suppresses the Fano mode.
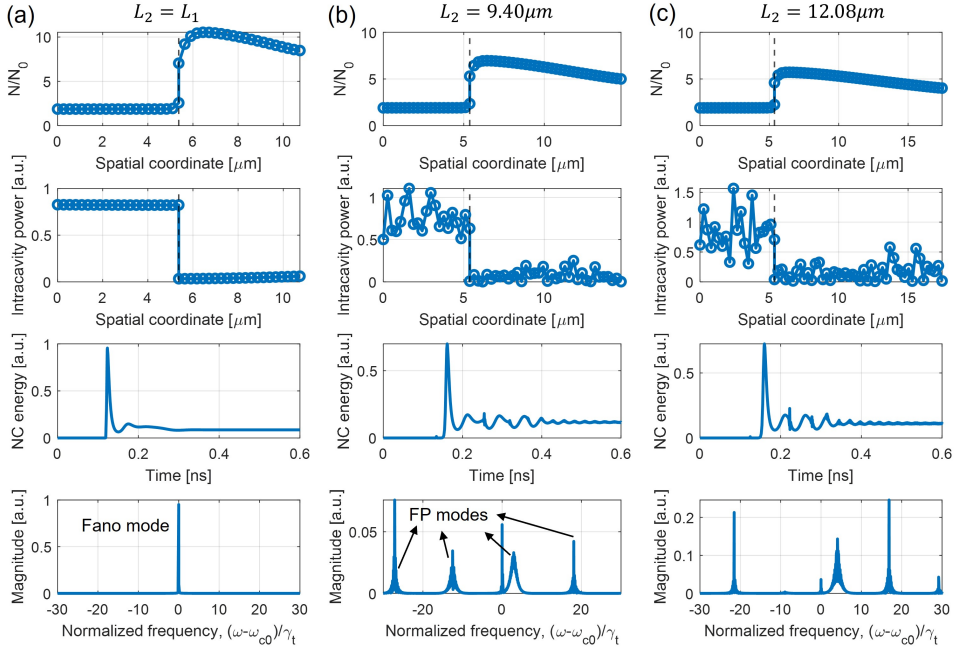
Figure 4.21. Simulation results for asymmetric feedback Fano lasers with uniform pumping with RHS WG length of (a) 5.3 μm, (b) 9.4 μm, and (c) 12.1 μm. The pump rate is set at $10R_{th}$, with an NC detuning of $\sigma_c = 0$. The Fano mode in the bottom-row panels exhibits a normalized frequency value of 0.

We then measured the sample with a 980 nm pump atop the LHS WG and the 1480 nm uniform pump from the GC to simultaneously excite the Fano and FP modes. Figure 4.22(a) shows the spectral variations with increasing 980 nm pump power, revealing a redshift in the Fano mode, while the 1st FP mode remains unshifted. As shown in Figures 4.22(b) and (c), a sudden increase and subsequent decrease in power marks the overlapping and subsequent separation of the Fano mode and the 1st FP mode. The separation indicates that the laser does not stabilize in the FP mode after the overlap, and hence, no bistability is observed in this sample. This preliminary sample based on two-dimensional PhC might have complicated effects such as slow light [5], band-edge lasing [115], and Anderson localization [114], making it difficult to differentiate various modes and effectively excite the Fano mode. Additionally, the suspension slab structure results in mechanical instability, making it difficult to control the laser operating in the bistability region. Future experiments could be conducted on a symmetric feedback Fano laser based on a one-dimensional nanobeam

structure [102,116], which could avoid challenges such as mechanical instability, slow
light-induced band-edge lasing and the difficulty in identifying multiple high-order
modes [104], thereby enabling more precise control on the Fano mode.
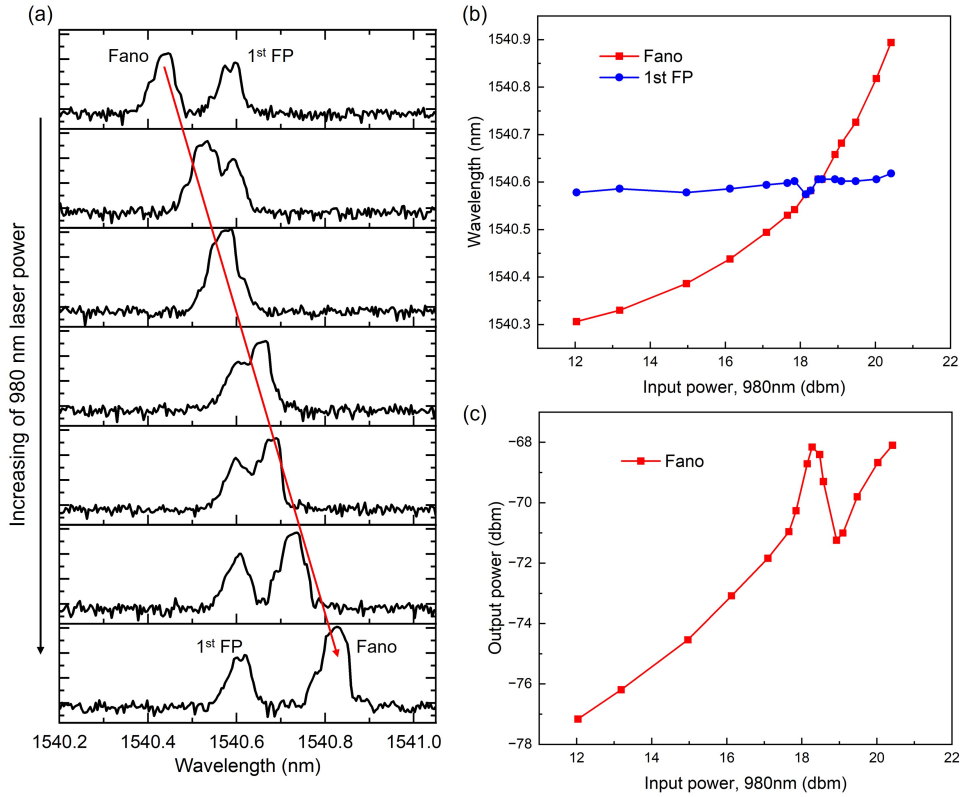
Figure 4.22. (a) Emission spectra of the feedback Fano laser with the 980 nm pump atop
the LHS WG and the 1480 nm uniform pump from the grating coupler. The spectra demon-
strate the overlap and separation of the Fano mode and the 1st FP mode with increasing
980 nm pump power. (b) Variations in the wavelength of the Fano mode and the 1st FP
mode as a function of 980 nm laser power. (c) The output power of the Fano mode as a
function of 980 nm laser input power.

Parameter	Symbol	Value
Original NC frequency	ω_{c0}	1.215×10^{15} Hz
NC coupling Q	Q_c	500
NC vertical scattering Q	Q_v	10^5
NC internal loss Q	Q_i	86000
WG internal loss	α_i	10 cm^{-1}
LHS mirror reflection coefficient	r_L	-0.9
Phase and group indices	n, n_g	3.5
Confinement factor	Γ	0.01
Differential gain	g_n	5×10^{-16} m^{-2}
Transparency carrier density	N_0	5×10^{21} m^{-3}
Carrier lifetime	τ_c	0.28 ns
Cross-section of WG mode	A	1.05×10^{-13} m^2
LHS WG length	L_1	5.37 μm
Threshold pumping rate	R_{th}	3.325×10^{31} m^{-3}s^{-1}
Free carrier dispersion coefficient	K_{car}	1.95×10^{-12} m^{3}s^{-1}
Two-photon absorption coefficient	β_{TPA}	2.4×10^{-10} m/W
Effective two-photon absorption mode volume	V_{TPA}	2.1×10^{-19} m^3

Table 4.1. Simulation parameters used in Chapter 4.

Stochastic simulation of semiconductor nanolasers

5.1 Introduction

The preceding chapters focus on lasers, despite being designed with micro to nanometer-scale structures, operating with a significant number of carriers and photons, which allows the dynamic equations to be solved by ignoring the shot noise of photon and carrier numbers due to the small relative fluctuation compared to their mean values. However, more refined dynamics equations become essential as we approach the lasing threshold, where nanolasers operate with only a few intra-cavity photons or carriers. This is particularly important for lasers employing quantum dots as the gain medium, where the reduced number of emitters necessitates a more detailed and accurate approach to model their behavior [117]. Moreover, pursuing benefits such as reduced power consumption [7] and high modulation speeds [118] leads to a continuous reduction in the physical size and alters certain fundamental properties of lasers. For instance, reducing the available number of cavity modes increases the proportion of spontaneous emission photons channeled into lasing modes [119]. In this case, the β-factor, described in Equation 2.2, gains importance. Figure 5.1 shows the laser intra-cavity photon number (proportional to the laser output power) against the pumping rate for different β values. Notably, as β increases, the kink in these curves becomes less pronounced, and the lasing threshold is less clearly defined. As β approaches 1, the curve nearly flattens, suggesting the laser can become almost "thresholdless [120]." This is an example of how microscopic quantum effects can affect the macroscopic behavior of lasers.

When the average number of photons in the cavity is low, spontaneous emission becomes crucial; under such conditions, photon noise can substantially influence the laser dynamics. A standard method to introduce stochastic noise sources into the conventional semiconductor laser model is incorporating Langevin noise, denoted as $F_i(t)$ [52]. The correlation function for such noise is given by $\langle F_i(t)F_j(t-\tau)\rangle = S_{ij} \cdot \delta(\tau)$,
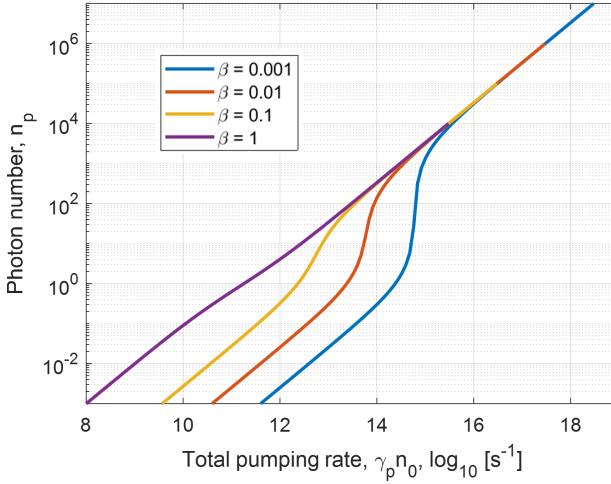
Figure 5.1. Photon number n_p as a function of total pumping rate $\gamma_p n_0$ for different β-factors. Here, the product of the total number of emitters n_0 and the β-factors is fixed at 300. The data presented in this figure is calculated using Equation 5.2 at steady state.

where S_{ij} represents the correlation strength and $\delta(\tau)$ is the Dirac delta function. The noise spectrum of laser intensity can be analyzed by utilizing the relationship between the correlation function and spectral density, described by Wiener–Khinchin theorem [52]. However, the Langevin equation is based on continuous variables. This formulation overlooks the inherent discrete nature of photons and carriers characterized by the Poisson processes [121]. For systems with large average values, the Poisson process with discrete variables can be approximated as Gaussian distribution with continuous variables [122], validating the Langevin equation's assumptions. However, as the size of the laser decreases, this approximation might no longer hold. Additionally, when the numbers of photons and carriers are near zero, $F_i(t)$ can potentially yield negative values, leading to unphysical results. Therefore, a more appropriate approach to simulate the dynamics of nanolasers is to employ a discrete stochastic model [123–125].

In a discrete stochastic model, the evolution of carriers and photons is computed event by event. Each event alters the carrier number, n_e, or the photon number, n_p. The occurrence of these events is dictated by the Poisson process, capturing the probabilistic and random nature of quanta. By implementing this model, the inherent shot noise is considered in calculations and revealed in the statistical properties of the photon number, which is important for quantum optics applications. The next section will introduce and delve into two discrete stochastic algorithms: the Fixed Time Increment method (FTI) and Gillespie's First Reaction Method (FRM) [125].

5.2 Stochastic laser rate equations

5.2.1 Fixed time increment method (FTI)

An intuitive approach to numerically solve the laser rate equations by iteration is to update the system's parameters with fixed time intervals, simulating the laser dynamics with differential rate equations. Consider a laser consisting of carriers with two energy levels located within the cavity and interacting only with a single mode. These carriers can either be in the ground or the excited state, with the total number of carriers being n_0. Several events can alter the number of excited carriers n_e, or the number of photons n_p within the laser, including stimulated emission, spontaneous emission, re-absorption (photon absorption by carriers in the ground state before exiting the cavity), cavity-loss (the loss of photons from the cavity through mirror loss), pumping, and background decay (non-radiative recombination or emission into non-lasing mode). The average rates of each event are listed in Table5.1 [124].

Event	Symbol a_x	Average rate
Stimulated em.	a_{st}	$\gamma_r n_e n_p$
Spontaneous em.	a_{sp}	$\gamma_r n_e$
Re-absorption	a_{ra}	$\gamma_r (n_0 - n_e) n_p$
Cavity-loss	a_c	$\gamma_c n_p$
Pumping	a_p	$\gamma_p (n_0 - n_e)$
Background decay	a_{bg}	$\gamma_{bg} n_e$

Table 5.1. Average rate and the symbols used for each event type in the laser rate equations.

Here, γ_r is the rate at which a carrier is emitted into the lasing mode. The ratio of γ_r to the total carrier decay rate γ_t is defined as the spontaneous emission β factor, signifying the proportion of spontaneous emission photons emitted into the lasing mode:

$$\beta = \frac{\gamma_r n_e}{\gamma_t n_e} = \frac{\gamma_r}{\gamma_t} = \frac{\gamma_r}{\gamma_r + \gamma_{bg}} \tag{5.1}$$

with $\gamma_t = \gamma_r + \gamma_{bg}$, and γ_{bg} being the background decay rate for a carrier. According to Einstein's relation [126], absorption would have the same rate as stimulated emission, meaning it also has the rate γ_r. The term γ_c is the cavity loss rate for a photon, and γ_p is the pumping rate for a carrier. Note that here, we consider the possibility of photons undergoing re-absorption before exiting the cavity [127]. Also, we consider the pumping saturation due to the Pauli blocking principle [128]. This effect is less likely present in semiconductor lasers that utilize bulk gain materials, whose continuous band structure provides more available excited states. However, this effect becomes essential when investigating lasers with gain materials having two-level states, such as quantum dot lasers.

According to Table 5.1, the laser rate equations with discrete variables can be expressed as [124]:

$$\frac{dn_p}{dt} = a_{sp} + a_{st} - a_{ra} - a_c$$
$$= \gamma_r n_e + \gamma_r(2n_e - n_0)n_p - \gamma_c n_p \qquad (5.2)$$

$$\frac{dn_e}{dt} = a_p - a_{sp} - a_{st} + a_{ra} - a_{bg}$$
$$= \gamma_p(n_0 - n_e) - \gamma_r(2n_e - n_0)n_p - \gamma_t n_e \qquad (5.3)$$

Now, we can iteratively solve the differential laser rate equations using the FTI algorithm. The procedure is outlined as follows [125]:

1. Initialization: Set initial values for n_p and n_e at time $t = 0$.

2. Rate Calculation: For each event type x, calculate its corresponding average rate, represented as a_x.

3. Drawing the number of events occurring: Utilize the Poisson distribution to determine the number of times each event x occurs during the time interval dt. The mean value for the Poisson distribution is given by $a_x dt$.

4. Renewal: Update the values of n_e and n_p accordingly and adjust the time from t to $t + d\tau_x$.

With this procedure, the iterative rate equation can then be written as:

$$n_{p,i+1} = n_{p,i} + p_{sp} + p_{st} - p_{ra} - p_c \qquad (5.4)$$

$$n_{e,i+1} = n_{e,i} + p_p - p_{sp} - p_{st} + p_{ra} - p_{bg} \qquad (5.5)$$

Here, i is the current calculation step index, and p_x is the occurrence times of the event x, which is drawn following the Poisson distribution.

A critical factor in maintaining the accuracy of the model is the selection of a suitable time increment, denoted as dt. Ideally, $1/dt$ should be significantly faster than the rate of the fastest occurring event in the system. This ensures that the number of events drawn remains either one or zero for each event. If the number of events drawn exceeds one in a single iteration, the changes in n_e and n_p resulting from each event will overlap, leading to a deviation from the ideal Poisson process. To avoid this issue, one can alternatively fix the "fractional time increment," f_t. By adjusting the time increment to $dt = f_t/a_{max}$ during each iteration, where a_{max} represents the fastest event rate, we ensure that the iteration rate consistently remains much faster than the rate of any event throughout the simulation. This adjustment adapts to changes in the event rate as the simulation progresses. The influence of f_t on the event occurrence number can be examined by considering $P(X \leq k)$, which is the probability that the drawn number of events occurring is less than or equal to a certain value k. This probability can be calculated using the cumulative distribution function of the Poisson distribution:

$$P(X \leq k) = e^{-\lambda} \sum_{j=0}^{k} \frac{\lambda^j}{j!} \qquad (5.6)$$

where λ is the average value of the Poisson distribution. In Figure 5.2, the dependence of $P(X \leq 1)$ on f_t is demonstrated. Notably, to ensure $P(X \leq 1)$ surpasses 90%, f_t should be kept below 50%. By decreasing f_t to just 1%, $P(X \leq 1)$ can rise to nearly 99.995%. However, it is essential to find a balance since an excessively small f_t will lead to a considerable increase in computation times.
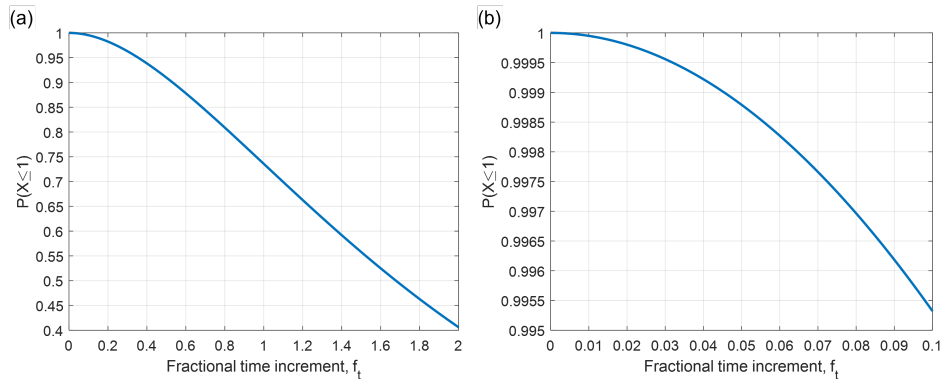
Figure 5.2. (a) The probability that the drawn number of events is less than or equal to one, $P(X \leq 1)$, as a function of the fraction time increment, f_t. (b) detailed zoom-in view of (a), focusing on the range of f_t from 0 to 10%.

5.2.2   Gillespie's first reaction method (FRM)

FTI algorithms can sometimes lead to ambiguities in the order of event occurrences [125]. This issue arises when multiple events occur within a single time step. For instance, at a given time t, there are $n_e(t)$ excited carriers. If spontaneous emission happens before stimulated emission, the spontaneous emission rate would be $\gamma_r n_e(t)$, and the subsequent stimulated emission rate would be $\gamma_r(n_e(t)-1)n_p(t)$. Conversely, if stimulated emission precedes spontaneous emission, the rates would be $\gamma_r n_e(t)n_p(t)$ for stimulated emission and $\gamma_r(n_e(t)-1)$ for spontaneous emission. However, in FTI, if both spontaneous and stimulated emissions happen within the same time interval from t to $t + dt$, the algorithm counts the number of excited carriers available for both events as $n_e(t)$, introducing deviations from the actual physical process. Such deviations become more pronounced when the time step size increases, resulting in the number of event occurrences exceeding one. To circumvent this problem, an alternative approach known as the first reaction method can be employed. Daniel T. Gillespie first introduced this method in quantum chemistry simulations [129]. FRM algorithm adopts a different approach compared to the method of drawing the number of events within a time step. FRM identifies the first occurring event by estimating the waiting time for each possible event and then selecting the one with the shortest duration. The calculation procedure for the FRM is outlined as follows [125]:

1. Initialization: Set initial values for n_p and n_e at time $t = 0$.

2. Rate Calculation: For each event type x, calculate its corresponding average rate, represented as a_x.

3. Drawing waiting times of events: For each event x, calculate tentative waiting times τ_x using the formula $\tau_x = -log(r_x)/a_x$, where r_x is a randomly generated number between 0 and 1.

4. Determine the occurring event: Identify the event with the shortest waiting time, τ_x.

5. Renewal: Update the values of n_e and n_p accordingly and adjust the time from t to $t + d\tau_x$.

The tentative time τ_x is the duration required for the event to occur. It is derived from the "reaction probability density function" $P_x(\tau)$. The term $P_x(\tau)d\tau$ represents the probability for the event x that its next reaction will occur in the period $(t + \tau, t + \tau + d\tau)$. Here, $P_x(\tau)$ is the product of the probability $P_0(\tau)$ — the probability that event x remains fixed between $(t, t + \tau)$ and $a_x d\tau$ — the probability of event x do occur between $(t + \tau, t + \tau + d\tau)$. It can be recognized that $P_0(\tau)$ is just the cumulative distribution function of the Poisson distribution when $k = 0$; therefore, $P_0(\tau) = e^{-a_x \tau}$ [129]. Consequently, we have:

$$P_x(\tau)d\tau = a_x e^{-a_x \tau} d\tau \tag{5.7}$$

By randomly picking a number between 0 and 1, we can get a random sampling from the cumulative distribution function of $P_x(\tau)$, and therefore obtain the tentative waiting time $\tau_x = -log(r_x)/a_x$ following the distribution $P_x(\tau)$ [129] . The iterative rate equation in this method becomes:

$$n_{p,i+1} = n_{p,i} \begin{cases} +1 & x = sp, st \\ -1 & x = c, ra \end{cases} \tag{5.8}$$

$$n_{e,i+1} = n_{e,i} \begin{cases} +1 & x = p, ra \\ -1 & x = sp, st, bg \end{cases} \tag{5.9}$$

This method would either increase or decrease n_e and n_p each iteration, avoiding the mix-up of event orders like in the FTI method.

5.2.3   Computational efficiency analysis: FRM vs. FTI

In FRM, the time step for each iteration varies because each drawn waiting time τ_x is different. This poses a difficulty when attempting to take the ensemble average (the average over multiple trials). Due to the varying lengths of time steps in each iteration, the recorded values of photon and carrier numbers from various trials do not align on the same time points. One potential solution is to first take time averages for each individual trial and then calculate their average. However, this method is limited to systems in stationary states and is not applicable to cases where the system state is not stable over time. Another way to address this issue is to do resampling. This

method generates new data points that have the same time intervals, with the value of each new point determined based on the nearest preceding old data point. Note that the resampling interval is chosen to be no larger than the smallest τ_x encountered in the raw data to avoid losing resolution in the resampled data. However, while resampling can normalize the time intervals of the data, it significantly increases the size of the dataset to an unpredictable extent. In contrast, FTI algorithm offers an inherent advantage in terms of data alignment when a fixed time increment dt is used (Note that using fixed fractional time increments would still give varying lengths of time intervals). The trade-off with the FTI algorithm, however, is the potential ambiguity in the order of event occurrences, as mentioned earlier.
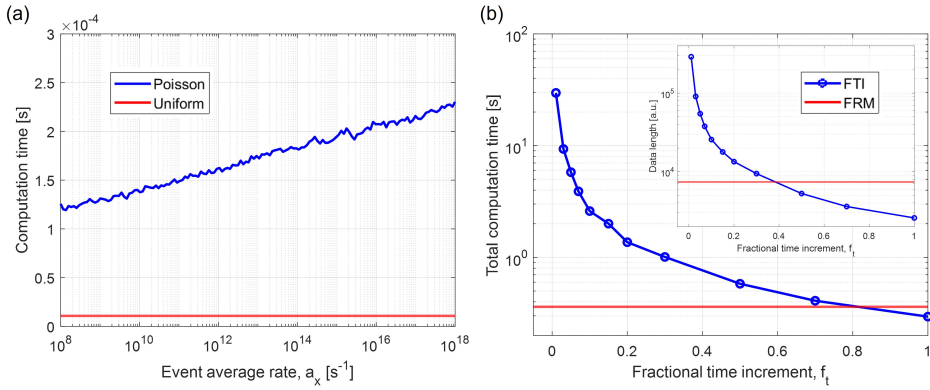
Figure 5.3. (a) Computation time required for a single draw as a function of the average event rate a_x, compared between the Poisson and uniform distributions. Here, the data is an average taken over 300 trials. (b) Total computation time for a single simulation trial using both the FTI and FRM algorithms, plotted against the fractional time increment f_t. The simulated duration is 1ns. The inset depicts the corresponding variations in data length. The parameters used for this simulation are $n_0 = 200$, $\gamma_p = 5 \times 10^{10}$ s^{-1}, and $\beta = 0.1$.

When comparing FTI and FRM, FRM exhibits better computational efficiency, particularly when the event average rates of events are not excessively high. A key factor contributing to this difference lies in the methods each employs for generating random numbers. The process of drawing a number following the Poisson distribution, as utilized in the FTI algorithm, is more time-consuming than the approach of drawing a number from a uniform distribution between 0 and 1, as utilized in the FRM algorithm.

Figure 5.3(a) shows the computation time against the event average rate a_x for both the Poisson distribution and uniform distribution (For all the simulations presented in this chapter, we set $\gamma_t = 10^{10}$ s^{-1}, $\gamma_c = 10^{11}$ s^{-1}, unless specified otherwise). The time required for drawing from the Poisson distribution is longer than that for a uniform distribution and tends to increase with the event rate. This significantly affects the total computation time..

Figure 5.3(b) shows how the total computational time for a single simulation trial using FTI varies with the fractional time increment f_t. When f_t is changed from 1% to 10%, there is a 90% reduction in computation time (from 30 to 3 seconds). The inset in this figure illustrates the relation between data length (which can be equated to the number of iterations) and f_t, revealing a trend that is similar to the computational time. As seen, FRM consistently outperforms FTI in terms of memory efficiency until f_t exceeds 40%, and in terms of computational time until f_t exceeds 80%, where FTI already largely deviates from the ideal Poisson process. Further analysis demonstrates FRM's superior efficiency across various pumping rates [125].

5.2.4   Stochastic simulation of a time-varying pump rate

In situations where the external pump varies in time, accurately sampling the pumping rate function, $\gamma_p(t)$, over time becomes crucial. For FTI with a constant dt, capturing the time-varying characteristics of $\gamma_p(t)$ is straightforward, as long as dt is small enough to reflect the pump source's variations accurately. However, this task becomes more challenging in FRM (or in FTI with a fixed f_t). In these methods, time intervals between events vary based on event rates. When the pumping rate is close to zero, both n_e and n_p are typically low, leading to longer drawn time intervals. This extended duration can miss the finer variations in the pumping source (or any other external time-varying parameters).

One solution to this problem is to impose an upper limit on the time step, denoted as dt_{lim}. If the drawn dt surpasses dt_{lim}, the values for n_e and n_p are carried over from the previous step, but the time is updated as $t \to t + dt_{lim}$. This approach prevents large time steps, particularly during periods of near-zero pumping. It proves especially beneficial when examining the turn-on transient dynamics of lasers. Figure 5.4 shows the impact of using dt_{lim} on simulation results. In Figure 5.4(a), the gradual increase of the sampling signal from a triangular signal pump source is lost due to the large time leaps caused by the low initial pumping rate. However, by setting dt_{lim} to 10^{-12} seconds, as shown in Figure 5.4(b), the sampled signal closely follows the pattern of the original signal, thereby preserving the dynamics of the modulated pump.

5.3   Dynamics of nanolasers near threshold

5.3.1   Photon burst phenomenon

When the laser crosses the lasing threshold, there is a transition region from incoherent spontaneous emission to coherent stimulated emission. Historically, this transition was conceptualized as a mixture of coherent and incoherent photons. With increasing pumping power, the proportion of stable coherent photons grows faster than incoherent photons, ultimately predominating in the lasing field. Under this model, photon statistics are thought to be represented by a superposition of both the
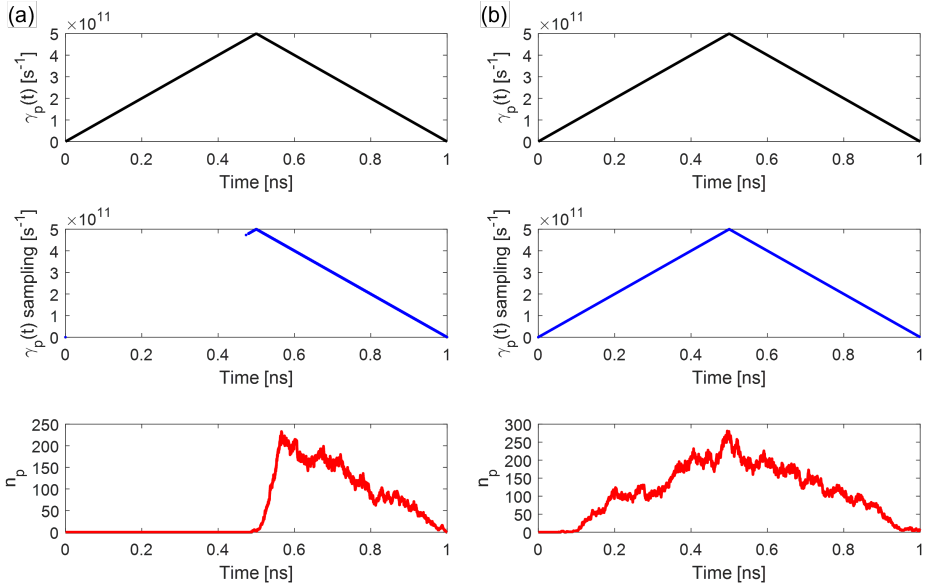
Figure 5.4. Demonstration of the effect of setting a time step limit dt_{lim} with a time-varying pumping source. (a) Without applying dt_{lim}, the initial rising ramp of the sampled pumping signal is lost, leading to a zero value of photon number. (b) Results with setting $dt_{lim} = 10^{-11}$ s, showing improved signal sampling that captures the dynamic changes in the pumping rate. The parameters used for this simulation are $n_0 = 200$ and $\beta = 1$. A small bias of $\gamma_{p0} = 10^7$ s^{-1} is added to the time-varying pump to prevent the time step from being infinitely large.

Poisson and Bose-Einstein distributions [130]. This transition is difficult to observe in macroscopic lasers due to the extremely narrow transition zone [39]. However, when lasers are miniaturized, an increased β-factor broadens this lasing transition region, as depicted in Figure 5.1. Certain experiments have detected a unique phenomenon called "photon bursts," marked by coherent pulses immersed within an incoherent photon background in this transition region [39]. This observation is supported by phenomena like oscillations in the second-order time-delayed autocorrelation function $g^{(2)}(\tau)$, fluctuating above and below unity [131]. These oscillations indicate amplitude fluctuations in the coherent pulses. Additionally, direct observations of sharp intensity spikes have been recorded [131]. Notably, the appearance of superthermal statistics, where $g^{(2)}(0) > 2$, an unexpected behavior during the thermal to the Poisson transition, has been measured in micro vertical-cavity surface-emitting lasers (VCSELs) [132]. Stochastic simulations have also observed the photon bursts phenomenon for quantum well lasers [133], which can not predicted by the conventional differential laser rate equations [39].

Photon bursts can be attributed to the excessive accumulation of carriers before

coherent emission. When the cavity lacks photons, the probability of excited carriers undergoing stimulated emission is significantly low. Despite some small fluctuations, these excited-state carriers rarely relax into photons, leading to a continuous accumulation of carriers to a high level. When the high carrier number eventually leads to a high spontaneous emission rate, a cascade of stimulated emission can be initiated, releasing a coherent pulse. This mechanism is like an intrinsic Q-switching, where energy stored in carriers is rapidly released due to an abrupt change in the stimulated emission rate. After the pulse release, the low pumping power hinders the rapid re-pumping of carriers and prevents them from generating stable coherent photon emissions. As a result, the laser returns to a state of low photon number, thereby restarting the cycle. This phenomenon is even apparent in intermediate low-β lasers (β in the range of 0.01 to 0.1). In these lasers, the proportion of spontaneous emission into the lasing mode is not that large, leading to photon pulses occurring less frequently but tend to be much stronger and broader than those in high-β lasers, as shown in Figure 5.5. Notably, high-β lasers can exhibit larger relative fluctuations near the threshold, as evidenced by the relation $\delta n_p / \langle n_p \rangle \simeq \beta^{1/4}$ [134]. This relationship is derived from differential laser rate equations considering the contributions from spontaneous emission. However, small signal stability analysis [52] reveals that high-β lasers typically have more negative eigenvalues, which means that any fluctuations in photon or carrier numbers tend to decay more rapidly [39]. This implies that, despite more frequent and large relative fluctuations, high-β lasers still exhibit intrinsic stability that exceeds low-β lasers.
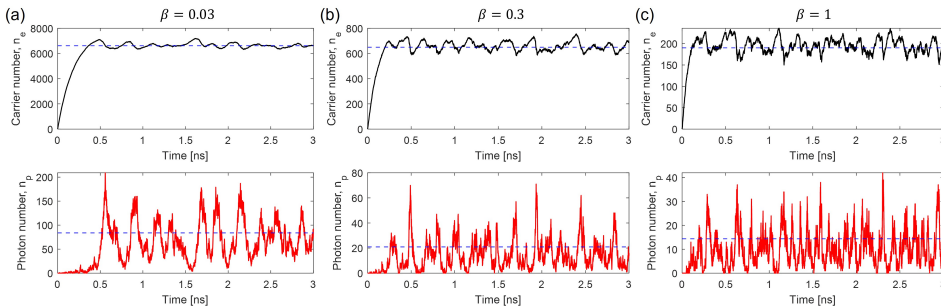
Figure 5.5. Demonstration of photon burst phenomenon using stochastic simulation for (a) $\beta = 0.03$ with total pumping rate $\gamma_p n_0 = 4 \times 10^{13}$ s^{-1}, (b) $\beta = 0.3$, $\gamma_p n_0 = 6 \times 10^{12}$ s^{-1}, and (c) $\beta = 1$, $\gamma_p n_0 = 3 \times 10^{12}$ s^{-1}. The blue dashed lines denote the average value of either carrier or photon number after $t = 0.5$ ns. These simulations were conducted using FRM algorithm.

5.3.2   Turn-on transient dynamics of nanolasers

While photon bursts offer the potential for ultra-low power self-pulsing and observing superthermal light emission, their inherent randomness poses limitations for certain

applications, such as imaging techniques [135]. Inspired by this phenomenon, we
sought to explore the dynamics of small lasers under a near-threshold pumping pulse.
In this study, we utilized FRM to simulate the behavior of a laser with pulse pump-
ing. Figure 5.6, serves as an illustrative example, showing the temporal changes in
the pumping signal and the corresponding photon number. To align with practical
applications, we consider the signal received by a photon detector. Note that the
statistical properties differ between intra-cavity and out-coupled photons [136]. The
detector's integration time is set at one femtosecond. Although this duration is con-
siderably shorter than the response times of the fastest available detectors (on the
order of picoseconds [137]), extending it further would result in losing pulse details.
The pump signal has the shape of a square pulse, turned on at 0.1ns and sustained
for various durations. We define a specific range for the output pulses to exclude the
influence of signal tails before and after the square pumping pulse on photon number
statistics. The initial laser turn-on delay signals and the relaxation tails after the
pump turn-off will be discarded, as these sections generally exhibit unwanted near-
zero photon numbers. In Figure 5.6, the horizontal line indicates the cutoff level used
to define the pulse range, with vertical lines marking the corresponding cutoff time
points. To define the pulse period precisely in the presence of significant noise, we
only consider time intervals where the photon number exceeds the defined cutoff sig-
nal level. This level is set at 5% of the peak photon number, rounded to the nearest
integer. This period extends until the pump is turned off and the photon number
falls below this cutoff threshold for the first time.

Figure 5.7(a), (b), and (c) show the autocorrelation function $g^{(2)}(0)$ as a function
of pulse width at three distinct pumping rates close to the lasing threshold with β
values of 0.03, 0.3, and 1. The autocorrelation function $g^{(2)}(0)$ can be calculated
by [138]:

$$g^{(2)}(0) = 1 + \frac{\langle \delta n_p{}^2 \rangle - \langle n_p \rangle}{\langle n_p \rangle^2} \tag{5.10}$$

where $\langle n_p \rangle$ is the average photon number, and $\langle \delta n_p{}^2 \rangle$ is the variance of photon number.
Ensemble averaging is used here since long-time averages can not be taken for short
pulse pumping. Each point in the figure represents an average of 10 trials. Dashed
lines represent the steady-state $g^{(2)}(0)$ under time-invariant pumps. As expected,
every curve approaches the time-invariant pumping steady-state solutions as the pulse
width expands. This is attributed to the decreasing influence of the pulse's rising
and falling edges over its entire pulse duration. With the increasing pumping power,
there is a noticeable decline in $g^{(2)}(0)$, particularly for shorter pulses. This observation
suggests that the statistical properties during the transient rise and fall edges are more
sensitive to the pumping power than the steady-state behavior. Notably, even when
the steady-state $g^{(2)}(0)$ is below 2, shorter pulses can still yield superthermal light
emissions, concluding that the rising and falling edge might contribute significantly
to superthermal emission. Remarkably, low-β lasers can exhibit higher $g^{(2)}(0)$ values
for short pulses compared to their higher-β counterparts (for example, comparing the
blue lines in (b) and (c), which have the same $g^{(2)}(0)$ for DC pumping but different
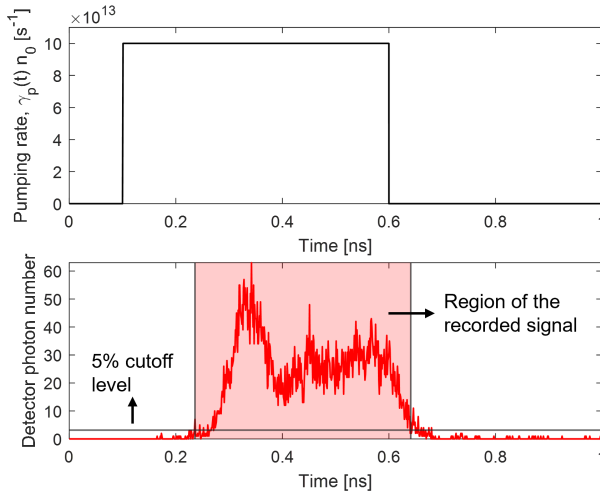
Figure 5.6. Illustration of pulse signal extraction methodology. The upper panel shows a square-pulse, time-varying pumping source. The lower panel shows the photon number signal received by the detector, with an integration time of 1 fs. In the lower panel, the horizontal line marks the 5% maximum photon number cutoff level, while the two vertical lines mark the corresponding cutoff time points. The region of the signal for recording is highlighted in light red.

$g^{(2)}(0)$ variation for pulse pumping.). This could be due to the rapid rise and fall processes under near-threshold pumping, mimicking the photon burst phenomenon with superthermal statistics [132], which are more pronounced in lower-β lasers.

Figure 5.7(d), (e), and (f) show the $g^{(2)}(0)$ curves with the lowest pumping rates, replicated from panels (a), (b), and (c) (left axis), and their corresponding total photon number of the output pulses (right axis) as a function of the pump pulse width. Note that the $g^{(2)}(0)$ curves in Figure 5.7(d) and (e) traverse from a superthermal $(g^{(2)}(0) > 2)$ to a subthermal $(g^{(2)}(0) < 2)$ region as pumping pulse width increases. For the pulses with the same width (for example, comparing the pulses in (d) and (e) where $g^{(2)}(0) = 2$ and pulse width is 0.4), lasers with a lower β can emit more energy per pulse, as indicated by the total photon number detected. This finding suggests that lasers with a near-unity β might not always be the optimal choice for generating high-power superthermal light pulses. However, using macro-lasers with very low β values might also be less suitable, as the superthermal region associated with photon bursts could be considerably narrowed or even vanish [39].
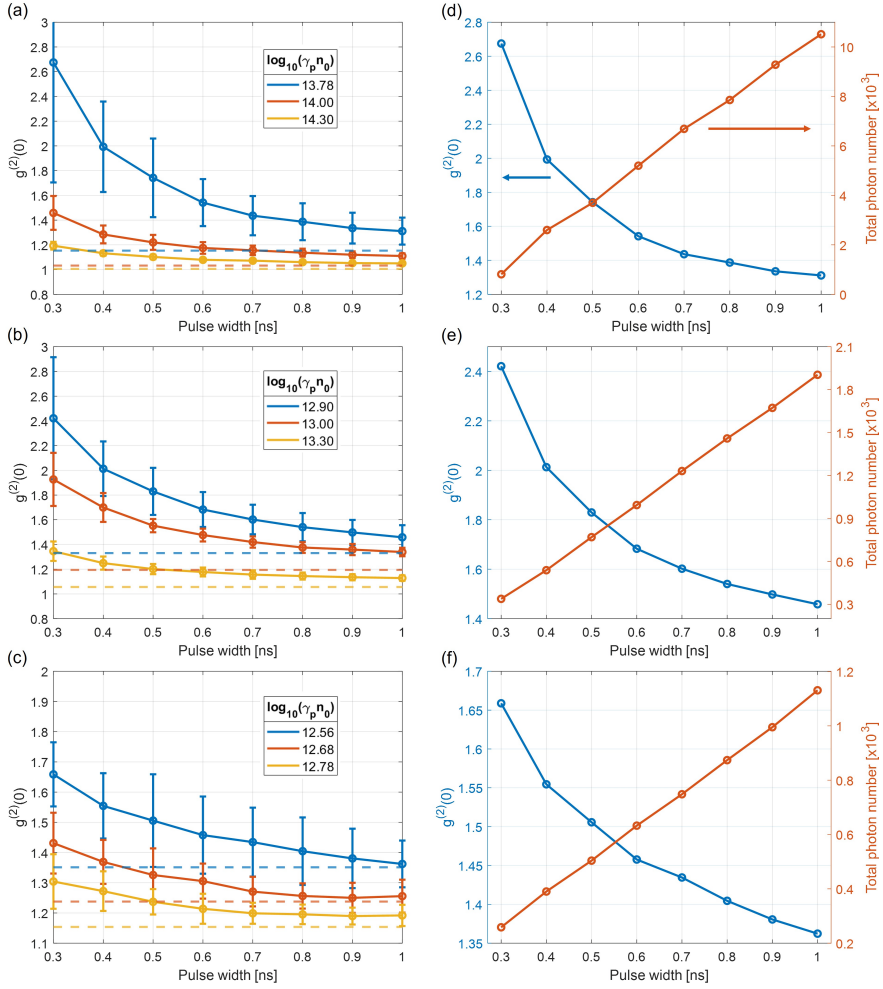
Figure 5.7. Variation of the autocorrelation function $g^{(2)}(0)$ with respect to pumping pulse width at different pumping rates. Panels (a) to (c) show the changes in $g^{(2)}(0)$ for β values of 0.03, 0.3, and 1, respectively. Each data point is the result of an average of 10 trials. Dashed lines indicate the steady-state $g^{(2)}(0)$ under time-invariant pumps. Panels (d), (e), and (f) show the relationship between $g^{(2)}(0)$ (blue lines, left y-axis) and the total photon number for each output pulse (red lines, right y-axis) as a function of pumping pulse width. The $g^{(2)}(0)$ curves correspond to the blue lines in panels (a), (b), and (c), respectively. Here, the product $n_0\beta$ is fixed at 300.

5.3.3 Monitoring spontaneous and stimulated emission photons in stochastic simulations

Near the lasing threshold, there is a notable transition from the dominance of spontaneous emission photons to stimulated emission photons. To gain a deeper understanding of this transition, it would be beneficial to monitor both spontaneous and stimulated emission photons simultaneously. The previously discussed stochastic simulation model can track only the total photon number n_p, as characterized by the "one-pool model." However, to concurrently monitor the spontaneous emission photon number $n_{p,sp}$, and stimulated emission photon number $n_{p,st}$, a "two-pool model" can be constructed by creating two separate reservoirs for spontaneous and stimulated emission photons. This modification involves not just the spontaneous and stimulated emission events but also re-absorption and cavity loss events, both of which also affect photon numbers. The average rates for re-absorption and cavity loss can be split to operate on the two separate reservoirs, spontaneous and stimulated emission, as follows:

$$a_{ra,sp(st)} = \gamma_r(n_0 - n_e)n_{p,sp(st)}$$
$$a_{c,sp(st)} = \gamma_c n_{p,sp(st)} \tag{5.11}$$

Using FRM as an example, the iterative equations for this two-pool model are formulated as follows:

$$n_{p,sp,i+1} = n_{p,sp,i} \begin{cases} +1 & x = sp \\ -1 & x = c_{sp}, ra_{sp} \end{cases}$$
$$n_{p,st,i+1} = n_{p,st,i} \begin{cases} +1 & x = st \\ -1 & x = c_{st}, ra_{st} \end{cases} \tag{5.12}$$

and the total photon number is $n_{p,i} = n_{p,sp,i} + n_{p,st,i}$.

Figure 5.8(a) shows the temporal evolution of n_e, $n_{p,sp}$, and $n_{p,st}$ using the two-pool model for a laser with a $\beta = 0.03$. Note that this evolution pattern differs from that generated by the one-pool model, as shown in Figure 5.8(b), even when the same seed for the random number generator is used. This observation raises a consideration: the act of splitting the photon reservoir into two pools might inadvertently introduce non-physical effects, especially considering that photons, according to quantum theory, are indistinguishable. However, further analyses, as presented in Figure 5.9, reveal that both the average photon number $\langle n_p \rangle$ and the variation of $g^{(2)}(0)$ as functions of the pumping rate exhibit remarkable similarities between the two models. This resemblance is evident for $\beta = 0.03$ (Figure 5.9(a) and (c)) and $\beta = 0.3$ (Figure 5.9(b) and (d)) in the near-threshold region. Additionally, higher-order statistical measures such as variance, skewness, and kurtosis also closely align in both models (see Appendix E), thereby confirming the capability of the two-pool model to generate reliable simulation outcomes comparable to the one-pool model.
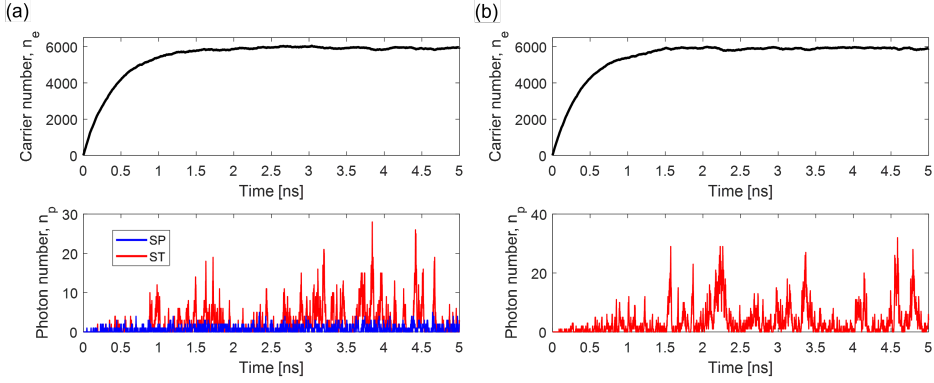
Figure 5.8. Temporal evolution of the carrier number n_e and photon number n_p for a laser characterized by $\beta = 0.03$. Comparisons are drawn between (a) the two-pool model and (b) the one-pool model. In (a), the blue and red lines denote the stimulated and spontaneous emission photon numbers, respectively, while in (b), the red line denotes the total photon number. Here, the product $n_0\beta$ is fixed at 300. An identical random number generator seed is used for both simulations.

5.3.4 Comparative analysis: FTI vs. FRM in the near-threshold region

As discussed in Subsection 5.2.3, FTI introduces deviations from the Poisson process, prompting interest in investigating its influence on statistical quantities. By comparing simulation results with analytical solutions, we can gain insights into these deviations. Analytically, the average photon number $\langle n_p \rangle$ can be derived from the steady-state solution of Equations 5.3 and 5.2, and the autocorrelation function $g^{(2)}(0)$ is related to $\langle n_p \rangle$ and its variance $\langle \delta n_p{}^2 \rangle$ as in Equation 5.10. The variance, derived from the rate equations with Langevin noise, is given by [52]:

$$\langle \delta n_p^2 \rangle = \frac{1}{\Gamma} \left[\left(1 + \frac{\Gamma_{ee}^2}{\omega_R^2} \right) D_{pp} + \frac{\Gamma_{pe}^2}{\omega_R^2} D_{ee} + \frac{2\Gamma_{pe}\Gamma_{ee}}{\omega_R^2} D_{pe} \right] \tag{5.13}$$

where [124]

$$
\begin{aligned}
2D_{pp} &= \gamma_c \langle n_p \rangle + \gamma_r \langle n_e \rangle + \gamma_r n_0 \langle n_p \rangle \\
2D_{pe} &= -\gamma_r n_0 \langle n_p \rangle - \gamma_r \langle n_e \rangle \\
2D_{ee} &= \gamma_p \left(n_0 - \langle n_e \rangle \right) + \gamma_t \langle n_e \rangle + \gamma_r n_0 \langle n_p \rangle
\end{aligned}
\tag{5.14}
$$
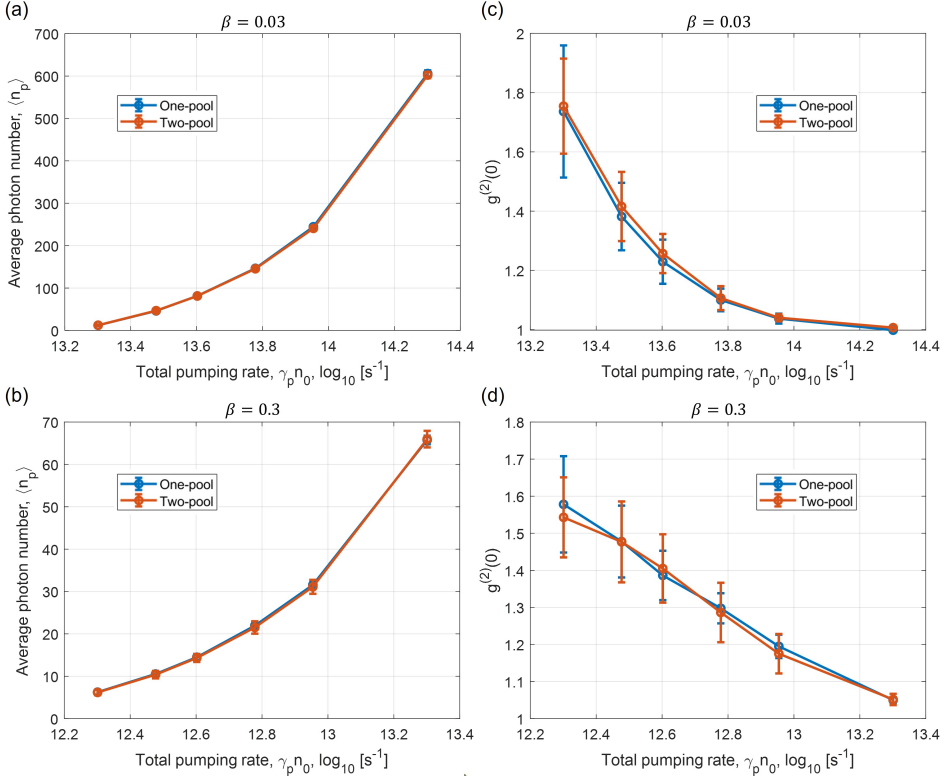
Figure 5.9. Comparative analysis of the one-pool (blue lines) and the two-pool (red lines) models. (a) and (b) show the dependence of the average photon number $\langle n_p \rangle$ on the total pumping rate for $\beta = 0.03$ and 0.3, respectively. (c) and (d) show the dependence of the average photon number $g^{(2)}(0)$ on the total pumping rate for $\beta = 0.03$ and 0.3, respectively. Here, the product $n_0\beta$ is fixed at 300. Each data point is the result of an average of 30 trials.

and

$$
\begin{aligned}
\Gamma_{ee} &= \gamma_p + \gamma_t + 2\gamma_r \langle n_p \rangle \\
\Gamma_{ep} &= \gamma_r \left(2 \langle n_e \rangle - n_0 \right) \\
\Gamma_{pe} &= \gamma_r \left(2 \langle n_p \rangle + 1 \right) \\
\Gamma_{pp} &= \gamma_c - \gamma_r \left(2 \langle n_e \rangle - n_0 \right) \\
\Gamma &= \Gamma_{ee} + \Gamma_{pp} \\
\omega_R^2 &= \Gamma_{ee}\Gamma_{pp} + \Gamma_{pe}\Gamma_{ep}
\end{aligned}
\tag{5.15}
$$

Figure 5.10 compares the relative deviations in photon number $\Delta\langle n_p \rangle / \langle n_p \rangle$ (Figure 5.10(a)) and deviations in autocorrelation function $\Delta g^{(2)}(0)$ (Figure 5.10(b)) between

analytical and simulation results for both FTI and FRM algorithms, plotted against the pumping rate. For FTI, the time interval condition is set to ensure $P(X \leq 1) > 99\%$.

In the observed results, FRM exhibits larger photon number deviations than FTI, particularly at low pumping rates and higher β. In this regime, noisy spikes are present when average photon numbers are near zero. The assumption that Langevin noise is symmetrically distributed about the average value is less valid when the photon number approaches zero. FRM algorithm considers only one event per iteration. When photon or carrier numbers reach zero in a given step, the algorithm excludes any subsequent event that could further decrease these numbers in the next step. Conversely, the FTI algorithm mixes the effects of all events within a single time step. This approach allows for the occurrence of events in larger numbers than the photon or carrier numbers, potentially resulting in photon or carrier numbers falling below zero. For instance, if the photon number $n_p(t)$ is one at time t, the cavity-loss event could occur twice during the period dt due to its non-zero average rate. Although the photon number after this iteration step, $n_p(t + dt)$, cannot be negative, the cavity-loss event can cancel out the effects of, for example, stimulated emission, resulting in a smaller increase in the photon number. Therefore, FTI is closer to the analytical model assumption that Langevin noise can be both positive and negative, even when the average value is near zero. As seen from Figure 5.10, the discrepancy between the results from the FRM and analytical solutions diminishes as the pumping rate increases due to the average photon numbers moving away from zero. Further evidence of this trend is provided in Figure 5.11, which shows the fraction of time in which n_p exceeds its average $\langle n_p \rangle$ during the whole simulated time for $\beta = 1$. The data shows that in FTI simulation, the fraction approaches closer to 50% compared to FRM under the same pumping rate, suggesting a more balanced probability of the photon number being either above or below its average. As the pumping intensifies, both methods exhibit a trend of converging toward 50%, owing to the decreased probability of the photon number reaching zero. The autocorrelation function $\Delta g^{(2)}(0)$ also shows convergence towards the analytical solutions (where $\Delta g^{(2)}(0) = 0$) as the pumping rate increases for both methods. It is observed that FRM yields negative deviations of $g^{(2)}(0)$ from the analytical model, especially at low pumping rates. This trend can be understood by Equation 5.10, which indicates that a larger average photon number results in a lower $g^{(2)}(0)$. In FRM, as shown in Figure 5.10(a), there are notable positive deviations in $\langle n_p \rangle$ at low pumping rates. This positive deviation of photon number subsequently results in the negative deviation of $g^{(2)}(0)$. As observed, in the near-threshold region characterized by large relative fluctuations in photon number and an average photon number nearing zero, there are notable deviations in the average photon number, $\langle n_p \rangle$, and $g^{(2)}(0)$ when comparing the analytical model and FTI with the more realistic FRM simulation. These discrepancies are especially pronounced in high β lasers with an extended lasing transition region.
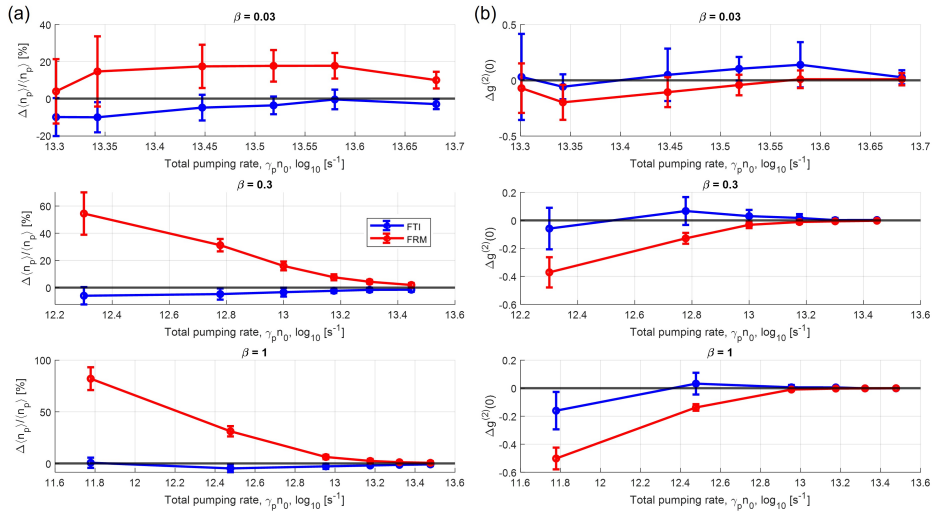
Figure 5.10. Comparison between stochastic simulation and analytical solutions for (a) the relative deviation in photon number $\Delta\langle n_p\rangle/\langle n_p\rangle$, and (b) the deviations in the autocorrelation function $\Delta g^{(2)}(0)$. The blue lines represent the results from FTI, while the red lines represent the results from FRM. The black lines mark the zero deviation point, perfectly matching the analytical solutions. The results are organized according to different β values, with 0.03 in the upper row, 0.3 in the middle row, and 1 in the lower row. Here, the product $n_0\beta$ is fixed at 300. Each data point for FRM is averaged over 30 trials. For FTI, each point is averaged over 10 trials due to longer computational time, using a time increment of $dt = 8 \times 10^{-15}$ s.
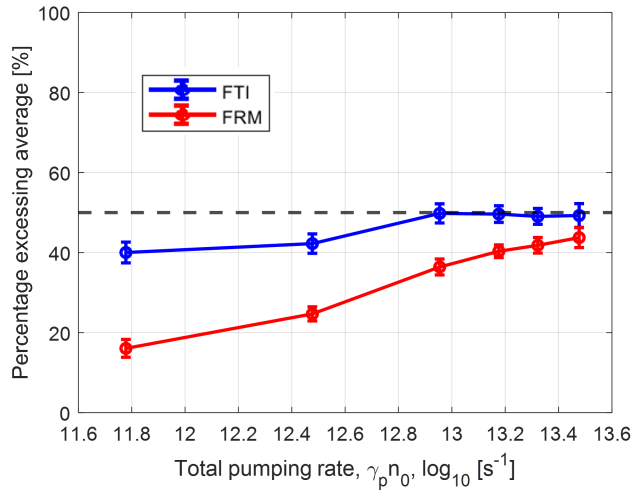
Figure 5.11. Percentage of the signal exceeding its average value for $\beta = 1$. The blue line shows the results from FTI, and the red line shows the results from FRM. The black dashed line at 50% indicates an equal distribution of the photon number above and below its average value.

CHAPTER 6

Conclusion

This thesis represents an exploration of the dynamics and applications of photonic crystal Fano lasers, advancing the understanding through theoretical and experimental investigations. Key highlights include the experimental demonstration of energy-efficient pulse generation in Fano lasers, as well as the development of a mathematical model and a refined simulation algorithm for Fano lasers with feedback. The research presented here opens up a route for future innovations in laser technology.

In Chapter 2, we develop an algorithm for simulating Fano lasers. This algorithm divides the laser cavity into multiple sections, allowing for taking the carrier diffusion into account and enhancing the temporal resolution of the field evolution. We investigate the relationship between the number of sections and the pumping rate for maintaining numerical stability. The convergence of laser variables with increasing section numbers and the deviation from steady-state oscillation conditions solutions due to non-uniform carrier distribution is analyzed. The comparison of our new multi-section approach with previous analytical solutions assuming uniform carrier distribution reveals a notable discrepancy, which indicates the deviation of previous calculations from realistic cases. Additionally, we conduct a comparative analysis of laser dynamics during relaxation oscillations, employing various numerical simulation approaches. This study offers a more precise tool for simulating the behavior of Fano lasers. While more realistic models such as logarithm gain dependence on carrier density in quantum well lasers and pumping saturation can be considered [52], this simple model still offers valuable insights into the dynamics of Fano lasers.

In Chapter 3, our research delved into nanocavity refractive index tuning methods, particularly focusing on the free carrier effect and the thermal effect on Fano lasers. Q-switching and cavity-dumping mechanisms explain the pulse generation observed during nanocavity frequency tuning. The experimental results, demonstrating similar pulse shapes to the simulation predictions, validate our theoretical model and highlight the energy efficiency of pulse generation in Fano lasers compared to equivalently sized Fabry-Pérot lasers. Although the modulation in this study is achieved through an external ultra-short pulse laser, the potential for electrical modulation of nanocavities is promising. This advancement could pave the way for compact, integrable, and modulable on-chip Fano lasers in the future.

Chapter 4 proposes a novel Fano laser configuration with an active feedback cavity. Unlike previous weak feedback systems, where the feedback field only slightly perturbs the dominant lasing mode, this device exhibits various modes arising from

the interplay between the original Fano laser and the external cavity. The coexistence of Fano and Fabry-Pérot modes under specific nanocavity detuning and bistability is observed, opening up possibilities for creating compact, energy-efficient flip-flop devices using feedback Fano lasers. The analytical comparison between nanolasers with two coupled cavities and our waveguide-nanocavity systems reveals our system's stability, avoiding the mode oscillations observed in two coupled nanocavities lasers. Experimental characterization of a sample with a feedback Fano laser structure was conducted. However, this prototype sample did not observe bistability as predicted in our model. This may be because the sample was designed and fabricated before the theoretical model was developed. Therefore, the sample does not meet the specific conditions our model predicts as necessary for achieving bistability. Looking forward, we are optimistic that newly designed samples, more closely adhering to the theoretical guidelines, will successfully demonstrate the bistability properties.

Chapter 5 shifts focus to the stochastic simulation of nanolasers, going beyond the semi-classical approach used in previous chapters. This research aims to catch up with the future development of nanolasers towards lower power and fewer emitters. We revisit two stochastic approaches, the fixed time increment method and Gillespie's first reaction method, to examine their characteristics and computational efficiency. A key area of focus is the behavior of nanolasers in near-threshold regions. In this region, our simulations successfully capture the photon burst phenomenon previously observed in quantum well lasers [39]. This phenomenon is reproduced in our simulations using quantum dot laser configuration, considering effects such as photon recycling and pumping block effects. The statistical properties observed in the simulations reveal deviations from analytical solutions in the near-threshold regions, which are attributed to the photon bursts causing large fluctuations in photon and carrier numbers. Moreover, we investigate the photon statistical properties of pulses generated through gain tuning near the threshold. This study might shed light on ultra-low power pulse generation, potentially paving the way for advancements in energy-efficient optical communication technologies.

Appendices

Derivation of feedback Fano laser oscillation condition

To determine the lasing mode frequencies and threshold carrier densities of a feedback Fano laser, we calculate the pole of the scattering matrix (S-matrix), $\mathbf{S}$, which corresponds to the threshold for lasing [52]. The pole can be determined by identifying the root of the denominator of the S-matrix elements. The S-matrix can be expressed in terms of the transmission matrix (T-matrix), $\mathbf{T}$, as follows [52]:

$$\mathbf{S} = \frac{1}{T_{11}} \begin{bmatrix} T_{21} & det\mathbf{T} \\ 1 & -T_{21} \end{bmatrix} \tag{A.1}$$

Equation A.1 shows that all elements of the S-matrix share a common denominator, T_{11}. The overall T-matrix of the feedback Fano laser, $\mathbf{T}_{tot}$, is obtained by sequentially multiplying the matrices in Equation 4.3 as $\mathbf{T}_{LM}\mathbf{T}_{LWG}\mathbf{T}_F\mathbf{T}_{RWG}\mathbf{T}_{RM}$. Consequently, we can express T_{11} as:

$$T_{11} = \frac{e^{-i(k(\omega,N)L_1 + k(\omega,N)L_2)}}{t_F(\omega)t_L t_R} \left(\begin{array}{c} 1 - e^{2ik(\omega,N)L_1}r_F(\omega)r_L - e^{2ik(\omega,N)L_2}r_F(\omega)r_R \\ +e^{2i(k(\omega,N)L_1 + k(\omega,N)L_2)}r_L r_R\left(r_F^2(\omega) - t_F^2(\omega)\right) \end{array} \right) \tag{A.2}$$

To find the poles of the S-matrix, we set the numerator of T_{11} to zero, resulting in the following equation:

$$\begin{array}{c} e^{2ik(\omega,N)L_1}r_L r_F(\omega) + e^{2ik(\omega,N)L_2}r_R r_F(\omega) \\ +e^{2ik(\omega,N)(L_1+L_2)}r_L r_R t_F^2(\omega) - e^{2ik(\omega,N)(L_1+L_2)}r_L r_R r_F^2(\omega) = 1 \end{array} \tag{A.3}$$

This derivation leads to Equation 4.5 in the main text, which defines the lasing oscillation condition for a feedback Fano laser.

Derivation of the composite Fano mirror

The lasing condition for the LHS-Fano mode can be alternatively seen as the condition for the field circulating without loss in a cavity composed of the LHS mirror, with reflection coefficient r_L, and the RHS composite Fano mirror, with reflection coefficient r_{CMR}:

$$r_L r_{CMR}(\omega, N) e^{2ik(\omega, N)L_1} = 1 \tag{B.1}$$

The RHS composite Fano mirror is composed of the Fano mirror, the RHS WG, and the RHS mirror. Its reflection coefficient can be calculated using the T-matrix. The overall T-matrix of the RHS composite Fano mirror, $\mathbf{T}_{CMR}$, is given by:

$$\mathbf{T}_{CMR} = \mathbf{T}_F \mathbf{T}_{RWG} \mathbf{T}_{RM} = \frac{e^{ik(\omega, N)L_2}}{t_F(\omega)\, t_R} \left[\begin{array}{cc} T_{CMR,11} & T_{CMR,12} \\ T_{CMR,21} & T_{CMR,22} \end{array} \right] \tag{B.2}$$

where the elements are defined as:

$$
\begin{aligned}
T_{CMR,11} &= 1 - e^{2ik(\omega,N)L_2} r_F(\omega)\, r_R \\
T_{CMR,12} &= -e^{2ik(\omega,N)L_2} r_F(\omega) + r_R \\
T_{CMR,21} &= r_F(\omega) + e^{2ik(\omega,N)L_2} r_R \left(t_F^2(\omega) - r_F^2(\omega) \right) \\
T_{CMR,22} &= r_F(\omega)\, r_R + e^{2ik(\omega,N)L_2} \left(t_F^2(\omega) - r_F^2(\omega) \right)
\end{aligned}
\tag{B.3}
$$

Consequently, the RHS composite Fano mirror reflection coefficient r_{CMR} can be obtained by:

$$r_{CMR} = \frac{T_{CMR,21}}{T_{CMR,11}} = r_F(\omega) + \frac{r_R t_F^2(\omega) e^{2ik(\omega,N)L_2}}{1 - r_R r_F(\omega) e^{2ik(\omega,N)L_2}} \tag{B.4}$$

which leads to Equation 4.6 in the main text.

Stability investigation of modes in feedback Fano lasers

The stability of each mode in a feedback Fano laser can be numerically evaluated by observing the time evolution from its steady state. Utilizing the lasing oscillation condition (Equation 4.5), we can calculate the spatial distribution of the field amplitude for each mode based on their mode frequency and threshold carrier density. This distribution is subsequently used as the initial condition for the dynamic evolution equations of the laser to examine mode stability.

First, we consider the carrier density rate equation at steady state (assuming uniform carrier density without diffusion):

$$R_p - \frac{N_s}{\tau_c} - \frac{\Gamma v_g g_n \left(\sigma_{nl} \left(\omega_s, N_s \right) |S_{nl}^-|^2 + \sigma_{nr} \left(\omega_s, N_s \right) |S_{nr}^-|^2 \right)}{A \left(L_1 + L_2 \right)} \left(N_s - N_0 \right) = 0 \quad \text{(C.1)}$$

Here, ω_s and N_s are the steady state mode frequency and threshold carrier density for each mode derived from Equation 4.5. The parameter $\sigma_{nl(nr)}(\omega_s, N_s)$ is the photon number-intensity parameter (ratio of total photon number to intensity) with respect to $S_{nl(nr)}^-$, which can be derived as follows [56]:

$$\sigma_{nl}(\omega_s, N_s) = \frac{I \left(t \right)}{\left| S_{nl}^-(t) \right|^2} = \frac{\sigma_0 \int_0^{L_1} \left| S^+(z,t) + S^-(z,t) \right|^2 dz}{\left| S_{nl}^-(t) \right|^2} \quad \text{(C.2)}$$

Here, $\sigma_0 = 2\epsilon_0 n n_g / (\hbar \omega_s)$, and $I(t)$ is the total photon number within the WG. The terms $S^{+(-)}(z,t)$ are the complex amplitude of the field propagating forward (backward) toward the NC, dependent on spatial coordinate z along the WG. Setting $z = 0$ at the point beneath the NC, we then have the relation:

$$S^\pm \left(z, t \right) = S_{nl}^\pm (t) e^{\pm ik(\omega, N)z} \quad \text{(C.3)}$$

and

$$S_{nl}^-(t) = r_{CMR} S_{nl}^+(t) \quad \text{(C.4)}$$

Substituting Equation C.3 and C.4 into C.2, we get:

$$\sigma_{nl}(\omega_s, N_s) = \sigma_0 \int_0^{L_1} \left(\left| \frac{1}{r_{CMR}} e^{ik(\omega_s, N_s)z} + e^{-ik(\omega_s, N_s)z} \right|^2 \right) dz$$

$$= \sigma_0 \left(\frac{e^{2G(N_s)L_1} - 1}{2G(N_s)} + \frac{1 - 2G(N_s)L_1}{2G(N_s)|r_{CMR}|^2} + \frac{i \left(e^{-i2\beta(\omega_s)L_1} - 1 \right)}{2\beta(\omega_s) r_{CMR}} + \frac{i \left(1 - e^{i2\beta(\omega_s)L_1} \right)}{2\beta(\omega_s) r_{CMR}^*} \right) \tag{C.5}$$

where $G(N_s) = \frac{1}{2}(\Gamma g_n(N_s - N_0) - \alpha_i)$ is the imaginary part, and $\beta(\omega_s) = \omega_s n/c$ is the real part (assume linewidth enhancement factor $\alpha = 0$) of the wavenumber $k(\omega_s, N_s)$. The parameter σ_{nr} can be derived in the same way by replacing $S_{nl}^{\pm}$ with $S_{nr}^{\pm}$, L_1 with L_2, and the RHS composite mirror with the LHS composite mirror.

Next, to obtain the relation between $S_{nl}^{\pm}$ and $S_{nr}^{\pm}$, we use the definition of the Fano mirror T-matrix $\mathbf{T}_F$:

$$\begin{bmatrix} S_{nl}^+ \\ S_{nl}^- \end{bmatrix} = \mathbf{T}_F \begin{bmatrix} S_{nr}^- \\ S_{nr}^+ \end{bmatrix} \tag{C.6}$$

By dividing S_{nl}^- on both sides and using the relation $r_{CMR} = S_{nl}^-/S_{nl}^+$, we have:

$$\begin{bmatrix} S_{nr}^-/S_{nl}^- \\ S_{nr}^+/S_{nl}^- \end{bmatrix} = \mathbf{T}_F^{-1} \begin{bmatrix} r_{CMR}^{-1} \\ 1 \end{bmatrix} \tag{C.7}$$

where $\mathbf{T}_F^{-1}$ is the inverse matrix of $\mathbf{T}_F$. The amplitude S_{nr}^- in Equation C.1 can be eliminated and solved to determine S_{nl}^- as a function of ω_s and N_s. The field amplitudes at other sites in the WG, $S_m^{\pm}$, and within the NC, A_c can then be obtained using Equations 4.7 and 4.11.

Using $S_m^{\pm}$, A_c, and N_s as the initial conditions of the multi-section dynamic equations, we can examine the stability of each mode. Figure C.1 shows the temporal evolution of energy inside the NC, E_{NC}, and normalized carrier density, N/N_0, for each mode when NC detuning $\sigma_c = -3$. As seen, the hybrid mode and RHS Fano mode eventually transfer to the LHS-Fano mode, having the same E_{NC} and N values. On the other hand, the FP mode, though exhibiting some oscillation, stabilizes without transitioning to other modes. This result confirms the stability of the LHS-Fano and FP modes.
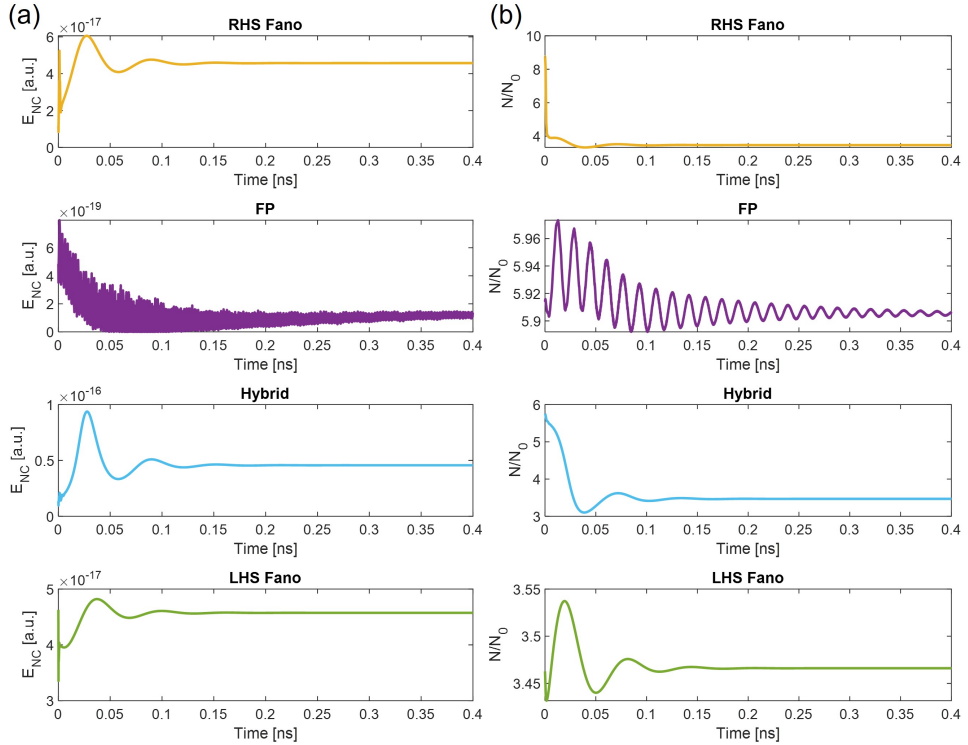
Figure C.1. Evolution of nanocavity (NC) energy and carrier density for various modes in a feedback Fano laser. (a) NC energy E_{NC} and (b) carrier density N are tracked for the RHS Fano mode (yellow lines), FP mode (violet lines), hybrid mode (light blue lines), and LHS-Fano mode (green lines). The simulation is conducted at a pumping rate $R_p = 20R_{th}$ and an NC detuning of $\sigma_c = -3$. The RHS Fano and hybrid modes eventually transfer to the LHS-Fano mode, while the FP mode remains stable.

Detailed derivation of the analytical relation between feedback Fano lasers and nanolasers with two coupled cavities

D.1 Relation between the anti-symmetric mode function and the nanocavity complex amplitude

In Section 4.6 of the main text, we use two variables, $A_{c1}(t)$ and $A_{c2}(t)$, to describe the complex amplitude located in the first and the second nanocavity of a two coupled cavities nanolaser. We then define an anti-symmetric function as:

$$\psi(t)\varphi(r) \equiv A_{c1}(t)\varphi_1(r) - A_{c2}(t)\varphi_2(r) \tag{D.1}$$

with the anti-bonding relation:

$$A_{c1}(t) = -A_{c2}(t) \tag{D.2}$$

Here, $\varphi(r)$ is the space-dependent complex amplitude. Since the $\varphi_1(r)$ and $\varphi_2(r)$ are located in different NCs, we have the non-overlap relation:

$$\int \varphi_1(r)\varphi_2(r)dr = 0 \tag{D.3}$$

and the normalization condition:

$$\int \varphi(r)dr = 1 \tag{D.4}$$

Given these relations, Equation D.1 can be rewritten as:

$$
\begin{aligned}
|\psi(t)|^2 &= |\psi(t)|^2 \int |\varphi(r)|^2 dr \\
&= \int |A_{c1}(t)\varphi_1(r) - A_{c2}(t)\varphi_2(r)|^2 dr \\
&= \int \left(|A_{c1}(t)|^2|\varphi_1(r)|^2 + |A_{c2}(t)|^2|\varphi_2(r)|^2 - A_{c1}(t)\varphi_1(r)A_{c2}{}^*(t)\varphi_2{}^*(r) - C.C. \right) dr \\
&= |A_{c1}(t)|^2 + |A_{c2}(t)|^2 \\
&= 2|A_{c1}(t)|^2 = 2|A_{c2}(t)|^2
\end{aligned}
\tag{D.5}
$$

By subtracting Equations 4.22 with 4.23 and substituting Equation D.5 into them, we derive Equation 4.24 in the main text.

D.2   Derivation of the Jacobian matrix for the FP Mode and the LHS-Fano mode

For the feedback Fano laser, substituting Equations 4.7 and 4.11 into Equation 4.12 and under the assumptions $L_1 = L_2 = L$ and $r_L = -1$, we can simplify and derive the NC field evolution equation dependent only on $A_c(t)$ as presented in Equation 4.25 in the main text:

$$\frac{dA_c(t)}{dt} = -(i\delta(\omega) + \gamma_t) A_c(t) + \gamma_c \left[\frac{i(r_L + r_R)e^{2ik(\omega,N)L} + 2r_L r_R e^{4ik(\omega,N)L}}{1 + r_L r_R e^{4ik(\omega,N)L}} \right] A_c(t) \tag{D.6}$$

We can then linearize Equation D.6 to obtain the perturbation equation around the steady state mode frequency ω_s and carrier density N_s:

$$
\begin{aligned}
\frac{d\Delta A_c(t)}{dt} =& \left[\frac{\gamma_c 2|r_R|e^{4ik_s L} - i\gamma_c(1 + |r_R|)e^{2ik_s L}}{1 + |r_R|e^{4ik_s L}} - (i\delta(\omega) + \gamma_t) \right] \Delta A_c(t) \\
&+ \left[\frac{-\gamma_c 2GL|A_s|e^{2ik_s L}i(1 + |r_R| + 4i|r_R|e^{2ik_s L} - |r_R|e^{4ik_s L} - |r_R|^2 e^{4ik_s L})}{(1 + |r_R|e^{4ik_s L})^2} \right] \Delta N(t)
\end{aligned}
\tag{D.7}
$$

Here, $k_s = k(\omega_s, N_s)$ and A_s are the wavenumber and the NC field amplitude at steady state, respectively.

For the LHS-Fano mode at steady state, $\delta(\omega_s)$ is close to zero and $r_F(\omega_s) \approx i$. Then, according to the oscillation condition $r_L r_F(\omega_s) \exp(2ik_sL) = 1$, we derive:

$$\exp\left(2ik_sL\right) \approx i \tag{D.8}$$

and

$$\exp\left(4ik_sL\right) \approx -1 \tag{D.9}$$

Substituting Equations D.8 and D.9 into D.7, we obtain:

$$\frac{d\Delta A_c\left(t\right)}{dt} = (\gamma_c - \gamma_t)\Delta A_c\left(t\right) + 2GL|A_s|\gamma_c\Delta N(t) \tag{D.10}$$

which is Equation 4.26 in the main text.

The rate equation for carriers in the WG can be expressed as:

$$\frac{dN(t)}{dt} = R_p - \frac{N(t)}{\tau_c} - \left(g'_{nl}|S_{nl}^-(t)|^2 + g'_{nr}|S_{nr}^-(t)|^2\right)(N(t) - N_0) \tag{D.11}$$

where g'_{nl} and g'_{nr} are the gain coefficients associated with S_{nl}^- and S_{nr}^-, respectively. Assuming that the round-trip time in the system is much shorter than the timescales for variations in the field and carrier density, we can utilize Equation 4.11:

$$S_{nl(nr)}^- = -iS_{nr(nl)}^+ + \sqrt{\gamma_c}A_c \tag{D.12}$$

and Equation 4.7 for $S_{nl(nr)}$ at steady state:

$$\begin{aligned} S_{nl}^+ &= S_{nl}^- r_L e^{2ik_sL} \\ S_{nr}^+ &= S_{nr}^- r_R e^{2ik_sL} \end{aligned} \tag{D.13}$$

to obtain the equation depends solely on S_{nl}^- and A_c:

$$S_{nl}^- = \frac{1 - ir_R e^{2ik_sL}}{1 + r_L r_R e^{4ik_sL}}\sqrt{\gamma_c}A_c = \frac{1 + i|r_R|e^{2ik_sL}}{1 + |r_R|e^{4ik_sL}}\sqrt{\gamma_c}A_c \tag{D.14}$$

and the equation depends solely on S_{nr}^- and A_c:

$$S_{nr}^- = \frac{1 - ir_L e^{2ik_sL}}{1 + r_L r_R e^{4ik_sL}}\sqrt{\gamma_c}A_c = \frac{1 + ie^{2ik_sL}}{1 + |r_R|e^{4ik_sL}}\sqrt{\gamma_c}A_c \tag{D.15}$$

By substituting Equations D.14 and D.15 into Equation D.11 and using the Equations D.8 and D.9, Equation D.11 becomes:

$$\frac{dN(t)}{dt} = R_p - \frac{N(t)}{\tau_c} - g'_{nl}(N(t) - N_0)\gamma_c|A_c|^2 \tag{D.16}$$

We can similarly linearize the carrier rate equation D.16:

$$\frac{d\Delta N(t)}{dt} = -\frac{\Delta N(t)}{\tau_c} - 2g'_{nl}\gamma_c|A_s|(N_s - N_0)\Delta A_c(t) - g'_{nl}\gamma_c|A_s|^2\Delta N(t) \tag{D.17}$$

For the LHS-Fano mode at steady state, $N_s \approx N_0$, Equation D.17 simplifies to:

$$\frac{d\Delta N(t)}{dt} = -\frac{\Delta N(t)}{\tau_c} - g'_{nl}\gamma_c|A_s|^2\Delta N(t) \tag{D.18}$$

which is Equation 4.27 in the main text.

For the FP mode at the steady state, the lasing condition becomes:

$$r_L r_R t_F{}^2(\omega_s)\exp\left(4ik_sL\right) = 1 \tag{D.19}$$

Incorporating the Fano mirror transmission from Equation 2.10 and taking the square root yields:

$$\sqrt{|r_R|}(\frac{\delta(\omega) - i\gamma_v}{i\delta(\omega_s) + \gamma_t})e^{2ik_sL} = \pm 1 \tag{D.20}$$

Given that $\exp(2ik_sL)$ must achieve value i when $\delta(\omega_s) \to 0$ for the Fano mode (see Equation D.8), only the positive solution is physically valid. We then have (assume $\gamma_v \approx 0$):

$$e^{2ik_sL} = \frac{1}{\sqrt{|r_R|}}(i + \frac{\gamma_t}{\delta(\omega_s)}) \tag{D.21}$$

In the FP mode, the mode frequency detunes from the NC frequency by several linewidths, γ_t. We can assume $\gamma_t^2/\delta^2(\omega_s) \ll 1$, leading to:

$$e^{4ik_sL} \approx \frac{1}{|r_R|}(-1 + i\frac{2\gamma_t}{\delta(\omega_s)}) \tag{D.22}$$

Substituting Equations D.21 and D.22 into Equation D.7, we derive:

$$\begin{aligned}
\frac{d\Delta A_c(t)}{dt} &= \left[(2 - \zeta_1)\gamma_c - \gamma_t - i\left((\zeta_1 - 1)\frac{\gamma_c\delta(\omega_s)}{\gamma_t} + \delta(\omega_s)\right)\right]\Delta A_c(t) \\
&+ \left[2|A_s|GL(\zeta_1 - 1)\frac{\gamma_c\left(\gamma_t{}^2 - \delta^2(\omega_s)\right)}{\gamma_t{}^2} - i4|A_s|GL(\zeta_1 - 1)\frac{\gamma_c\delta(\omega_s)}{\gamma_t}\right]\Delta N(t)
\end{aligned} \tag{D.23}$$

With $\gamma_c \approx \gamma_t$ in a low loss NC, Equation D.23 simplifies further as:

$$\begin{aligned}
\frac{d\Delta A_c(t)}{dt} &= \left[-(\zeta_1 - 1)\gamma_t - i\zeta_1\delta(\omega_s)\right]\Delta A_c(t) \\
&+ \left[-2|A_s|GL(\zeta_1 - 1)\frac{\delta^2(\omega_s)}{\gamma_t} - i4|A_s|GL(\zeta_1 - 1)\delta(\omega_s)\right]\Delta N(t)
\end{aligned} \tag{D.24}$$

where $\zeta_1 = (1 + |r_R|)/(2\sqrt{|r_R|})$.

Substitute Equations D.21 and D.22 into Equation D.14, we obtain:

$$S_{nl}^- = \frac{1 - \sqrt{|r_R|} + i\sqrt{|r_R|}\frac{\gamma_t}{\delta(\omega_s)}}{i\frac{2\gamma_t}{\delta(\omega_s)}}\sqrt{\gamma_c}A_c \tag{D.25}$$

and therefore

$$
\begin{aligned}
|S_{nl}^{-}|^2 &= \left(\frac{1}{4} \frac{\delta^2(\omega_s)}{\gamma_t{}^2} (1 - \sqrt{|r_R|})^2 + |r_R| \right) \gamma_c |A_c|^2 \\
&= \left(\frac{1}{2} \frac{\delta^2(\omega_s)}{\gamma_t{}^2} \sqrt{|r_R|}(\zeta_1 - 1) + |r_R| \right) \gamma_c |A_c|^2
\end{aligned}
\tag{D.26}
$$

Also, for the Equation D.15:

$$
S_{nr}^{-} = \frac{1 - \frac{1}{\sqrt{|r_R|}} + i \frac{1}{\sqrt{|r_R|}} \frac{\gamma_t}{\delta(\omega_s)}}{i \frac{2\gamma_t}{\delta(\omega_s)}} \sqrt{\gamma_c} A_c
\tag{D.27}
$$

and therefore

$$
\begin{aligned}
|S_{nr}^{-}|^2 &= \left(\frac{1}{4} \frac{\delta^2(\omega_s)}{\gamma_t{}^2} (1 - \frac{1}{\sqrt{|r_R|}})^2 + \frac{1}{|r_R|} \right) \gamma_c |A_c|^2 \\
&= \left(\frac{1}{2} \frac{\delta^2(\omega_s)}{\gamma_t{}^2} \frac{1}{\sqrt{|r_R|}}(\zeta_1 - 1) + \frac{1}{|r_R|} \right) \gamma_c |A_c|^2
\end{aligned}
\tag{D.28}
$$

Using Equation D.26 and D.28, the linearized carrier rate equation becomes:

$$
\frac{d\Delta N(t)}{dt} = -\frac{\Delta N(t)}{\tau_c} - 2\kappa\gamma_c |A_s|(N_s - N_0)\Delta A_c(t) - \kappa\gamma_c |A_s|^2 \Delta N(t)
\tag{D.29}
$$

with the coefficient κ:

$$
\kappa = g_{nl}{}' \left(\frac{1}{2} \frac{\delta^2(\omega_s)}{\gamma_t{}^2} \sqrt{|r_R|}(\zeta_1 - 1) + |r_R| \right) + g_{nr}{}' \left(\frac{1}{2} \frac{\delta^2(\omega_s)}{\gamma_t{}^2} \frac{1}{\sqrt{|r_R|}}(\zeta_1 - 1) + \frac{1}{|r_R|} \right)
\tag{D.30}
$$

Combined with the Equation D.24, we can construct the Jacobian matrix for the real part component:

$$
J_{FP} = \begin{pmatrix} -(\zeta_1 - 1)\gamma_t & -2|A_s|GL(\zeta_1 - 1)\frac{\delta^2(\omega_s)}{\gamma_t} \\ -2\kappa\gamma_c|A_s|(N_s - N_0) & -(\frac{1}{\tau_c} + \kappa\gamma_c|A_s|^2) \end{pmatrix}
\tag{D.31}
$$

which is Equation 4.31 in the main text.

Comparison between one-pool and two-pool stochastic models

This chapter shows the additional results of the comparison between the one-pool and two-pool stochastic models discussed in Subsection 5.3.3. We examine the higher-order statistical quantities such as variance, skewness, and kurtosis of the photon number probability distribution function (PDF). Skewness is the third order of the standardized moment, measuring the asymmetry of the PDF [139], and kurtosis is the fourth order of the standardized moment, measuring how often the outliers occur in the distribution [139]. These additional analyses are presented in Figure E.1.

The results demonstrate that besides the average photon number and the auto-correlation function discussed in the main text, higher-order statistical quantities as functions of the pumping rate also reveal similarities between the two models. This observation suggests that the two-pool model can have a high resemblance in photon statistics to the one-pool model.

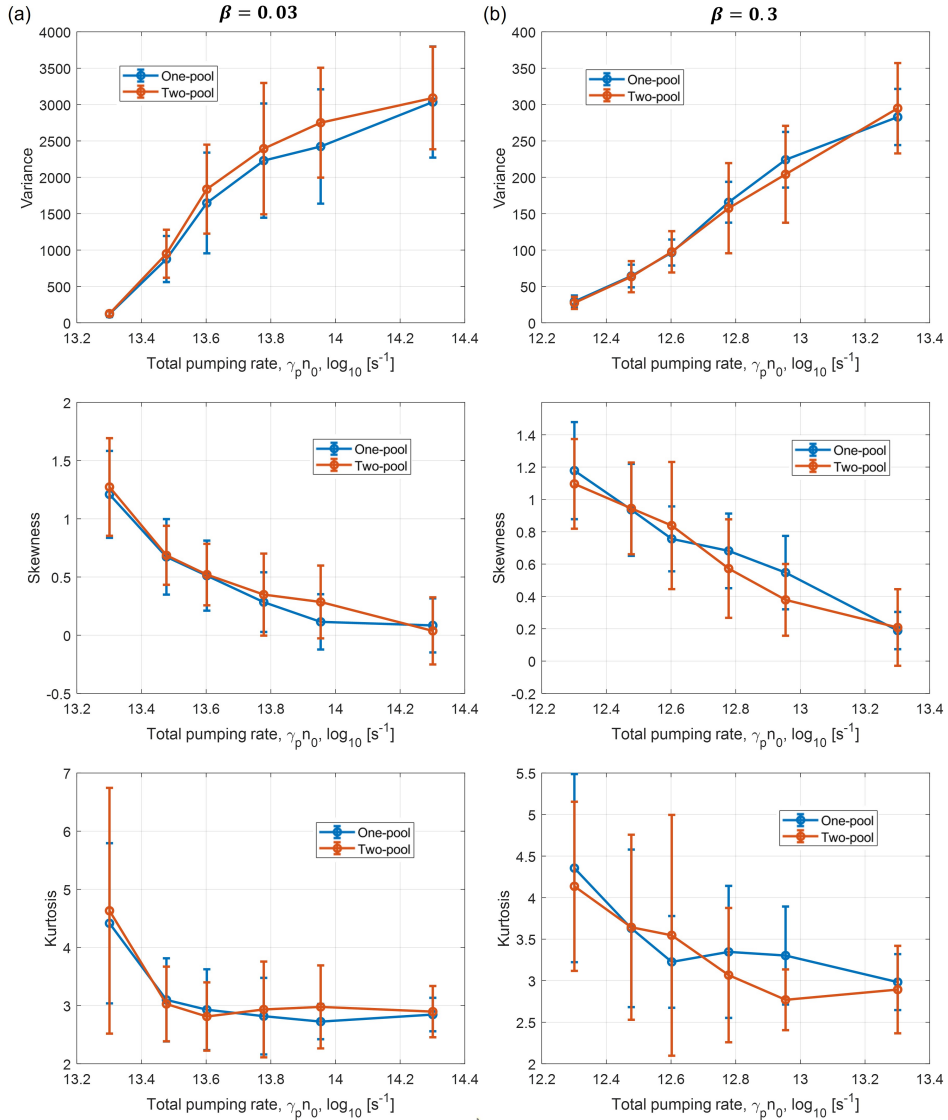**Figure E.1.** Comparative analysis of the one-pool (blue lines) and two-pool (red lines) models in terms of higher-order statistical quantities. (a) and (b) show the cases for $\beta = 0.03$, and $\beta = 0.3$, respectively. The top panels show variance, the middle panels show skewness, and the bottom panels show kurtosis. Here, the product $n_0\beta$ is fixed at 300. Each data point is the result of an average of 30 trials.

Bibliography

[1] J. He, R. A. Norwood, M. Brandt-Pearce, I. B. Djordjevic, M. Cvijetic, S. Subramaniam, R. Himmelhuber, C. Reynolds, P. Blanche, B. Lynn, and N. Peyghambarian, "A survey on recent advances in optical communications," *Computers Electrical Engineering*, vol. 40, no. 1, pp. 216–240, 2014. 40th-year commemorative issue.

[2] F. S. Ujager, S. M. H. Zaidi, and U. Younis, "A review of semiconductor lasers for optical communications," in *7th International Symposium on High-capacity Optical Networks and Enabling Technologies*, pp. 107–111, 2010.

[3] N. Jones, "How to stop data centres from gobbling up the world's electricity," *Nature*, vol. 561, no. 7722, pp. 163–166, 2018.

[4] S. Matsuo, K. Takeda, T. Sato, M. Notomi, A. Shinya, K. Nozaki, H. Taniyama, K. Hasebe, and T. Kakitsuka, "Room-temperature continuous-wave operation of lateral current injection wavelength-scale embedded active-region photonic-crystal laser," *Opt. Express*, vol. 20, pp. 3773–3780, Feb 2012.

[5] J. Joannopoulos, S. Johnson, J. Winn, and R. Meade, *Photonic crystals: Molding the flow of light.* United States: Princeton University Press, Oct. 2011.

[6] E. Dimopoulos, A. Sakanas, A. Marchevsky, M. Xiong, Y. Yu, E. Semenova, J. Mørk, and K. Yvind, "Electrically-driven photonic crystal lasers with ultra-low threshold," *Laser & Photonics Reviews*, vol. 16, no. 11, p. 2200109, 2022.

[7] E. Dimopoulos, M. Xiong, A. Sakanas, A. Marchevsky, G. Dong, Y. Yu, E. Semenova, J. Mørk, and K. Yvind, "Experimental demonstration of a nanolaser with a sub- a threshold current," *Optica*, vol. 10, pp. 973–976, Aug 2023.

[8] H.-P. D. Yang, I.-C. Hsu, F.-I. Lai, H.-C. Kuo, and J. Y. Chi, "High-power single-mode vertical-cavity surface-emitting lasers with multi-leaf holey structure," *Japanese Journal of Applied Physics*, vol. 45, p. L871, aug 2006.

[9] N. Yokouchi, A. J. Danner, and K. D. Choquette, "Vertical-cavity surface-emitting laser operating with photonic crystal seven-point defect structure," *Applied Physics Letters*, vol. 82, pp. 3608–3610, 05 2003.

[10] A. Liu, M. Xing, H. Qu, W. Chen, W. Zhou, and W. Zheng, "Reduced divergence angle of photonic crystal vertical-cavity surface-emitting laser," *Applied Physics Letters*, vol. 94, p. 191105, 05 2009.

[11] M. Butt, S. Khonina, and N. Kazanskiy, "Recent advances in photonic crystal optical devices: A review," *Optics Laser Technology*, vol. 142, p. 107265, 2021.

[12] R. Athale and D. Psaltis, "Optical computing: Past and future," *Opt. Photon. News*, vol. 27, pp. 32–39, Jun 2016.

[13] T. Erneux and P. Glorieux, *Laser Dynamics.* Cambridge University Press, 2010.

[14] B. J. Shastri, A. N. Tait, T. F. de Lima, *et al.*, "Photonics for artificial intelligence and neuromorphic computing," *Nat. Photonics*, vol. 15, pp. 102–114, 2021.

[15] T. Alexoudi, G. T. Kanellos, and N. Pleros, "Optical ram and integrated optical memories: a survey," *Light: Science & Applications*, vol. 9, p. 91, May 2020.

[16] J. Buck and W. Hayt, *Engineering Electromagnetics.* McGraw-Hill Education, 2011.

[17] D. Molka, D. Hackenberg, and R. Schöne, "Main memory and cache performance of intel sandy bridge and amd bulldozer," in *Proceedings of the Workshop on Memory Systems Performance and Correctness*, MSPC '14, (New York, NY, USA), Association for Computing Machinery, 2014.

[18] S. Yu and P.-Y. Chen, "Emerging memory technologies: Recent trends and prospects," *IEEE Solid-State Circuits Magazine*, vol. 8, no. 2, pp. 43–56, 2016.

[19] M. T. Hill, H. J. S. Dorren, T. de Vries, X. J. M. Leijtens, J. H. den Besten, B. Smalbrugge, Y.-S. Oei, H. Binsma, G.-D. Khoe, and M. K. Smit, "A fast low-power optical memory based on coupled micro-ring lasers," *Nature*, vol. 432, pp. 206–209, Nov 2004.

[20] N. Pleros, D. Apostolopoulos, D. Petrantonakis, C. Stamatiadis, and H. Avramopoulos, "Optical static ram cell," *IEEE Photonics Technology Letters*, vol. 21, no. 2, pp. 73–75, 2009.

[21] C.-H. Chen, S. Matsuo, K. Nozaki, A. Shinya, T. Sato, Y. Kawaguchi, H. Sumikura, and M. Notomi, "All-optical memory based on injection-locking bistability in photonic crystal lasers," *Opt. Express*, vol. 19, pp. 3387–3395, Feb 2011.

[22] J. Chang, Y.-H. Chen, W.-M. Chan, S. P. Singh, H. Cheng, H. Fujiwara, J.-Y. Lin, K.-C. Lin, J. Hung, R. Lee, H.-J. Liao, J.-J. Liaw, Q. Li, C.-Y. Lin, M.-C. Chiang, and S.-Y. Wu, "7nm 256mb sram in high-k metal-gate finfet technology with write-assist circuitry for low-vmin applications," in *2017 IEEE International Solid-State Circuits Conference (ISSCC)*, pp. 206–207, 2017.

[23] S. Pitris, C. Vagionas, T. Tekin, R. Broeke, G. T. Kanellos, and N. Pleros, "Wdm-enabled optical ram at 5 gb/s using a monolithic inp flip-flop chip," *IEEE Photonics Journal*, vol. 8, no. 2, pp. 1–7, 2016.

[24] K. Nozaki, A. Shinya, S. Matsuo, Y. Suzaki, T. Segawa, T. Sato, Y. Kawaguchi, R. Takahashi, and M. Notomi, "Ultralow-power all-optical ram based on nanocavities," *Nature Photonics*, vol. 6, pp. 248–252, Apr 2012.

[25] J. Zhou, M. Cada, and T. Makino, "All-optical bistable switching dynamics in 1.55-/spl mu/m two-segment strained multiquantum-well distributed-feedback lasers," *Journal of Lightwave Technology*, vol. 15, no. 2, pp. 342–355, 1997.

[26] M. Bohr, "Nanotechnology goals and challenges for electronic applications," *IEEE Transactions on Nanotechnology*, vol. 1, no. 1, pp. 56–62, 2002.

[27] D. A. B. Miller, "Attojoule optoelectronics for low-energy information processing and communications," *Journal of Lightwave Technology*, vol. 35, no. 3, pp. 346–396, 2017.

[28] A. N. Tait, T. Ferreira de Lima, M. A. Nahmias, H. B. Miller, H.-T. Peng, B. J. Shastri, and P. R. Prucnal, "Silicon photonic modulator neuron," *Phys. Rev. Appl.*, vol. 11, p. 064043, Jun 2019.

[29] B. J. Shastri, M. A. Nahmias, A. N. Tait, A. W. Rodriguez, B. Wu, and P. R. Prucnal, "Spike processing with a graphene excitable laser," *Scientific Reports*, vol. 6, p. 19126, Jan 2016.

[30] J. Mork, Y. Chen, and M. Heuck, "Photonic crystal fano laser: Terahertz modulation and ultrashort pulse generation," *Phys. Rev. Lett.*, vol. 113, p. 163901, Oct 2014.

[31] A. R. Zali, M. K. Moravvej-Farshi, Y. Yu, and J. Mørk, "Small and large signal analysis of photonic crystal fano laser," *Journal of Lightwave Technology*, vol. 36, no. 23, pp. 5611–5616, 2018.

[32] T. S. Rasmussen, Y. Yu, and J. Mørk, "Modes, stability, and small-signal response of photonic crystal fano lasers," *Opt. Express*, vol. 26, pp. 16365–16376, Jun 2018.

[33] T. S. Rasmussen, Y. Yu, and J. Mørk, "Theory of self-pulsing in photonic crystal fano lasers," *Laser & Photonics Reviews*, vol. 11, no. 5, p. 1700089, 2017.

[34] T. S. Rasmussen, Y. Yu, and J. Mørk, "Suppression of coherence collapse in semiconductor fano lasers," *Phys. Rev. Lett.*, vol. 123, p. 233904, Dec 2019.

[35] T. S. Rasmussen and J. Mørk, "Theory of microscopic semiconductor lasers with external optical feedback," *Opt. Express*, vol. 29, pp. 14182–14188, May 2021.

[36] Y. Yu, W. Xue, E. Semenova, K. Yvind, and J. Mørk, "Demonstration of a self-pulsing photonic crystal fano laser," *Nature Photonics*, vol. 11, pp. 81–84, Feb 2017.

[37] Y. Yu, A. Sakanas, A. R. Zali, E. Semenova, K. Yvind, and J. Mørk, "Ultra-coherent fano laser based on a bound state in the continuum," *Nature Photonics*, vol. 15, no. 10, pp. 758–764, 2021.

[38] G. Dong, S. L. Liang, A. Sakanas, E. Semenova, K. Yvind, J. Mørk, and Y. Yu, "Cavity dumping using a microscopic fano laser," *Optica*, vol. 10, pp. 248–254, Feb 2023.

[39] G. L. Lippi, "Amplified spontaneous emission" in micro- and nanolasers," *Atoms*, vol. 9, no. 1, 2021.

[40] U. Fano, "Effects of configuration interaction on intensities and phase shifts," *Phys. Rev.*, vol. 124, pp. 1866–1878, Dec 1961.

[41] K. Yamada, *Silicon Photonic Wire Waveguides: Fundamentals and Applications*, pp. 1–29. Berlin, Heidelberg: Springer Berlin Heidelberg, 2011.

[42] D. Bekele, Y. Yu, K. Yvind, and J. Mørk, "In-plane photonic crystal devices using fano resonances," *Laser & Photonics Reviews*, vol. 13, no. 12, p. 1900054, 2019.

[43] M. F. Limonov, M. V. Rybin, A. N. Poddubny, and Y. S. Kivshar, "Fano resonances in photonics," *Nature Photonics*, vol. 11, pp. 543–554, Sep 2017.

[44] J. Mørk, Y. Yu, T. S. Rasmussen, E. Semenova, and K. Yvind, "Semiconductor fano lasers," *IEEE Journal of Selected Topics in Quantum Electronics*, vol. 25, no. 6, pp. 1–14, 2019.

[45] C. J. R. Sheppard, "Approximate calculation of the reflection coefficient from a stratified medium," *Pure and Applied Optics: Journal of the European Optical Society Part A*, vol. 4, p. 665, sep 1995.

[46] H. Ishii, H. Tanobe, F. Kano, Y. Tohmori, Y. Kondo, and Y. Yoshikuni, "Quasi-continuous wavelength tuning in super-structure-grating (ssg) dbr lasers," *IEEE Journal of Quantum Electronics*, vol. 32, no. 3, pp. 433–441, 1996.

[47] S. Zamek, L. Feng, M. Khajavikhan, D. T. H. Tan, M. Ayache, and Y. Fainman, "Micro-resonator with metallic mirrors coupled to a bus waveguide," *Opt. Express*, vol. 19, pp. 2417–2425, Jan 2011.

[48] Y. Yu, E. Palushani, M. Heuck, N. Kuznetsova, P. T. Kristensen, S. Ek, D. Vukovic, C. Peucheret, L. K. Oxenløwe, S. Combrié, A. de Rossi, K. Yvind, and J. Mørk, "Switching characteristics of an inp photonic crystal nanocavity: Experiment and theory," *Opt. Express*, vol. 21, pp. 31047–31061, Dec 2013.

[49]   B. A. Daniel, D. N. Maywar, and G. P. Agrawal, "Dynamic mode theory of optical resonators undergoing refractive index changes," *J. Opt. Soc. Am. B*, vol. 28, pp. 2207–2215, Sep 2011.

[50]   N.-P. Diamantopoulos, T. Fujii, S. Yamaoka, H. Nishi, K. Takeda, T. Tsuchizawa, T. Segawa, T. Kakitsuka, and S. Matsuo, "60 ghz bandwidth directly modulated membrane iii-v lasers on sio2/si," *Journal of Lightwave Technology*, vol. 40, no. 10, pp. 3299–3306, 2022.

[51]   J. R. Tredicce, F. T. Arecchi, G. L. Lippi, and G. P. Puccioni, "Instabilities in lasers with an injected signal," *J. Opt. Soc. Am. B*, vol. 2, pp. 173–183, Jan 1985.

[52]   L. A. Coldren, S. W. Corzine, and M. L. Mašanović, *Diode Lasers and Photonic Integrated Circuits.* John Wiley Sons, Inc., 2012.

[53]   P. Landsberg and A. Beattie, "Auger effect in semiconductors," *Journal of Physics and Chemistry of Solids*, vol. 8, pp. 73–75, 1959.

[54]   S. Fan, W. Suh, and J. D. Joannopoulos, "Temporal coupled-mode theory for the fano resonance in optical resonators," *J. Opt. Soc. Am. A*, vol. 20, pp. 569–572, Mar 2003.

[55]   H. Haus, *Waves and Fields in Optoelectronics.* Prentice-Hall series in solid state physical electronics, Prentice-Hall, 1984.

[56]   B. Tromborg, H. Olesen, X. Pan, and S. Saito, "Transmission line description of optical feedback and injection locking for fabry-perot and dfb lasers," *IEEE Journal of Quantum Electronics*, vol. 23, no. 11, pp. 1875–1889, 1987.

[57]   J. C. Butcher, *Numerical Differential Equation Methods*, ch. 2, pp. 55–142. John Wiley Sons, Ltd, 2016.

[58]   H. Langtangen and S. Linge, *Finite Difference Computing with PDEs: A Modern Software Approach.* Texts in Computational Science and Engineering, Springer International Publishing, 2017.

[59]   M. Levinshtein, S. Rumyantsev, M. Shur, and W. Scientific, *Handbook Series on Semiconductor Parameters: Ternary and quaternary III-V compounds.* EBL-Schweitzer, World Scientific Publishing Company, 1999.

[60]   T. Rasmussen, *Light-matter interaction and laser dynamics in nanophotonic structures.* PhD thesis, 2020.

[61]   G. Keeler, B. Nelson, D. Agarwal, C. Debaes, N. Helman, A. Bhatnagar, and D. Miller, "The benefits of ultrashort optical pulses in optically interconnected systems," *IEEE Journal of Selected Topics in Quantum Electronics*, vol. 9, no. 2, pp. 477–485, 2003.

[62] D. A. B. Miller, "Device requirements for optical interconnects to silicon chips," *Proceedings of the IEEE*, vol. 97, no. 7, pp. 1166–1185, 2009.

[63] B. Nelson, G. Keeler, D. Agarwal, N. Helman, and D. Miller, "Wavelength division multiplexed optical interconnect using short pulses," *IEEE Journal of Selected Topics in Quantum Electronics*, vol. 9, no. 2, pp. 486–491, 2003.

[64] A. V. Pushkin, E. A. Migal, S. Tokita, Y. V. Korostelin, and F. V. Potemkin, "Femtosecond graphene mode-locked fe:znse laser at 4.4 µm," *Opt. Lett.*, vol. 45, pp. 738–741, Feb 2020.

[65] J. D. Kafka, T. Baer, and D. W. Hall, "Mode-locked erbium-doped fiber laser with soliton pulse shaping," *Opt. Lett.*, vol. 14, pp. 1269–1271, Nov 1989.

[66] A. Hermans, K. Van Gasse, J. . Kjellman, C. Caër, T. Nakamura, Y. Inada, K. Hisada, T. Hirasawa, S. Cuyvers, S. Kumari, A. Marinins, R. Jansen, G. Roelkens, P. Soussan, X. Rottenberg, and B. Kuyken, "High-pulse-energy III-V-on-silicon-nitride mode-locked laser," *APL Photonics*, vol. 6, p. 096102, 09 2021.

[67] C. Gordón, R. Guzmán, X. Leijtens, and G. Carpintero, "On-chip mode-locked laser diode structure using multimode interference reflectors," *Photon. Res.*, vol. 3, pp. 15–18, Feb 2015.

[68] J. J. Zayhowski, "Q-switched operation of microchip lasers," *Opt. Lett.*, vol. 16, pp. 575–577, Apr 1991.

[69] R. S. Conroy, T. Lake, G. J. Friel, A. J. Kemp, and B. D. Sinclair, "Self-q-switched nd:yvo4 microchip lasers," *Opt. Lett.*, vol. 23, pp. 457–459, Mar 1998.

[70] G. N. Gibson, R. Klank, F. Gibson, and B. E. Bouma, "Electro-optically cavity-dumped ultrashort-pulse ti:sapphire oscillator," *Opt. Lett.*, vol. 21, pp. 1055–1057, Jul 1996.

[71] J. Myers, C. Kokoczka, G. Cook, and R. Bedford, "High peak power cavity dumping semiconductor lasers," *Opt. Lett.*, vol. 42, pp. 113–116, Jan 2017.

[72] H. Long, Y.-Z. Huang, Y.-D. Yang, L.-X. Zou, J.-L. Xiao, X.-W. Ma, X.-M. Lv, B.-W. Liu, and Y. Du, "High-speed direct-modulated unidirectional emission square microlasers," *Journal of Lightwave Technology*, vol. 33, no. 4, pp. 787–794, 2015.

[73] L.-X. Zou, Y.-Z. Huang, X.-M. Lv, H. Long, J.-L. Xiao, Y.-D. Yang, and Y. Du, "Dynamic characteristics of algainas/inp octagonal resonator microlaser," *Applied Physics B*, vol. 117, pp. 453–458, Oct 2014.

[74] G. C. Park, W. Xue, M. Piels, D. Zibar, J. Mørk, E. Semenova, and I.-S. Chung, "Ultrahigh-speed si-integrated on-chip laser with tailored dynamic characteristics," *Scientific Reports*, vol. 6, p. 38801, Dec 2016.

[75]   N. Tessler, M. Margalit, G. Eisenstein, and U. Koren, "Wide-band amplitude modulation by electrooptic tuning of the center wavelength in short-cavity distributed bragg reflector lasers," *IEEE Journal of Selected Topics in Quantum Electronics*, vol. 1, no. 2, pp. 490–493, 1995.

[76]   P. Dong, A. Melikyan, K. Kim, N. Kaneda, B. Stern, and Y. Baeyens, "In-phase/quadrature modulation using directly reflectivity-modulated laser," *Optica*, vol. 7, pp. 929–933, Aug 2020.

[77]   P. Dong, A. Maho, R. Brenot, Y.-K. Chen, and A. Melikyan, "Directly reflectivity modulated laser," *Journal of Lightwave Technology*, vol. 36, no. 5, pp. 1255–1261, 2018.

[78]   F. Früngel, *Optical Pulses - Lasers - Measuring Techniques*. Elsevier Science, 2014.

[79]   U. Keller, *Q-Switching*, pp. 373–418. Cham: Springer International Publishing, 2021.

[80]   R. Paschotta, *Active and Passive Q Switching*. SPIE, September 2009.

[81]   C. B. Hitz, J. J. Ewing, and J. Hecht, *Cavity Dumping and Modelocking*, pp. 143–153. 2012.

[82]   B. Bennett, R. Soref, and J. Del Alamo, "Carrier-induced change in refractive index of inp, gaas and ingaasp," *IEEE Journal of Quantum Electronics*, vol. 26, no. 1, pp. 113–122, 1990.

[83]   E. Burstein, "Anomalous optical absorption limit in insb," *Phys. Rev.*, vol. 93, pp. 632–633, Feb 1954.

[84]   T. Moss, G. Burrell, and B. Ellis, "Chapter 3 - absorption processes in semiconductors," in *Semiconductor Opto-Electronics*, pp. 48–94, Butterworth-Heinemann, 1973.

[85]   L. P. Zverev, S. A. Negashev, V. V. Kruzhaev, and G. M. Minkov, "Mechanism of band gap variation in heavily doped gallium arsenide," *Soviet Physics - Semiconductors*, vol. 11, pp. 603–605, 1977.

[86]   C. H. Henry, R. A. Logan, and K. A. Bertness, "Spectral dependence of the change in refractive index due to carrier injection in GaAs lasers," *Journal of Applied Physics*, vol. 52, pp. 4457–4461, 07 1981.

[87]   F. Stern, "Dispersion of the index of refraction near the absorption edge of semiconductors," *Phys. Rev.*, vol. 133, pp. A1653–A1664, Mar 1964.

[88]   C. Grein and S. John, "Temperature dependence of the fundamental optical absorption edge in crystals and disordered semiconductors," *Solid State Communications*, vol. 70, no. 1, pp. 87–91, 1989.

[89]   G. Cocorullo, F. G. Della Corte, and I. Rendina, "Temperature dependence of the thermo-optic coefficient in crystalline silicon between room temperature and 550 K at the wavelength of 1523 nm," *Applied Physics Letters*, vol. 74, pp. 3338–3340, 05 1999.

[90]   S. Krishnamurthy, Z. G. Yu, L. P. Gonzalez, and S. Guha, "Temperature- and wavelength-dependent two-photon and free-carrier absorption in GaAs, InP, GaInAs, and InAsP," *Journal of Applied Physics*, vol. 109, p. 033102, 02 2011.

[91]   D. Vignaud, J. F. Lampin, and F. Mollot, "Two-photon absorption in InP substrates in the 1.55 m range," *Applied Physics Letters*, vol. 85, pp. 239–241, 07 2004.

[92]   T. J. Johnson, M. Borselli, and O. Painter, "Self-induced optical modulation of the transmission through a high-q silicon microdisk resonator," *Opt. Express*, vol. 14, pp. 817–831, Jan 2006.

[93]   R. Righini, "Ultrafast optical kerr effect in liquids and solids," *Science*, vol. 262, no. 5138, pp. 1386–1390, 1993.

[94]   K. Saito and R. Ito, "Buried-heterostructure algaas lasers," *IEEE Journal of Quantum Electronics*, vol. 16, no. 2, pp. 205–215, 1980.

[95]   S. Matsuo, A. Shinya, T. Kakitsuka, K. Nozaki, T. Segawa, T. Sato, Y. Kawaguchi, and M. Notomi, "High-speed ultracompact buried heterostructure photonic-crystal laser with 13 fj of energy consumed per bit transmitted," *Nature Photonics*, vol. 4, pp. 648–654, Sep 2010.

[96]   W. Xue, L. Ottaviano, Y. Chen, E. Semenova, Y. Yu, A. Lupi, J. Mørk, and K. Yvind, "Thermal analysis of line-defect photonic crystal lasers," *Opt. Express*, vol. 23, pp. 18277–18287, Jul 2015.

[97]   M. M. Mano and C. Kime, *Logic and Computer Design Fundamentals*. USA: Prentice Hall Press, 4th ed., 2007.

[98]   W. D'Oosterlinck, F. Öhman, J. Buron, S. Sales, A. P. Pardo, A. Ortigosa-Blanch, G. Puerto, G. Morthier, and R. Baets, "All-optical flip-flop operation using a soa and dfb laser diode optical feedback combination," *Opt. Express*, vol. 15, pp. 6190–6199, May 2007.

[99]   H. Dorren, D. Lenstra, Y. Liu, M. Hill, and G.-D. Khoe, "Nonlinear polarization rotation in semiconductor optical amplifiers: theory and application to all-optical flip-flop memories," *IEEE Journal of Quantum Electronics*, vol. 39, no. 1, pp. 141–148, 2003.

[100] Y. Naito, S. Shimizu, T. Kato, K. Kobayashi, and H. Uenohara, "Investigation of all-optical latching operation of a monolithically integrated soa-mzi with a feedback loop," *Opt. Express*, vol. 20, pp. B339–B349, Dec 2012.

[101] A. Trita, G. Mezosi, M. J. L. Vidal, M. Zanola, I. Cristiani, M. Sorel, P. Ghelfi, A. Bogoni, and G. Giuliani, "10 gb/s operation of monolithic all-optical set-reset flip-flop based on semiconductor ring laser," in *CLEO/QELS: 2010 Laser Science to Photonic Applications*, pp. 1–2, 2010.

[102] Y. Gong and J. Vučković, "Photonic crystal cavities in silicon dioxide," *Applied Physics Letters*, vol. 96, p. 031107, 01 2010.

[103] K.-Y. Jeong, Y.-S. No, Y. Hwang, K. S. Kim, M.-K. Seo, H.-G. Park, and Y.-H. Lee, "Electrically driven nanobeam laser," *Nature Communications*, vol. 4, p. 2822, Nov 2013.

[104] G. Dong, M. Xiong, E. Dimopoulos, A. Sakanas, E. Semenova, K. Yvind, Y. Yu, and J. Mørk, "Fano laser based on a photonic crystal nanobeam cavity," in *Conference on Lasers and Electro-Optics*, p. STu4E.6, Optica Publishing Group, 2022.

[105] N. Ismail, C. C. Kores, D. Geskus, and M. Pollnau, "Fabry-pérot resonator: spectral line shapes, generic and related airy distributions, linewidths, finesses, and performance at low or frequency-dependent reflectivity," *Opt. Express*, vol. 24, pp. 16366–16389, Jul 2016.

[106] B. Holdsworth and C. Woods, *Digital Logic Design.* Elsevier Science, 2002.

[107] M. Saldutti, Y. Yu, P. T. Kristensen, G. Kountouris, and J. Mørk, "Carrier dynamics in nonlinear photonic nanocavities with extreme dielectric confinement," in *2022 IEEE Photonics Conference (IPC)*, pp. 1–2, 2022.

[108] M. Saldutti, Y. Yu, G. Kountouris, P. T. Kristensen, and J. Mørk, "Carrier diffusion in semiconductor nanoscale resonators," 2023.

[109] T. S. Rasmussen, Y. Yu, and J. Mørk, "All-optical non-linear activation function for neuromorphic photonic computing using semiconductor fano lasers," *Opt. Lett.*, vol. 45, pp. 3844–3847, Jul 2020.

[110] M. Saldutti, M. Xiong, E. Dimopoulos, Y. Yu, M. Gioannini, and J. Mørk, "Modal properties of photonic crystal cavities and applications to lasers," *Nanomaterials*, vol. 11, no. 11, 2021.

[111] P. Hamel, S. Haddadi, F. Raineri, P. Monnier, G. Beaudoin, I. Sagnes, A. Levenson, and A. M. Yacomotti, "Spontaneous mirror-symmetry breaking in coupled photonic-crystal nanolasers," *Nature Photonics*, vol. 9, pp. 311–315, May 2015.

[112] J. T. Stuart, "On the non-linear mechanics of wave disturbances in stable and unstable parallel flows part 1. the basic behaviour in plane poiseuille flow," *Journal of Fluid Mechanics*, vol. 9, no. 3, p. 353–370, 1960.

[113] S. Strogatz, *Nonlinear Dynamics and Chaos: With Applications to Physics, Biology, Chemistry, and Engineering.* CRC Press, 2018.

[114] P. D. García, G. Kiršanskė, A. Javadi, S. Stobbe, and P. Lodahl, "Two mechanisms of disorder-induced localization in photonic-crystal waveguides," *Phys. Rev. B*, vol. 96, p. 144201, Oct 2017.

[115] V. I. Kopp, B. Fan, H. K. M. Vithana, and A. Z. Genack, "Low-threshold lasing at the edge of a photonic stop band in cholesteric liquid crystals," *Opt. Lett.*, vol. 23, pp. 1707–1709, Nov 1998.

[116] M. Notomi, E. Kuramochi, and H. Taniyama, "Ultrahigh-q nanocavity with 1d photonic gap," *Opt. Express*, vol. 16, pp. 11095–11102, Jul 2008.

[117] S. Lichtmannecker, M. Florian, T. Reichert, M. Blauth, M. Bichler, F. Jahnke, J. J. Finley, C. Gies, and M. Kaniber, "A few-emitter solid-state multi-exciton laser," *Scientific Reports*, vol. 7, p. 7420, Aug 2017.

[118] C.-Y. A. Ni and S. L. Chuang, "Theory of high-speed nanolasers and nanoleds," *Opt. Express*, vol. 20, pp. 16450–16470, Jul 2012.

[119] E. M. Purcell, "Spontaneous emission probabilities at radio frequencies," *Phys. Rev.*, vol. 69, p. 681, 1946.

[120] M. Khajavikhan, A. Simic, M. Katz, J. H. Lee, B. Slutsky, A. Mizrahi, V. Lomakin, and Y. Fainman, "Thresholdless nanoscale coaxial lasers," *Nature*, vol. 482, pp. 204–207, Feb 2012.

[121] M. Bundgaard-Nielsen, E. V. Denning, M. Saldutti, and J. Mørk, "Stochastic approach to the quantum noise of a single-emitter nanolaser," *Phys. Rev. Lett.*, vol. 130, p. 253801, Jun 2023.

[122] K. L. Chung, *Poisson and Normal Distributions*, pp. 192–239. New York, NY: Springer New York, 1975.

[123] G. P. Puccioni and G. L. Lippi, "Stochastic simulator for modeling the transition to lasing," *Opt. Express*, vol. 23, pp. 2369–2374, Feb 2015.

[124] J. Mork and G. L. Lippi, "Rate equation description of quantum noise in nanolasers with few emitters," *Applied Physics Letters*, vol. 112, p. 141103, 04 2018.

[125] E. C. André, J. Mørk, and M. Wubs, "Efficient stochastic simulation of rate equations and photon statistics of nanolasers," *Opt. Express*, vol. 28, pp. 32632–32646, Oct 2020.

[126] R. C. Hilborn, "Einstein coefficients, cross sections, f values, dipole moments, and all that," *American Journal of Physics*, vol. 50, pp. 982–986, 11 1982.

[127] F. Stern and J. M. Woodall, "Photon recycling in semiconductor lasers," *Journal of Applied Physics*, vol. 45, pp. 3904–3906, 10 2003.

[128] A. Moelbjerg, P. Kaer, M. Lorke, B. Tromborg, and J. Mørk, "Dynamical properties of nanolasers based on few discrete emitters," *IEEE Journal of Quantum Electronics*, vol. 49, no. 11, pp. 945–954, 2013.

[129] D. T. Gillespie, "Exact stochastic simulation of coupled chemical reactions," *The Journal of Physical Chemistry*, vol. 81, pp. 2340–2361, Dec 1977.

[130] F. Arecchi, A. Berne, A. Sona, and P. Burlamacchi, "1a4 - photocount distributions and field statistics," *IEEE Journal of Quantum Electronics*, vol. 2, no. 9, pp. 341–350, 1966.

[131] T. Wang, G. P. Puccioni, and G. L. Lippi, "Dynamical buildup of lasing in mesoscale devices," *Scientific Reports*, vol. 5, p. 15858, Oct 2015.

[132] T. Wang, D. Aktas, O. Alibart, E. Picholle, G. P. Puccioni, S. Tanzilli, and G. L. Lippi, "Superthermal-light emission and nontrivial photon statistics in small lasers," *Phys. Rev. A*, vol. 101, p. 063835, Jun 2020.

[133] G. P. Puccioni and G. L. Lippi, "Stochastic simulator for modeling the transition to lasing," *Opt. Express*, vol. 23, pp. 2369–2374, Feb 2015.

[134] P. R. Rice and H. J. Carmichael, "Photon statistics of a cavity-qed laser: A comment on the laser–phase-transition analogy," *Phys. Rev. A*, vol. 50, pp. 4318–4329, Nov 1994.

[135] S. Cassina, G. Cenedese, M. Lamperti, M. Bondani, and A. Allevi, "On the use of superthermal light for imaging applications," 2023.

[136] Y. Yamamoto and N. Imoto, "Internal and external field fluctuations of a laser oscillator: Part i–quantum mechanical langevin treatment," *IEEE Journal of Quantum Electronics*, vol. 22, no. 10, pp. 2032–2042, 1986.

[137] G. N. Gol'tsman, O. Okunev, G. Chulkova, A. Lipatov, A. Semenov, K. Smirnov, B. Voronov, A. Dzardanov, C. Williams, and R. Sobolewski, "Picosecond superconducting single-photon optical detector," *Applied Physics Letters*, vol. 79, pp. 705–707, 08 2001.

[138] M. Scully and M. Zubairy, *Quantum Optics*. Quantum Optics, Cambridge University Press, 1997.

[139] R. Shanmugam and R. Chattamvelli, *Skewness and Kurtosis*, ch. 4, pp. 89–110. John Wiley Sons, Ltd, 2015.